UPPSALA
UNIVERSITET

Window Layer Structures for Chalcopyrite Thin-Film Solar Cells

FREDRIK LARSSON

Abstract

Larsson, F. 2020. Window Layer Structures for Chalcopyrite Thin-Film Solar Cells. *Digital Comprehensive Summaries of Uppsala Dissertations from the Faculty of Science and Technology* 1951. 110 pp. Uppsala: Acta Universitatis Upsaliensis. ISBN 978-91-513-0984-2.

This thesis aims to contribute to the development of improved window layer structures for chalcopyrite thin-film solar cells, with an emphasis on the buffer layer, to assist future reductions of the levelized cost of energy. This is realized by exploring the potential of existing materials and deposition processes, as well as developing new buffer layer processes based on atomic layer deposition (ALD).

Ternary compound ALD processes are more complicated to control than when depositing binary compounds and the composition can be significantly different at the absorber interface as compared to the bulk. A method based on in-situ quartz crystal microbalance that can measure these compositional variations is demonstrated in the thesis. Furthermore, the addition of alkali-metal fluoride post-deposition treatments (PDTs) can further complicate ALD of buffer layers, due to residual salts that are formed on the absorber surface during a PDT process. When applying ALD $ZnO_{1-x}S_x$ to KF-treated CIGS absorbers, competitive solar cell efficiencies could only be obtained after performing additional wet-chemical treatments prior to ALD processing.

It is shown that the performance of wide-bandgap solar cells can be greatly enhanced by improving the conduction band alignment between the absorber and buffer layers. By applying ALD $Zn_{1-x}Sn_xO_y$ buffer layers in $CuGaSe_2$ solar cells, record efficiency (η = 11.9%) and open-circuit voltage (V_{oc} = 1017 mV) values are demonstrated.

In search of a new buffer layer suitable for a wide range of absorber materials (and surface bandgaps), amorphous tin-gallium oxide grown by ALD is evaluated as a new buffer layer material. This material exhibits a highly variable bandgap (and electron affinity) the absorber/buffer conduction band alignment can be controlled by adjusting the cation composition and deposition temperature. The potential of $Sn_{1-x}Ga_xO_y$ as a buffer layer was studied in combination with low-bandgap $(Ag,Cu)(In,Ga)Se_2$ absorbers ($E_{g,surface} \approx 1.1$ eV). A best cell efficiency of 17.0% was achieved, which was lower than the efficiency of 18.6% obtained for the corresponding CdS reference due to slightly lower V_{oc} and higher series resistance. However, the full potential of $Sn_{1-x}Ga_xO_y$ as a buffer layer remains to be revealed.

Keywords: CIGS, atomic layer deposition, ALD, thin-film technology, window layer structures, buffer layers, front contacts, metal oxides, ternary compounds

Fredrik Larsson, Department of Materials Science and Engineering, Solar Cell Technology, Box 534, Uppsala University, SE-751 21 Uppsala, Sweden.

Till Tilde och Vilgot

List of papers

This thesis is based on the following papers, which are referred to in the text by their Roman numerals.

I   **Evaluation of different intrinsic ZnO and transparent conducting oxide layer combinations in Cu(In,Ga)Se$_2$ solar cells**, F. Larsson, J. Keller, M. Edoff, T. Törndahl, *Thin Solid Films* 633 (2017) 235–238

II   **Record 1.0 V open-circuit voltage in wide band gap chalcopyrite solar cells**, F. Larsson, N. Shariati Nilsson, J. Keller, C. Frisk, V. Kosyak, V., Edoff, M., Törndahl, T., *Progress in Photovoltaics: Research and Applications* 25(9) (2017) 755–763

III   **Atomic layer deposition of Zn(O,S) buffer layers for Cu(In,Ga)Se$_2$ solar cells with KF post-deposition treatment**, F. Larsson, O. Donzel-Gargand, J. Keller, M. Edoff, T. Törndahl, *Solar Energy Materials and Solar Cells* 183 (2018) 8–15

IV   **Atomic layer deposition of amorphous tin-gallium oxide films**, F. Larsson, J. Keller, D. Primetzhofer, L. Riekehr, M. Edoff, T. Törndahl, *Journal of Vacuum Science and Technology A* 37(3) (2019) 030906

V   **Amorphous tin-gallium oxide buffer layers in (Ag,Cu)(In,Ga)Se$_2$ solar cells**, F. Larsson, J. Keller, J. Olsson, O. Donzel-Gargand, N. M. Martin, M. Edoff, T. Törndahl, *Solar Energy Materials and Solar Cells* 215 (2020) 110647

VI   **Atomic layer deposition of ternary compounds on Cu(In,Ga)Se$_2$: An in situ quartz crystal microbalance study**, F. Larsson, L. Stolt, A. Hultqvist, M. Edoff, J. Keller, T. Törndahl, *ACS Applied Energy Materials* 3 (2020) 7208–7215

Reprints were made with permission from the respective publishers.

Author's contributions to the papers

I   Part of planning and majority of experimental work. Device simulations with input from co-authors. Main author.

II   Part of planning and device fabrication. Majority of electrical characterization. Crystallographic analysis. Main author.

III   Majority of planning and experimental work. All sample fabrication, solar cell characterization and material characterization with X-ray photoelectron spectroscopy. Main author.

IV   Majority of planning and experimental work. All sample fabrication, film growth studies by quartz-crystal microbalance, material characterization with X-ray fluorescence, X-ray reflectivity and resistivity measurements. Analysis of data from elastic recoil detection analysis and Rutherford backscattering spectrometry with input from co-authors. Main author.

V   Majority of planning and experimental work. All sample fabrication. Major part of solar cell and electrical characterization. Part of characterization with soft and hard X-ray photoelectron spectroscopy. Main author.

VI   Majority of planning and method development. Part of sample preparation and analysis with scanning electron microscopy. All of the material characterization with X-ray photoelectron spectroscopy and film growth characterization with quartz crystal microbalance. Main author.

Related work not included in the thesis

1. **Reduced interface recombination in Cu₂ZnSnS₄ solar cells with atomic layer deposition Zn₁₋ₓSnₓOᵧ buffer layers**, C. Platzer-Björkman, C. Frisk, J.K. Larsen, T. Ericson, S. Li, J.J.S. Scragg, J. Keller, F. Larsson, T. Törndahl, *Applied Physics Letters* 107 (2015) 243904

2. **Zinc-tin-oxide buffer layer and low temperature post annealing resulting in a 9.0% efficient Cd-free Cu₂ZnSnS₄ solar cell**, T. Ericson, F. Larsson, T. Törndahl, C. Frisk, J. Larsen, V. Kosyak, C. Hägglund, S. Li, C. Platzer-Björkman, *Solar RRL* 1 (2017) 1700001

3. **A Systematic study of light-on-bias behavior in Cu(In,Ga)Se₂ solar cells with varying absorber compositions**, P. Szaniawski, J. Olsson, C. Frisk, V. Fjällström, D. Ledinek, F. Larsson, U. Zimmermann, M. Edoff, *IEEE Journal of Photovoltaics* 7(3) (2017) 882–891

4. **Atomic layer deposition of electron selective SnOₓ and ZnO films on mixed halide perovskite: compatibility and performance**, A. Hultqvist, K. Aitola, K. Sveinbjörnsson, Z. Saki, F. Larsson, T. Törndahl, E. Johansson, G. Boschloo, M. Edoff, *ACS Applied Materials and Interfaces* 9 (2017) 29707–29716

5. **Deep surface Cu depletion induced by K in high-efficiency Cu(In,Ga)Se₂ solar cell absorbers**, O. Donzel-Gargand, T. Thersleff, J. Keller, T. Törndahl, F. Larsson, E. Wallin, L. Stolt, M. Edoff, *Progress in Photovoltaics: Research and Applications* 26 (2018) 730–739

6. **Secondary phase formation and surface modification from a high dose KF-post deposition treatment of (Ag,Cu)(In,Ga)Se₂ solar cell absorbers**, O. Donzel-Gargand, F. Larsson, T. Törndahl, L. Stolt, M. Edoff, *Progress in Photovoltaics: Research and Applications* 27 (2019) 220–228

7. **Cadmium free Cu₂ZnSnS₄ solar cells with 9.7% efficiency**, J. K. Larsen, F. Larsson, T. Törndahl, N. Saini, L. Riekehr, Y. Ren, A. Biswal, D. Hauschild, L. Weinhardt, C. Heske, C. Platzer-Björkman, *Advanced Energy Materials* 9 (2019) 1900439

8. **Post deposition treatments of (Ag,Cu)(In,Ga)Se₂ thin films for solar cells**, M. Edoff, T. Törndahl, F. Larsson, O. Stolt, N. Shariati-Nilsson, L. Stolt, *IEEE 46th Photovoltaic Specialists* Conference (2019) 0618–0621

Contents

List of abbreviations and acronyms

ALD	Atomic layer deposition	J–V	Current-density–voltage
ACIGS	$(Ag,Cu)(In,Ga)Se_2$	J–V(T)	Temperature-dependent current-density–voltage
ARC	Anti-reflective coating	LCOE	Levelized cost of energy
a-SGO	Amorphous $Sn_{1-x}Ga_xO_y$	MOS-CAP	Metal–oxide–semiconductor capacitor
CBD	Chemical bath deposition	PDT	Post-deposition treatment
CBO	Conduction band offset	QCM	Quartz crystal microbalance
CGS	$CuGaSe_2$	RBS	Rutherford backscattering spectrometry
CIGS	$Cu(In,Ga)Se_2$	RF	Radio frequency
C–V	Capacitance–voltage	R–T	Reflectance–transmittance
CVD	Chemical vapor deposition	SEM	Scanning electron microscopy
DC	Direct current	SLG	Soda-lime glass
DEZn	Diethylzinc, $Zn(C_2H_5)_2$	STEM	Scanning transmission electron microscopy
DMA$_4$Sn	Tetrakis(dimethyl-amido)tin(IV), $Sn(N(CH_3)_2)_4$	sp.	sputtered
DMA$_3$Ga	Tris(dimethylamido)-gallium(III)-dimer, $Ga_2(N(CH_3)_2)_6$	SRH	Shockley–Read–Hall
EDS	Energy dispersive X-ray spectroscopy	TCO	Transparent conducting oxide
EELS	Electron energy loss spectroscopy	TEM	Transmission electron microscopy
EQE	External quantum efficiency	ToF-ERDA	Time-of-flight elastic recoil detection analysis
GDOES	Glow-discharge optical emission spectroscopy	XPS	X-ray photoelectron spectroscopy
GGI	[Ga]/([Ga]+[In])	XRD	X-ray diffraction
GPC	Growth per cycle [Å]	XRF	X-ray fluorescence spectrometry
HAXPES	Hard X-ray photoelectron spectroscopy	XRR	X-ray reflectivity
IQE	Internal quantum efficiency	ZTO	$Zn_{1-x}Sn_xO_y$

η	Solar cell efficiency [%]
V_{oc}	Open-circuit voltage [mV]
FF	Fill factor [%]
J_{sc}	Short-circuit current density [mA/cm^2]
J_0	Dark saturation current density [mA/cm^2]
A	Diode ideality factor
A, B	Number of individual sub cycles per ALD super-cycle (Chapter 5 & 7)
R_s	Series resistance [$\Omega \cdot$cm^2]
R_{sh}	Shunt resistance [$\Omega \cdot$cm^2]
E_A	Recombination activation energy [eV]
E_g	Bandgap energy [eV]
E_{CBM}	Conduction band minimum energy [eV]
E_{VBM}	Valence band maximum energy [eV]
E_F	Fermi level [eV]
ΔE_c	Conduction band offset energy [eV]
χ	Electron affinity [eV]
Φ_{CNL}	Charge neutrality level [eV]
S	Screening factor
T	Temperature [K]
T_{ALD}	ALD temperature [°C]
x	Cation/anion ratio
	Optical path length [cm] (Chapter 2)
	Average number of exchanged ligands (Chapter 5)
d	Film thickness [nm]
ρ	Resistivity [$\Omega \cdot$cm]
	Density [g/cm^3] (Chapter 5)
M	Molar mass [g/mol]
n_i	Number of moles of cation i per area [mol/cm^2]
q	Elementary charge constant (1.602 176 634 × 10^{-19} C)
k	The Boltzmann constant (8.617 333 262... × 10^{-5} eV/K)
Δm	Mass gain per super-cycle [ng/cm^2]
$<\Delta m>$	Average mass gain per super-cycle [ng/cm^2]
N_D	Doping concentration [cm^{-3}]
α	Absorption coefficient [cm^{-1}]
h	Planck's constant (4.135 667 696... × 10^{-15} eV·s)
c	Speed of light in vacuum (299 792 458 m/s)
ν	Frequency of light [s^{-1}]
λ	Wavelength [nm]

1 Introduction

1.1 Background

The global living standard and life expectancy have never before been as high as it is today. A contributing reason to this is that a larger share of people has access to electricity [1]. Meanwhile, the global energy consumption is at unpreceded levels (160 000 TWh/year in 2018 [2]) and will continue to increase in the near future. This is very problematic, since a majority of the energy supply is provided by non-renewable and greenhouse gas emitting sources. Renewable energy sources (excluding traditional bio-fuels) provided 6700 TWh of energy in 2018, which only corresponded to 4% of the global energy consumption (see Figure 1.1). A substantially larger renewable energy production is needed for the transition to a more sustainable society.

Essentially all renewable energy sources are driven by solar irradiation, either directly or indirectly. The total solar irradiance is about 1360 W/m^2 at the top of earth's atmosphere [3]. Around half of this irradiance is either
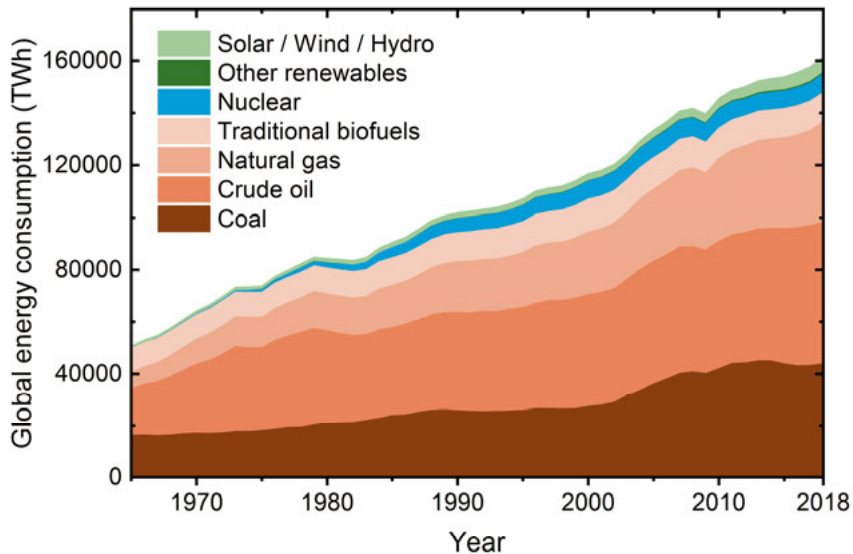

Figure 1.1. Global energy consumption by source for years between 1965 and 2018. Constructed from data reported in ref. [2].

reflected or absorbed in the atmosphere, while the remaining part reaches Earth's surface. It is difficult to grasp the magnitude of this number, so a comparison can be helpful: Each hour, 170 000 TWh of solar energy enters the top of the atmosphere, which is almost equal to the annular global energy consumption. Only a fraction of this energy is harvestable in practice, but the example is intended to demonstrate the enormous flux of energy that the sun provides. Using solar cells (also called photovoltaics) is the only way to convert solar radiation directly into electricity. It can also be an efficient way to provide electricity in remote locations.

The first semiconductor-based solar cells were invented by Charles Fritts in year 1883 and were made of selenium coated with a thin layer of gold [4]. Soon after, Fritts installed the world's first solar panels on a rooftop in New York [5]. However, the conversion efficiency of these solar cells was below 1%, which was too low for any practical power conversion application. It was not until the 1950s that the first useful solar cells were developed at Bell Laboratories by Chapin et al. [6]. The initial efficiency of these new solar cells was 6% and they were based on a so-called silicon p–n junction. This type of solar cell still dominates the market today, with a market share of 95% [7], and commercial solar panels with efficiencies above 20% are available [8].

During the recent decades, the cost of solar panels has been reduced by 20% for each doubling of the accumulative installed capacity [9]. The development has reached a point where solar cell technology can compete with non-renewable energy sources. As an example, according to a recent report from Fraunhofer ISE (2018), solar power has the lowest levelized cost of energy (LCOE) in Germany [10]. LCOE is a useful figure when comparing different energy sources and is calculated as the sum of all costs of a system divided by the total amount of generated energy, over the span of the system's lifetime. The cost of solar power is expected to continue decreasing. However, this is highly dependent on research and technological advancements.

Some ways to reduce the levelized cost further is to:

1. Increase the solar cell efficiency
2. Increase solar panel lifetime
3. Reduce material consumption
4. Increase throughput in production
5. Benefit from economy of scale

Thin-film solar cells have the potential to decrease both production and material costs, as compared to traditional crystalline silicon solar cells (e.g. by reducing the material and energy consumption). One of the commercial thin-film solar cell technologies is based on using the chalcopyrite compound $Cu(In,Ga)Se_2$ (CIGS) as light-absorbing material, which is the solar cell type of interest in this thesis. Here, the material demand is reduced by using only 1–2 μm thin absorber layers, which is about 50–100 times thinner than a strand

of hair. Another possibility that is unique for thin-film solar cells is the option to use flexible lightweight substrates, instead of glass. This can lower production and installation related costs, but also offer new opportunities to integrate solar cells in architecture and technology.

1.2 Aim of thesis

This thesis aims to contribute to the development of improved window layer structures for CIGS-based solar cells. The window layer structure consists of several transparent thin films with different functions and together they form the front contact of the solar cell. Among the different layers, special attention is given to the so-called buffer layer. The thesis contributes by increasing the overall knowledge of how the window layer properties and related process steps influence the solar cell performance. In addition, a part of the work is focused on developing window layer structures specifically suitable for wide-bandgap absorbers, which may be used in so-called multi-junction solar cells to push the efficiency limit higher.

The study was conducted under the boundary conditions that the processes used should not contain any toxic elements, should reduce chemical waste and be compatible with high throughput production. For this reason, only vacuum-based deposition techniques were used, and the thin-film deposition technique called atomic layer deposition (ALD) was employed instead of the conventionally used chemical bath deposition (CBD) process when depositing the buffer layer.

2 Physics of solar cells

The theory of solar cells is briefly reviewed in this chapter, aiming to provide an overview bridging the gap between fundamental semiconductor material properties and functioning solar cell devices. If a more comprehensive description is desired, the reader is encouraged to seek out one of the many textbooks available on the subject, e.g. *Solar Cells* by M.A. Green [11].

2.1 Semiconductors

A semiconductor is a material that can behave like either an insulator or a conductor depending on the temperature. The difference between insulators, semiconductors and conductors in terms of electrical conductivity is caused by differences in their energy band structures.

An energy band is a continuous range of allowed electronic states, which is formed by overlapping atomic orbitals from an infinite number of atoms. In Figure 2.1, the energy dispersion of typical band structures is visualized in simple band diagrams for conductors, semiconductors and insulators. The occupied band with highest energy is called the valence band and the unoccupied band with lowest energy is called the conduction band.

There is a gap in available electronic states between the valence and conduction band, where the energy difference between the bands is called the bandgap energy (E_g). Two types are typically distinguished—direct and indirect bandgaps. The band states are dispersed in the so-called momentum space. If the electron state at the conduction band minimum energy (E_{CBM}) has the same momentum vector as the state at the valence band maximum energy (E_{VBM}), the bandgap is direct. It is otherwise indirect.

Another important feature in the band diagrams is the energy position of the Fermi level (E_F). The Fermi level can be defined as the chemical potential for electrons at which the electron occupancy probability of an imaginary or real electronic state is 50%. For a conductor, the Fermi level is within a band. In both semiconductors and insulators, the Fermi level is in the bandgap. The difference between semiconductors and insulators is instead the magnitude of the bandgap, where the bandgap of a semiconductor is small enough to allow electrons to be thermally excited across the gap. Thermal excitation gives rise to a steady-state concentration of electrons in the conduction band, which is called the intrinsic carrier concentration n_i.
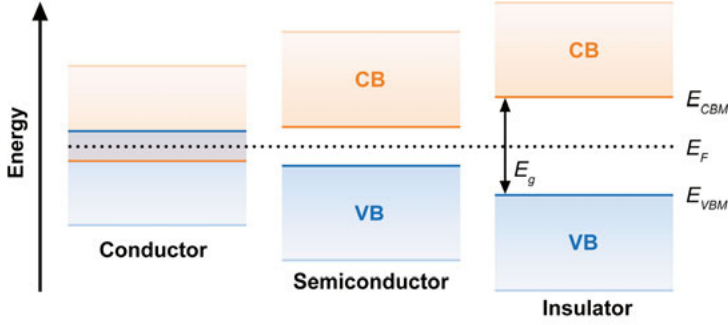
Figure 2.1. Schematic illustration of the difference in energy band dispersion between conductors, semiconductors and insulators.

If an electron is excited from the valence band to the conduction band, a vacant electron position is formed in the valence band. This vacant position is called a hole and is often regarded as an imaginary particle with a positive charge (h^+). For a semiconductor material without impurities, the concentration of holes in the valence band (denoted p) must be the same as the electron concentration in the conduction band (denoted n). However, it is possible to change the ratio between n and p by intentionally introducing impurities in the form of electron donors or acceptors. An electron donor introduces a state that is located at an energy level slightly below E_{CBM}, wherefrom electrons can easily be thermally excited to the conduction band, so that n increases. Similarly, an acceptor introduces a state slightly above E_{VBM}, which increases p. Regardless of doping concentrations, the product between n and p is constant at equilibrium according to the mass-action law: $np = n_i^2$. Note that the electrons and holes left in the dopant states are fixed in position and therefore do not contribute to the electrical conductivity (i.e. charge transport).

The conductivity in a semiconductor is given by

$$\sigma = \frac{1}{\rho} = q(\mu_e n + \mu_h p) \tag{2.1}$$

where ρ is the resistivity, q is the elementary charge, and μ_e and μ_h is the mobility of electrons and holes, respectively [12]. If electrons are the majority charge carrier in a semiconductor, it is called n-type. Likewise, if holes are the majority charge carrier in a semiconductor, it is called p-type. The charge carrier type of lower concentration is called the minority charge carrier.

2.2 Generation and recombination of charge carriers

The photovoltaic effect in semiconductors originates from the ability to absorb light to form electron–hole pairs.

As is well known from the Planck–Einstein relation, light can be described as a propagating electromagnetic wave with photon energy $E = h\nu$, where h is Planck's constant and ν is the wave frequency. When the photon energy is equal to or larger than the bandgap ($h\nu \geq E_g$), the photon can be absorbed by exciting a valence band electron to the conduction band. The probability of this process to happen is high for semiconductors with a direct bandgap. If the bandgap is indirect, the process must be phonon-assisted (assisted by vibrational energy), since photons alone cannot significantly change the electron's momentum. This results in a lower absorption coefficient for semiconductors with an indirect bandgap. A consequence of this is that materials with indirect bandgaps (such as crystalline silicon) require a longer optical path in the material to reach full absorption. Note that the light intensity follows an exponential attenuation in accordance with Beer–Lambert's law:

$$I(x) = I_0 e^{-x \cdot \alpha(\lambda)} \tag{2.2}$$

where I_0 is the intensity of the light that enters the absorber surface, $\alpha(\lambda)$ is the wavelength dependent absorption coefficient and x is the optical path length.

If the generated electron–hole pairs are not separated, they will spontaneously recombine. The mean time that electron–hole pairs survive before recombining defines the minority charge carrier lifetime. This is closely related to the diffusion length, which is the mean length minority charge carriers diffuse before they recombine.

There are three main types of recombination mechanisms: Radiative band–to–band recombination, Auger recombination and Shockley–Read–Hall (SRH) recombination. In radiative band–to–band recombination, the excess energy is emitted in form of a photon with an energy equal to the bandgap. Auger recombination is similar but involves a third electron. Here, the excess energy is transferred to another electron in the conduction band. In SRH recombination, the recombination is facilitated by defect states in the bandgap, where defect trap states in the middle of the band gap are the most effective recombination centers [12]. Moreover, the recombination rate is highest when the Fermi level is also positioned at the mid-gap energy. This is the dominating recombination mechanism in semiconductors with high defect concentrations, such as in CIGS [13].

2.3 The p–n junction and separation of charge carriers

A p–n junction is often used to separate electron–hole pairs after they have been generated. The junction is spontaneously formed when an n-type semiconductor shares an interface with a p-type semiconductor. When the two types of semiconductors are connected, the majority charge carriers of both sides diffuse to the opposing sides, leaving the close proximity of the junction depleted of charge carriers. This region is called the depletion region (or space-charge region). Positively charged ions (donors) remain on the n-side and negatively charged ions (acceptors) remain on the p-side, as illustrated in Figure 2.2a. This creates a built-in potential across the junction that impedes further charge carrier diffusion. The regions outside the depletion region, where the electric field is close to zero, are referred to as quasi-neutral regions.

Minority charge carriers that are photo-generated in the quasi-neutral region within a diffusion length away from the depletion region will be transported across the junction by the built-in electric field. This is illustrated in Figure 2.2b. This causes a photo-generated current that corresponds to the short-circuit current density (J_{sc}) when no load is connected. In open-circuit condition, an electric field opposite to the built-in field will form due to accumulation of charge. The potential difference across the two device terminals is the open-circuit voltage (V_{oc}).

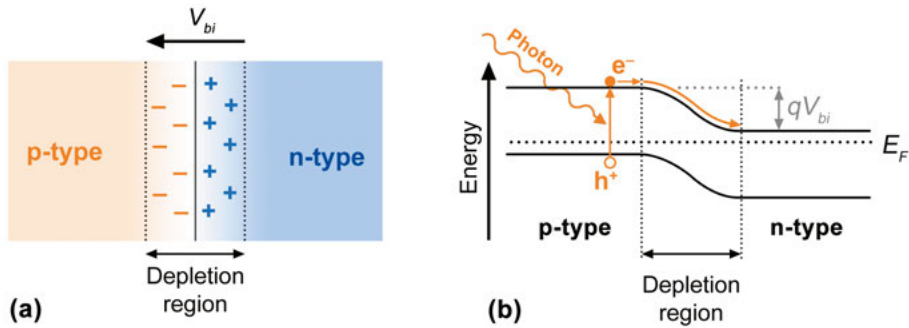**Figure 2.2**. (a) Illustration of a p–n junction with fixed ion charges (doping atoms) in the depletion region, and (b) the corresponding band diagram at short-circuit conditions. Photo-generation of an electron–hole pair and the subsequent charge separation is also shown. The excited electron first diffuses to the depletion region, after which it drifts across the junction by the electric field.

2.4 Current–voltage characteristics of solar cells

If a voltage bias is applied opposite to the built-in potential (called *forward bias*), the charge transport barrier is lowered. This allows more majority charge carriers to diffuse across the junction, resulting in a positive net-current in dark conditions. The current density (J) as a function of bias voltage (V) follows a typical diode behavior, where the current is exponentially increasing with forward bias but near constant in the reverse bias direction. This is described by Shockley's diode equation for ideal diodes [14]:

$$J = J_0 (e^{\frac{qV}{kT}} - 1)$$ (2.3)

where J_0 is the dark saturation current density, k is Boltzmann's constant, and T is the temperature.

For solar cells under illumination, the current-density–voltage (J–V) characteristic can be described by the empirical one-diode model as a first approximation:

$$J = J_0 \left(e^{\frac{q(V - J \cdot R_s)}{AkT}} - 1 \right) + \frac{(V - J \cdot R_s)}{R_{sh}} - J_L$$ (2.4)

This expression is a superposition of the ideal diode model in Eq. 2.3 and the photo-generated current density (J_L), with a few adjustments. The expression includes a voltage drop due to series resistance ($J \cdot R_s$) and an effective shunt path with the resistance R_{sh}. Furthermore, a diode ideality factor A is included that accounts for the deviation from the ideal diode model. It commonly has a value between 1 and 2, depending on the recombination characteristics of the solar cell [11].

Examples of solar cell J–V characteristics in dark and under illumination are shown in Figure 2.3. Several parameters can be extracted from the J–V curve measured under illumination (without the need to apply any model), where the most important are V_{oc}, J_{sc}, fill factor (*FF*) and efficiency (η). As indicated in the figure, the V_{oc} and J_{sc} values are simply read from the intercepts (i.e. at short-circuit and open-circuit conditions). *FF* is the ratio between the maximum power density output (P_{mp}) and the maximum power limit defined by $V_{oc} \cdot J_{sc}$:

$$FF = \frac{P_{mp}}{V_{oc} \cdot J_{sc}} = \frac{V_{mp} \cdot J_{mp}}{V_{oc} \cdot J_{sc}}$$ (2.5)

Here, V_{mp} and J_{mp} are the voltage and current density, respectively, at the maximum power point. Graphically, the *FF* can be regarded as the squareness
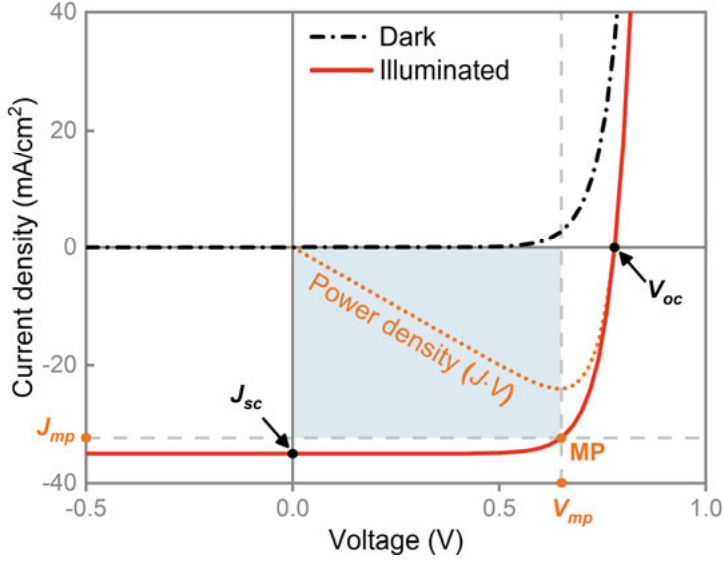
Figure 2.3. Example of J–V curves for a solar cell in dark and under illumination. The power density (arbitrary scale) is included to show the location of the maximum power point.

of the J–V curve. It is also a quality indicator of the device and is strongly affected by R_{sh}, R_s, J_0 and A (essentially all one-diode model parameters). However, it can also be influenced by non-ideal phenomena that are not included in the one-diode model in Eq. 2.4.

The most important parameter for a solar cell is undeniably the efficiency, which is defined as the maximum output power density divided by the incoming power density. This can be expressed as:

$$\eta = \frac{P_{mp}}{P_{in}} = \frac{V_{oc} \cdot J_{sc} \cdot FF}{P_{in}} \tag{2.6}$$

2.5 Fundamental efficiency limit

The absorber bandgap has a direct impact on the upper efficiency limit of a solar cell. As seen in Eq. 2.6, the efficiency is proportional to the product $V_{oc} \cdot J_{sc}$. The value for V_{oc} cannot be higher than the bandgap, and J_{sc} is limited by the number of photons that have a higher energy than the bandgap. Consequently, a wider bandgap allows for higher V_{oc} but lower J_{sc}. Therefore, an optimal bandgap value exists.

A derivation of the theoretical efficiency limit for single p–n junction solar cells was first presented by Shockley and Queisser [15]. They calculated the upper efficiency limit to be 30.5% at a bandgap of 1.35 eV, based on

blackbody radiation at 6000 K. Later, the Shockley–Queisser limit has been adjusted considering the AM1.5 spectrum [16], which is the solar spectrum after the light has travelled 1.5 times through the atmospheric thickness. The adjusted upper efficiency limit is 33.1% at a bandgap of 1.35 eV, though a second local maximum peak at 32.8% is found at 1.15 eV [17]. These values are based on the following assumptions:

1. The diode ideality factor is equal to 1 ($A = 1$)
2. All light is absorbed when the photon energy is larger than the bandgap ($hv > E_g$)
3. The only recombination mechanism is radiative band-to-band recombination
4. The radiative energy losses from the solar cell is based on a blackbody radiation at 300 K (which sets a lower limit for J_0)

Note that the radiative energy losses set a lower limit for J_0 and therefore limit the maximum achievable V_{oc} and FF [17].

   It is unlikely that the upper efficiency limit can be reached for practical devices. However, worth mentioning is the possibility to use multi-junction solar cells, that are constructed of multiple p–n junctions with several absorbers with different bandgaps, in order to increase the efficiency beyond the Shockley–Queisser limit [18]. By using absorbers with different bandgaps, a larger portion of the solar spectrum can be utilized without a loss in voltage.

3 Chalcopyrite thin-film solar cells

3.1 Chalcopyrite structured absorber layers

Chalcopyrite thin-film solar cells are in this thesis referring to solar cells fabricated with absorber layer compounds that have a chalcopyrite crystal structure, named after the mineral Chalcopyrite ($CuFeS_2$). The chalcopyrite structure is tetragonal with space group $I\bar{4}2d$, where each cation is surrounded by four anions and the two separate sites for cations with oxidation numbers +I and +III alternate throughout the structure [19].

More specifically, polycrystalline CIGS, $CuGaSe_2$ (CGS) and $(Ag,Cu)(In,Ga)Se_2$ (ACIGS), were used as absorbers in this thesis. The two latter can be regarded as sub-types or alterations of CIGS. Therefore, the following discussions will be mainly on CIGS absorbers in general.

3.2 Properties of Cu(In,Ga)Se$_2$

CIGS is a semiconducting material with high tolerance for off-stoichiometry and can be both n-type and p-type, depending on the concentrations of different intrinsic defects [20]. In CIGS solar cells, p-type absorbers are utilized where the doping is dominated by shallow acceptor levels formed by copper vacancies (V_{Cu}), compensated by In_{Cu} anti-site defects. This can be achieved by using copper-poor CIGS, typically grown in selenium rich conditions to suppress the formation of compensating selenium vacancies (V_{Se}). The defect chemistry of CIGS is complex and the formation of various point defects and defect pairs such as ($2V_{Cu}-In/Ga_{Cu}$) and ($V_{Se}-V_{Cu}$) plays a central role in the electrical and structural properties of the CIGS absorber layer [20–22]. Furthermore, the doping can be modified via the introduction of sodium and other alkali metals, which tends to increase the net doping concentration. Incorporation of sodium during CIGS growth has several potential effects on both structural properties and defect chemistry. However, it is unclear what is the dominant effect on the p-doping [23–26].

The bandgap in CIGS is direct and exhibits a large optical absorption coefficient (up to around 10^5 cm^{-1} depending on photon wavelength and CIGS composition [27]). This enables the use of merely 1–2 µm thick absorber layers to absorb a vast majority of all incoming photons with energies larger than the bandgap energy. The bandgap energy varies between 1.0 eV for

CuInSe$_2$ and 1.7 eV for CuGaSe$_2$, rather independently of the copper content [27–29]. The bandgap value as a function of gallium content roughly follows the empirical formula

$$E_g = 1.004(1 - GGI) + 1.663 \cdot GGI - 0.033 \cdot GGI(1 - GGI) \qquad (3.1)$$

where *GGI* is the [Ga]/([Ga]+[In]) ratio [27]. Changes in electron affinity (χ) account for a majority of the bandgap variation while E_{VBM} is rather unaffected, as seen in Figure 3.1 where the bandgap energies and (calculated) band alignments are displayed for different chalcopyrite-structured absorbers. It is also possible to increase the bandgap by substituting selenium with sulfur, which decreases the electron affinity (higher E_{CBM}) and lowers E_{VBM}. Pure CuInS$_2$ and CuGaS$_2$ have bandgap energies of around 1.5 eV and 2.4 eV, respectively [30]. Yet another way to control the bandgap and the electron affinity is by substituting copper for silver, which gives a bandgap energy of around 1.7 eV for pure AgGaSe$_2$ [31]. This is associated with both an increased electron affinity and lowered E_{VBM} for higher silver concentrations, depending on the gallium concentration [32]. Note that the opposite effects on electron affinity from silver and gallium content, respectively, provide an opportunity to tailor both the bandgap and the electron affinity. This can be interesting when adjusting the band alignment between the absorber and the window layer structure.
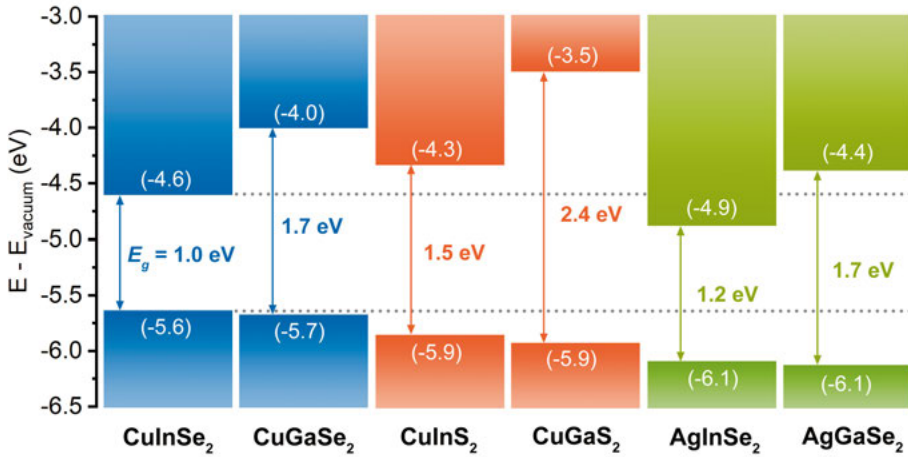
Figure 3.1. Bandgap energies and band alignments for different chalcopyrite-structured absorbers. Values within parenthesis indicate E_{VBM} and E_{CBM}, respectively. The figure is constructed from calculated values in refs. [32–35] by using the band offset transitivity rule [36].

3.3 The solar cell structure

A conventional thin-film layer structure used in chalcopyrite solar cells and the corresponding energy band diagram is schematically illustrated in Figure 3.2. It consists of a substrate (not shown), a back contact, a p-type absorber, a stack of transparent n-type materials (i.e. the window layers), and a metal grid. The materials used for each layer can vary, and different CIGS-module manufacturers have historically used slightly different structures, although the fundamental device structure is the same [37].

In this thesis, all solar cells are in general compared to cells fabricated with the CdS/i-ZnO/ZnO:Al window layer structure used in the Ångström baseline structure summarized in Table 3.1. The Ångström baseline structure is deemed a good representation of the industry standard, thus allowing for relevant comparisons when evaluating alternative materials (e.g. modified window layer structures). The role of each layer is briefly discussed in the following sub-sections.

Figure 3.2. A schematic illustration of a conventional thin-film layer stack used in chalcopyrite solar cells and the corresponding energy band diagram in short-circuit and dark conditions.

Table 3.1. Baseline CIGS solar cell structure at the Ångström laboratory.

	Material	Deposition process	Typical thickness	Typical sheet resistance (Ω/square)
Substrate	Soda-lime glass		1−3 mm	
Back contact	Molybdenum	DC sputtering	350 nm	0.6
Absorber	CIGS	Co-evaporation	2 µm	
Buffer layer	CdS	CBD	50 nm	
Intrinsic layer	ZnO	RF sputtering	90 nm	$7 \cdot 10^4$
Transparent front contact	ZnO:Al	RF sputtering	225 nm	40
Metal grid	Ni/Al/Ni stack	Electron beam evaporation	3 µm	

3.3.1 Substrate

The fundamental purpose of the substrate is to provide a mechanical support for the solar cell structure. Other important parameters are the surface roughness, thermal expansion coefficient [38], thermal stability (e.g. melting point or glass transition temperature), and the alkali-metal content.
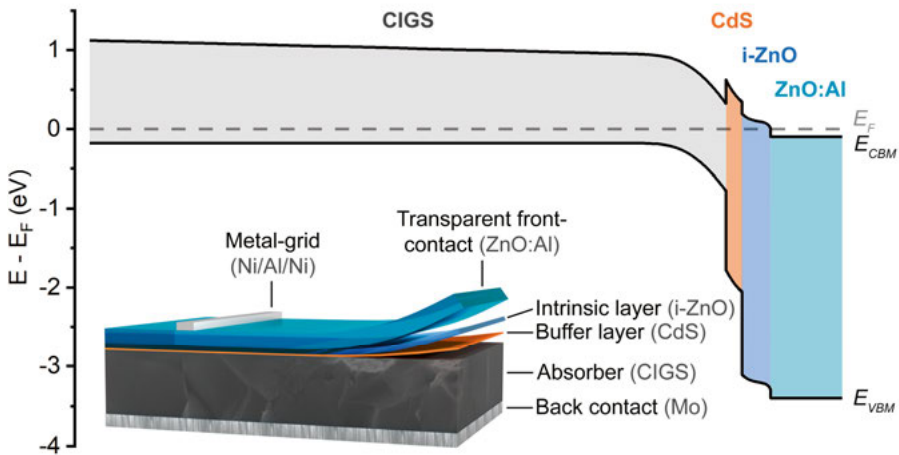
The conventional substrate for CIGS solar cells is soda-lime glass (SLG), which not only has suitable thermomechanical properties, but also provides a supply of sodium that can diffuse into the CIGS absorber during the CIGS deposition process [23]. Noteworthy alternatives to SLG are steel foil and polyimide substrates, which enable roll-to-roll manufacturing of flexible and low-weight modules [39], thereby potentially reducing production- and installation-related costs.

SLG substrates were generally used in all solar cell structures in Paper I, II, III and V. A high strain-point glass with a high potassium content was used for an improved CGS solar cell in Paper II, which enabled a higher absorber deposition temperature and incorporation of potassium into the absorber. In addition, partial solar cell structures were deposited on Cr/Au-coated quartz monitor crystals in Paper VI.

3.3.2 Back contact

The back contact should exhibit a high lateral conductivity, form a low-resistivity ohmic contact to CIGS, and should not degrade during the subsequent CIGS deposition process [40]. Other important aspects are the diffusion of alkali metals (if using alkali metal containing substrates) and the adhesion of the absorber layer.

Molybdenum is typically used as the back contact material, and is usually deposited by DC sputtering in a two-step process with varying argon pressure, to achieve a compromise between lateral conductivity and SLG/Mo

adhesion [41]. Furthermore, a MoSe$_2$ layer tends to form at the Mo/CIGS interface, which is generally regarded beneficial and proposely results in good Mo/CIGS adhesion and low contact resistance [40,42]. However, transparent alternatives in the form of various transparent conducting oxides (TCOs) have been evaluated for various applications [43–46], one example being bifacial solar cells that can be used in semi-transparent solar cell windows.

DC sputtered molybdenum back contacts were used in all solar cell structures in this thesis.

3.3.3 Absorber

The main properties of CIGS have already been described in Section 3.2. There are multiple ways to deposit high quality CIGS (and other chalcopyrite absorber layers), but most established methods are based on one of two main routes [47], either via (i) co-evaporation from elemental sources, or via (ii) a two-step process where a precursor layer is first deposited (e.g. by sputtering) and is then selenized/sulfurized in a second step. Regardless of deposition method, the absorber layers are usually deposited with an intentional gradient in gallium content (and sulfur content if applicable). There are several different grading strategies, but the main purpose is to decrease the electron affinity closer to the back contact to form a back-surface electric field that repels electrons from the back contact towards the depletion region [48]. This effectively reduces the recombination rate in the quasi-neutral region and at the back contact interface.

Different processes were used to deposit the absorber layers when fabricating the solar cells presented in this thesis. In Paper I and III, CIGS absorbers were deposited on full-size module substrates (60×120 cm^2) by Solibro Research AB using an in-line co-evaporation process. This way, all absorber material used within each experimental series originated from the same CIGS batch. This effectively removed most of the experimental variation related to varying absorber properties, which enabled the observation of weaker effects on solar cell performance when investigating modifications of the window layer structure. Similarly, in Paper V, ACIGS absorbers were also deposited by co-evaporated by Solibro Research AB. In Paper II and VI, an in-house co-evaporation process was used to deposit CIGS (and CGS). The depositions were performed in a Balzer BAK 550 vacuum chamber and copper, indium and gallium were evaporated from open-boat sources and selenium from an effusion cell. The evaporation rates were controlled in a feedback system where the rates, monitored by quadruple mass spectrometry (Balzer QmG 420), were used to regulate the heating of the sources.

3.3.4 The window layer structure

The window layer structure, as a unit, can be regarded to have a few principal purposes: (i) to form the n-type half of the p–n junction, (ii) to minimize recombination near the absorber/window interface, and (iii) to conduct the current to the metal grid. Clearly, the window layers must also be as transparent as possible so the incoming light reaches the absorber.

The structure and function of the window layer structure is the main topic of this thesis. How the properties of the individual layers, and related processes, affect the solar cell performance is discussed in more detail in Chapter 6, with emphasis on the buffer layer. Here, the roles and the most commonly used materials are outlined for each layer.

The stack is traditionally formed by three layers: a buffer layer, a resistive intrinsic layer, and a highly conductive transparent front contact.

3.3.5 Buffer layer

The buffer layer is essentially used to control the recombination rate near the absorber/buffer interface, primarily by ensuring favorable band offsets at the absorber/buffer interface and by reducing the interface defect density. It also affects the band bending in the absorber, with influence from the other layers in the window layer structure.

The industry standard has historically been to use CdS buffer layers, deposited by CBD [37,49,50]. However, CdS has a relatively narrow bandgap (E_g = 2.4 eV), which typically results in parasitic absorption of the incoming light that does not contribute to the photocurrent. CdS is thus not a perfect buffer layer material. There are also additional concerns regarding implementing a CdS CBD process in a production line. Cadmium and its compounds are known to be carcinogenic and suspected to be mutagenic and toxic to reproduction, and their use is heavily regulated in many countries, e.g. in the European Union under the framework of REACH [51].

Alternative buffer layers have been investigated for a long time (since around 1992), where the first cadmium-free buffer layers were ZnS and In(OH)$_3$ grown by CBD [49]. Today, the best CIGS solar cell, with a certified efficiency of 23.4%, was fabricated by Solar Frontier using a CBD-grown ZnO$_{1-x}$S$_x$ buffer layer in combination with ALD-grown Zn$_{1-x}$Mg$_x$O as second buffer layer [52]. However, using CBD processes for buffer layer deposition is not optimal. Partly because of the large volumes of liquid chemical waste that must be handled, but also because it is not performed in vacuum (unlike the other process steps) which interrupts the vacuum process chain. It would therefore be preferred to rely solely on vacuum-based buffer layer processes, such as evaporation, sputtering or ALD.

This thesis emphasizes on the properties and/or development of ALD buffer layers. An exception being Paper I, where only CdS buffer layers were used, deposited with the Ångström laboratory baseline CBD process, where the films are grown at 60 °C in an aqueous solution of cadmium acetate (3.2 M), thiourea (0.25 M) and ammonia (1.2 M) [53]. ALD $Zn_{1-x}Sn_xO_y$ (commonly abbreviated ZTO) buffer layers were used in Paper II and ALD $ZnO_{1-x}S_x$ buffer layers were used in Paper III. In Paper IV, a new ALD process was developed to grow amorphous $Sn_{1-x}Ga_xO_y$ (a-SGO)[†], which was evaluated as a new buffer layer material in Paper V. Both ALD $Zn_{1-x}Sn_xO_y$ and $Sn_{1-x}Ga_xO_y$ were used in Paper VI, where the growth of ternary oxides on CIGS was studied. See Chapter 5 for details regarding ALD of buffer layers.

3.3.6 Intrinsic layer

A resistive intrinsic (i.e. not intentionally doped) layer of ZnO (i-ZnO) is often included between the buffer layer and the transparent front contact. This layer can reduce the impact of possible shunt paths in the solar cell, but does not necessarily affect the performance in the absence of shunts [54]. However, there are other potential effects of the intrinsic layer (e.g. light-induced metastability, long-term stability, and band bending) that depend on the specific window layer structure and the corresponding process steps, which is briefly discussed in Section 6.6.

A relatively common alternative is to use a $Zn_{1-x}Mg_xO$ layer which has a wider bandgap than ZnO and therefore reduces the parasitic absorption [55].

RF-sputtered i-ZnO layers ($\rho \approx 0.6$ Ω·cm) were used in Papers I, II and III. In addition, more resistive i-ZnO layers ($\rho > 500$ Ω·cm) prepared by chemical vapor deposition (CVD) were used in Paper I for comparison. The intrinsic layer was omitted from the window layer structure in Paper V.

3.3.7 Transparent front contact

The role of the transparent front contact is to laterally transport the current to the metal grids. The two most important properties of this layer are the optical transparency and the lateral conductivity. Therefore, various TCOs are typically used, where the most common choice is sputtered ZnO:Al. TCOs are typically highly doped n-type semiconductors. Unfortunately, good electrical conductivity and high transparency can be difficult to achieve simultaneously. The conductivity in (n-type) TCOs is proportional to the charge carrier density and electron mobility. However, a high charge carrier density results in so-called free-carrier absorption. Therefore, a high mobility of at least

[†]Note the unfortunate inconsistency in the abbreviations ZTO and a-SGO, where both letters "T" and "S" represent Sn.

around 50 $cm^2/(V \cdot s)$ is required to reduce the need for a high charge carrier density. An example of high mobility TCO material is doped In_2O_3 (e.g. with H, Ti, Zr, Mo or W as dopant) [56,57].

RF-sputtered ZnO:Al TCOs were used in Paper I, II, III and V. In addition, ALD-grown In_2O_3:H layers were used in Paper I for comparison.

3.3.8 Metal grids and scribing

Metal grids are used to collect the current from the transparent front contact and conduct the current to the external circuit. The design of the grid is a compromise between shading the absorber and minimizing the distance the current is transported in the TCO (i.e. minimizing series resistance). Note that this also depends on the sheet resistance of the TCO layer. The grid used at Ångström laboratory consists of a Ni/Al/Ni multi-layer stack, which is deposited by evaporation through a shadow mask.

Arrays of laboratory solar cells are defined by mechanical scribing, where all layers are removed, down to the back contact, in a pattern surrounding well-defined areas (generally 0.5 cm^2 for the solar cells discussed in this thesis). Each solar cell can then be individually characterized.

Ni/Al/Ni grids and 0.5 cm^2 cell areas were used in Paper II, III, and V. The number of solar cells per sample was in the range 12–32, depending on the total sample area. In Paper I, the grid was omitted and a cell area of 0.1 cm^2 was used, with a sample size of up to 50 cells. The large sample size allowed for a better estimation of lateral variations in solar cell performance.

3.4 Efficiency loss mechanisms

Two types of loss mechanisms prevent chalcopyrite solar cells from reaching the fundamental upper efficiency limit discussed in Section 2.5—optical and electrical losses. It is only by reducing these losses the solar cell efficiency can be improved for single-junction solar cells.

The main optical losses are due to (i) shading from the metal grid, (ii) reflection from the window layer structure and absorber surface, (iii) absorption before the light reaches the absorber (i.e. parasitic absorption in the window layer structure), and (iv) incomplete absorption in the absorber. These mechanisms primarily reduce J_{sc}, due to the simple reason that fewer photons are absorbed in the absorber material. The actual extent of each effect on cell efficiency depends slightly on other factors, such as absorber bandgap, window layer structure and grid design. All the same, a comparison can be made by considering the case of high-efficient CIGS solar cells. The relative influence of losses on the efficiency for different loss mechanisms is therefore

listed in Table 3.2, which were estimated in ref. [17] for two previous record CIGS solar cells with efficiencies of 19.9% and 20.3%, respectively [58,59]. It may seem like losses from optical reflection influence the efficiency the most, among the optical loss mechanisms. However, the reflectance of non-encapsulated research cells is not representative of the reflectance of encapsulated solar cell modules, where instead absorption in a thicker TCO layer and front glass is more significant. Furthermore, the reflectance can be reduced by implementing anti-reflective coatings (ARCs), which was done for the record cells. If reflection losses are disregarded, the optical losses correspond to around 8–10% of the total deviation from the upper efficiency limit. These losses can be reduced by improving the grid design and the window layer structure.

The main electrical losses are (i) power dissipation due to series resistance, (ii) conduction through shunt paths, and most important (iii) charge carrier recombination. However, the effects from series resistance and shunt conductance are marginal compared to the recombination losses, which were responsible for a 30% efficiency loss in the example of high-efficient CIGS solar cells, as shown in Table 3.2. Collection losses accounted for 5% and are due to a reduction in J_{sc}, caused by recombination of charge carriers that are photo-generated further into the quasi-neutral region of the absorber. This effect is affected by the depletion region width and the charge-carrier diffusion length. The other 25% are due to decreased V_{oc} (and FF), which can be understood from an increase in the one-diode model parameters J_0 (recombination) and A. In fact, the V_{oc} deficit, often approximated as $E_g/q - V_{oc}$, is a common measure of the total recombination in a solar cell.

Table 3.2. Effect on efficiency for different loss mechanisms present in CIGS record solar cells, as estimated in ref. [17] for previous record CIGS solar cells with efficiencies of 20% and CdS buffer layers.

Loss mechanism	$|\Delta\eta|/\eta$ (%)
Shading from grid	2–4
Reflection from window layer structure	9[†]
Optical absorption in window layer structure	6
Collection losses due to recombination	5
High series resistance	2–4
Shunt conductance	<0.1
Other recombination losses	25

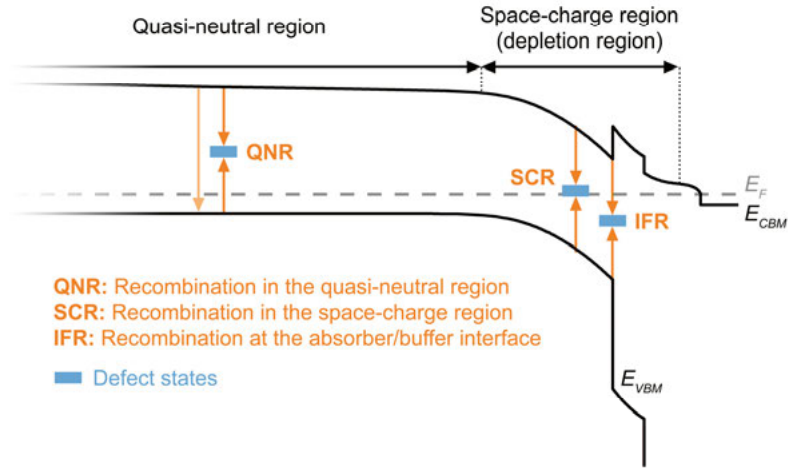[†]Before applying an anti-reflective coating

Figure 3.3. Primary recombination paths in chalcopyrite solar cells, excluding recombination at the back contact.

The primary recombination paths in chalcopyrite solar cells are displayed in Figure 3.3 [13]. They are (tunneling-enhanced) recombination at the absorber/buffer interface, (tunneling-enhanced) recombination in the space-charge region, recombination in the quasi-neutral region, and recombination at the back contact (not shown in Figure 3.3). Although each recombination path contributes to the total recombination loss, some path tends to dominate. The recombination rates for different recombination paths were reported for a recent CIGS record cell with a 22.9% efficiency, where recombination in the space-charge region was dominating [60]. As mentioned in Section 2.2, SRH recombination is the main type of recombination, where a high defect density at the mid-gap energy is most severe. In CIGS, the most detrimental trap states have been proposed to originate from V_{Se} and/or cation anti-site defects [61]. However, it is unclear to what extent deep defects affect the efficiency in state-of-the-art solar cells. It has been suggested that an enhanced radiative recombination caused by potential (or bandgap) fluctuations significantly contributes to the recombination losses [17,62]. Interestingly, band bending and band tailing around grain boundaries are suspected to contribute to this [63], which might challenge the notion that the grain boundaries in CIGS are completely benign.

The recombination in wide-bandgap C(I)GS absorbers can be different than in the narrow-bandgap equivalents. It has been generally observed that the V_{oc} deficit increases with gallium content in CIGS/CdS solar cells [64]. This can partly be explained by an increased bulk defect density, but there are also several other possible explanations. Firstly, when the composition approaches pure CGS, it is not possible to create a back-surface field by gallium grading. Secondly, both defect states and the Fermi level at the absorber/buffer interface shift towards the mid-gap energy, resulting in an increased interface

recombination rate [65]. Lastly, the conduction band alignment between the absorber and the CdS buffer layer becomes unsuitable for large gallium contents, which also enhances the interface recombination rate (see Section 6.2).

In the perspective of window layer development, improving the window layer structure offers different potential rewards for different absorbers. For example, minimizing optical losses and the production cost of high-efficient state-of-the-art CIGS solar cells may be more valuable than slightly reducing the interface recombination, while the potential benefit of improved window layer structures (buffer layer in particular) may be greater for wide-bandgap absorbers.

3.5 CIGS post-deposition treatments

Since year 2013, post-deposition treatment (PDT) of the absorber surface with alkali-metal fluorides has been included in the processing of state-of-the-art solar cells (notably with KF, RbF and CsF) [60,66,67]. The influence of PDT on the electrical and material properties of CIGS is by now well characterized [63]. In terms of solar cell performance, the main effect is an increased V_{oc}. In addition, PDT enables the use of thinner CdS buffer layers when grown by CBD, resulting in an increased J_{sc} due to reduced parasitic absorption. It is still uncertain which mechanism explains the majority of the V_{oc} gain (i.e. recombination reduction), and both reductions in interface and bulk recombination have been previously reported. However, it has been suggested that the improvement of bulk properties (including grain boundaries) is the most consistent explanation considering the available data in the literature [63].

A KF-PDT process induces an extensive modification of the CIGS surface, where the main effects are schematically shown in Figure 3.4. In general, the CIGS surface is typically depleted in copper and gallium after PDT, and a $KInSe_2$ phase is formed at/near the surface. In addition, the process results in residual salts on the surface (KF and one or more water-soluble compounds that contains gallium and fluorine).

X: Ga & F containing compound
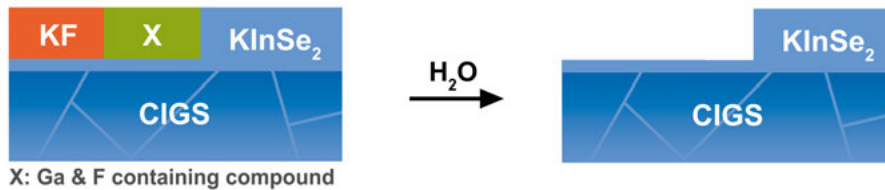
Figure 3.4. Schematic illustration of which phases are present at the CIGS surface after KF-PDT and after a subsequent water rinse.

If CBD is used to deposit the buffer layer, the salts are dissolved prior to buffer layer growth. However, this is more challenging in a vacuum-based process, where the salts typically remain at/near the absorber/buffer interface. How this was found to complicate the processing of ALD-based buffer layers is discussed in Section 6.5.

A similar surface modification also occurs for other alkali-metal fluorides, at least for RbF. In addition, the modification is similar when applying KF- and RbF-PDT to ACIGS absorbers, where silver is also depleted near the surface [68,69].

4. Characterization and simulation methods

The development of window layer structures for solar cells is assisted by a detailed understanding of the electrical and material properties of the solar cells as well as of the individual layers and interfaces. For this reason, numerous different characterization methods were employed in this thesis, as summarized in Table 4.1 and 4.2. This section describes the techniques used for photoelectrical characterization of the solar cell devices, whereas brief descriptions of the various methods used to analyze material properties, which are more widely used in multiple research fields, can be found in Appendix A.

Table 4.1. Summary of material characterization techniques used in this thesis.

Method	Information obtained	Used in paper:
GDOES	Compositional depth profiles	III, V
R–T spectroscopy	Reflectance of solar cells	III, V
	Optical bandgaps	IV, V
Four-terminal resistivity sensing	Sheet resistance	I, IV
SEM	Film morphology	II
	Film morphology and topography	VI
STEM	Film morphology (imaging)	IV, V
	Compositional distribution (EELS and EDS)	III[S], IV, V
	Degree of crystallinity (diffraction)	IV
RBS	Film composition	IV
ToF–ERDA	Impurity content	IV
XRD	Absorber texture, shifts in unit cell parameters	II
XRR	Film thickness and density	IV
XRF	Average composition	I–VI
	Film thickness	I–III, V,VI
XPS	Surface chemistry (qualitative)	III[S], VI
Synchrotron-based XPS and HAXPES	Valence band offset	V
J–V and C–V of MOSCAPs	Various electrical properties	V

[S] Included in paper as supplementary information

Table 4.2. Summary of photoelectrical characterization techniques used in this thesis.

Method	Information obtained	Used in paper:
EQE	Quantum efficiency, $J_{sc,EQE}$	I, II, III, V
J–V	Solar cell parameters	I, II, III, V
J–V(T)	Recombination activation energy	II

4.1 Photoelectrical characterization

4.1.1 Quantum efficiency measurements

Quantum efficiency measurements are very valuable for analyzing collection losses in the absorber and optical losses in the window layer structure. The quantum efficiency is the ratio of the number of collected charge carriers per incoming photon and wavelength. Two variants of quantum efficiency are usually considered, the external quantum efficiency (EQE) and the internal quantum efficiency (IQE). The difference is that EQE is based on the incoming photon flux, whereas IQE only considers the photons that are absorbed in the solar cell.

EQE can be obtained by measuring the spectral response (SR), which is the ratio of the current density output from a solar cell per incoming radiative flux, at a specific wavelength:

$$EQE(\lambda) = \frac{hc}{q\lambda} SR(\lambda) = \left(\frac{hc}{q\lambda}\right)\left(\frac{J(\lambda)}{E_{e,\lambda}}\right) \tag{4.1}$$

where c is the speed of light and $E_{e,\lambda}$ is the spectral irradiance ($[\text{W}\cdot\text{m}^{-2}\cdot\text{nm}^{-1}]$). Note that $J(\lambda)$ in Eq. 4.1 is the short-circuit current density at wavelength λ. An EQE measurement can thus be used to determine the expected J_{sc} value for the standard AM1.5G spectra (or any arbitrary spectra):

$$J_{sc,EQE} = \frac{q}{hc} \int (\lambda \cdot EQE(\lambda) \cdot E_{e,\lambda}) \, d\lambda \tag{4.2}$$

It can sometimes be more useful to analyze the IQE curves, e.g. when comparing the quantum efficiency of devices with different reflectance. If the reflectance R is known, IQE can be calculated with the simple expression

$$IQE(\lambda) = \frac{EQE(\lambda)}{1 - R(\lambda)} \tag{4.3}$$

This expression can also be modified to exclude parasitic absorption in the window layer structure.

In this thesis, EQE measurements were performed at 25 °C on all solar cell samples (note that there are several cells per sample). The experimental set-up employed monochromatic light generated by a Xenon arc lamp in a dual-beam optical system, in which the light intensity was constantly monitored by reference diodes and was calibrated with Si and InGaAs reference diodes with known spectral responses. The measurements were in general performed in an ambient light condition.

4.1.2 J–V measurements

The performance of a solar cell is ultimately measured by the conversion efficiency, which is extracted from the solar cell J–V characteristics, as previously described in Section 2.4. J–V measurements are performed at so-called standard test conditions, to allow for a universal comparison between solar cells. The standard test condition (for non-concentrated solar cells) is that the illumination corresponds to an AM1.5G standard spectrum irradiance [16], the device temperature is 25 °C, and the efficiency is calculated for the total area [70]. The AM1.5G spectrum corresponds to 1000 W/m^2 of direct and diffuse light and with a spectral distribution equivalent to light traveling 1.5 times the atmosphere (air mass). In this work, these criteria were ensured by (i) using a temperature-controlled sample stage, and (ii) calibrating the light intensity after EQE measurements, to compensate for the spectral mismatch between the light source used (a tungsten halogen lamp) and the AM1.5G spectrum.

4.1.3 Temperature dependent J–V measurements

To obtain information about the dominating recombination paths, it is possible to study the temperature dependence of V_{oc} by performing multiple J–V measurements under illumination at different temperatures (i.e. a J–V(T) measurement) [71].

The dark saturation current density can be expressed as

$$J_0 = J_{00}e^{-\frac{E_A}{AkT}} \tag{4.4}$$

where E_A is the activation energy of the dominating recombination path and J_{00} is a pre-factor weakly dependent on temperature.

By inserting Eq. 4.4 in the one-diode model (Eq. 2.4) and assuming that $1/R_{sh} = 0$, the following expression for V_{oc} can be obtained after some rearrangements:

$$V_{oc} \approx \frac{E_A}{q} + \frac{AkT}{q} \ln(\frac{J_L}{J_{00}}) \qquad (4.5)$$

If J_{00} and A are constant and not dependent on temperature, E_A can be extracted from the linear relationship between V_{oc} and T. The interpretation of E_A should be carefully considered. However, a common interpretation is that interface recombination is the dominating recombination path if $E_A < E_g$ [71].

A similar analysis can be performed for dark J–V(T) measurements [72], by making use of the relationship

$$A \cdot ln(J_0) = -\frac{E_A}{kT} + A \cdot \ln(J_{00}) \qquad (4.6)$$

which is also a reorganization of Eq. 2.4 and Eq. 4.4. Here, A and J_0 can be extracted by fitting the one-diode model to experimental data, after which E_A is obtained from the slope when plotting $A \cdot ln(J_0)$ against $1/T$, again assuming that A is independent of temperature.

In Paper II, E_A was extracted from both illuminated and dark J–V(T) measurements, which were performed in a liquid-nitrogen cooled cryostat. A white light-emitting diode was used as light source, with the light intensity calibrated to room-temperature EQE measurements.

4.2 Solar cell simulations

Numerical simulations can be useful to understand how various material properties of the different layers can influence the solar cell properties. In Paper I, the one-dimensional simulation tool SCAPS (solar cell capacitance simulator, [73]) was used to solve the fundamental semiconductor equations (Poisson equation and continuity equations) for various solar cell structures. Simulations were mainly used for demonstrational purposes, rather than for inference, to visualize how various changes in window layer properties (intrinsic layer thickness and charge carrier concentration) can affect the energy band structure.

5 Atomic layer deposition of buffer layers

ALD is a high-precision deposition method where thin films are grown in a sequential manner, from self-terminating reactions between gaseous precursors and the surface. Highly conformal, uniform and pinhole-free films can be grown over large substrate areas at relatively low deposition temperatures, with excellent control in both film thickness and composition. ALD is also suitable for deposition on sensitive substrates that are prone to sputtering-induced damage. In addition, an ideal ALD process is quite insensitive to reactor geometry and is compatible with large-scale production. The drawbacks are primarily a low deposition rate and an inefficient utilization of chemicals (i.e. material yield) compared to sputtering or evaporation processes (>50% unreacted precursors in ALD [74]). However, the chemical utilization in ALD is still considerably better than when growing CdS with CBD [75].

ALD processing of alternative buffer layers has long been regarded an attractive option and several different materials have been evaluated over the years. Some early examples are buffer layers based on ZnO, In_2S_3, and ZnSe [49], whereas $ZnO_{1-x}S_x$, $Zn_{1-x}Sn_xO_y$, and $Zn_{1-x}Mg_xO$ are more frequently used today. The ALD buffer layers that have been used to fabricate chalcopyrite solar cells with efficiencies above 15% are summarized in Table 5.1, along with the highest known efficiencies achieved.

Table 5.1. List of ALD buffer layers that have been used to produce chalcopyrite solar cells with cell efficiencies above 15%.

Buffer layer	Best η	T_{ALD} (°C)	d (nm)	X	ARC	Year	Ref.
With CIGS absorbers							
In_2S_3	16.4%	220	30		NO	2003	[76]
$Zn_{1-x}Mg_xO$	18.1%	120	150	0.2	YES	2007	[77]
$Zn_{1-x}Sn_xO_y$	18.2%	120	13	0.17	YES	2013	[53]
$ZnO_{1-x}S_x$	19.8%	125	50	0.33	YES	2016	[78]
With ACIGS absorbers							
$ZnO_{1-x}S_x$	19.2%	125	33	0.37	YES	2017	IN-HOUSE[†]
$Zn_{1-x}Sn_xO_y$	19.1%	125	40	0.18	YES	2019	IN-HOUSE[†]
$Sn_{1-x}Ga_xO_y$	17.0%	125	14	0.25	NO	2019	Paper V

[†]Unpublished in-house measurement

Two noteworthy examples that are not included in Table 5.1 are the use of ALD $Zn_{1-x}Sn_xO_y$ and $Zn_{1-x}Mg_xO$ buffer layers for the record efficiency solar cells based on the wide-bandgap absorbers CGS (η = 11.9%, Paper II) and Cu(In,Ga)S$_2$ (η = 15.5%, [79]). As indicated by Table 5.1, most alternative buffer layer materials today are ternary compounds. A very attractive property that ternary compounds can possess is the ability to tune the conduction band alignment by controlling the buffer layer composition.

In order to develop ALD-based buffer layers in an efficient manner, it is necessary to have a good understanding of the ALD process. This section provides an introduction to fundamental ALD theory and aims to cover the most important aspects when using ALD to deposit metal-oxide-based buffer layers. Note that only conventional thermal-activated ALD is treated here, i.e. not plasma-enhanced ALD (PE-ALD).

5.1 Thin-film growth in thermal-activated ALD

5.1.1 The ALD cycle

ALD is based on sequential self-terminating reactions between gasous precursors and the growing film. The sequence of precursor pulses that is repeated throughout the ALD process is called an ALD cycle. These can be more or less complex, depending on the process. Nonetheless, an illustrative example of metal oxide growth with a typical ALD cycle is displayed in Figure 5.1, where a metal complex and water serve as precursors. As seen in the figure, each unique precursor pulse is separated by purge pulses using an inert gas (e.g. N$_2$).
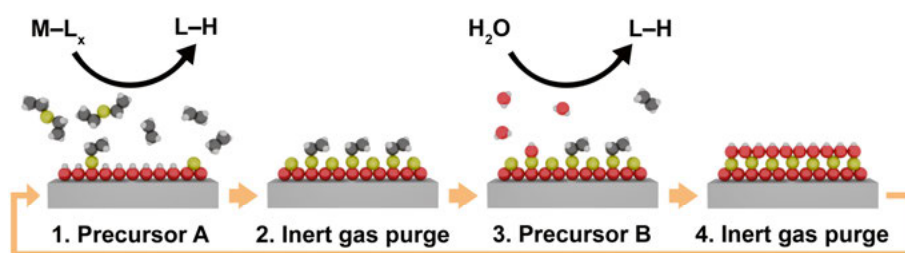

Figure 5.1. A typical ALD cycle for growing a metal oxide from a metal precursor and water, where M is a metal cation and L represents an arbitrary ligand.
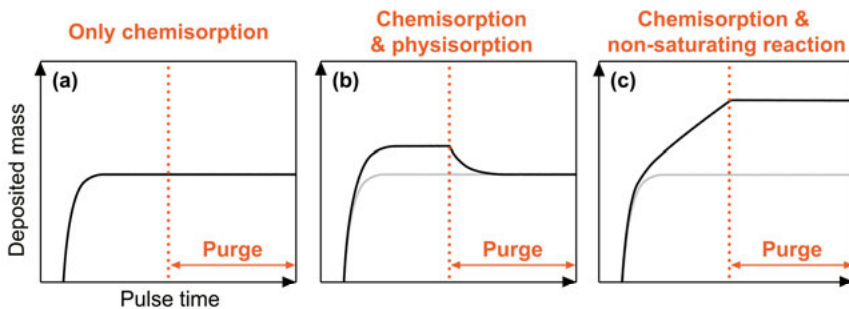
Figure 5.2. Mass gain during the metal-precursor pulse and subsequent purge pulse, assuming (a) chemisorption, (b) mixture of chemisorption and physisorption, and (c) chemisorption with contribution from a non-saturating reaction.
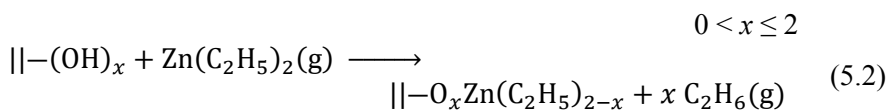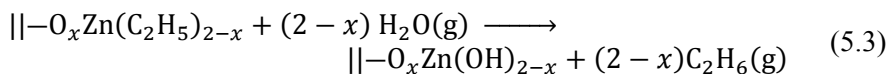
5.1.2 Adsorption mechanisms

During a precursor pulse, molecules adsorb to the growing surface by either chemisorption or physisorption. In chemisorption, the precursor adsorbs irreversibly and forms new strong chemical bonds to the surface (e.g. ionic or covalent bonds) in contrary to physisorption, where the adsorption is energetically driven by weak interactions between the precursor and the surface (e.g. van der Waals interactions). Only the irreversible adsorption contributes to ALD growth in an ideal case. How the mass changes during an ideal metal precursor pulse and the following purge is shown in Figure 5.2 for three different scenarios: (i) adsorption entirely by chemisorption, (ii) a mixture of chemisorption and physisorption, and (iii) chemisorption with a contribution from a non-saturating reaction (e.g. due to thermal decomposition of surface species [80], or system leaks).

The chemisorption process is commonly explained by a simple ligand-exchange mechanism [81]:

$$||-a + ML_n(g) \longrightarrow ||-ML_{n-1} + aL(g) \tag{5.1}$$
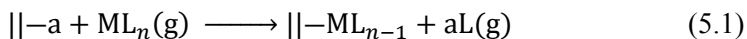
where "$||-a$" is a reactive surface group. Note that the ligand-exchange reaction can also occur for more than one ligand, i.e. the cation can form more than one chemical bond to the surface. Two other common chemisorption mechanisms identified in ALD processes are dissociation and association reactions [81]. Nonetheless, if a ligand-exchange mechanism is assumed for ALD of ZnO from diethylzinc [DEZn or $Zn(C_2H_5)_2$] and water, the corresponding ALD half-reactions (i.e. reactions during respective precursor pulse) would be:

$$0 < x \leq 2$$
$$||-(OH)_x + Zn(C_2H_5)_2(g) \longrightarrow$$
$$||-O_xZn(C_2H_5)_{2-x} + x\ C_2H_6(g) \tag{5.2}$$

$$||-O_xZn(C_2H_5)_{2-x} + (2-x)\,H_2O(g) \longrightarrow$$
$$||-O_xZn(OH)_{2-x} + (2-x)C_2H_6(g) \quad (5.3)$$

where x is the number of ligands exchanged per chemisorbed species. Note that the surface in question is –OH terminated both in the beginning of the first half-reaction and at the end of second half reaction, i.e. in the beginning and end of an ALD cycle.

5.1.3 What limits the growth per cycle?

The "growth rate" in ALD is sometimes reported as the growth per cycle (*GPC*) in literature, with unit [Å], although the actual growth rate in units [Å/s] is a function of *GPC* and pulse times.

Despite the name *atomic layer* deposition, it is seldom the case that a complete crystallographic monolayer is deposited in each cycle. *GPC* is limited by the surface density of precursors that are able to chemisorb onto the surface before the surface is saturated. In turn, this is controlled either by the availability of reactive surface sites (e.g. –OH groups) or by steric hindrance, where the highest possible amount of adsorbed precursors is simply determined by the size of the precursor (ligands).

Many ALD processes exhibit nearly constant *GPC* within a certain temperature window. This can be the case when steric hindrance controls the saturation and the number of reactive surface sites have no influence (although the temperature can also influence steric hindrance if the chemisorption mechanism changes) [81]. In other cases, the temperature can have a larger effect on *GPC* for numerous reasons, e.g. reduced surface density of reactive surface sites for higher temperatures or by enabling/disabling reaction paths.
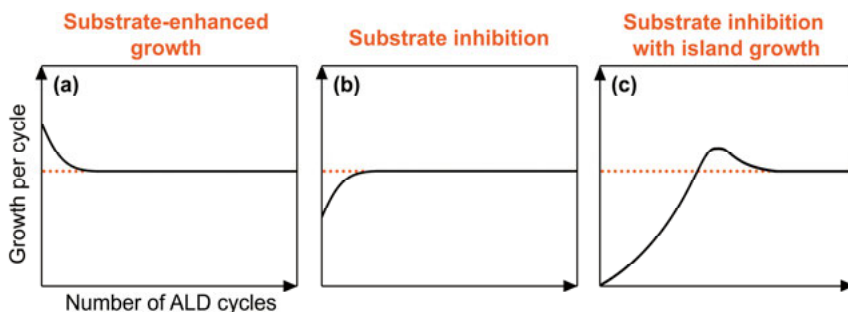

Figure 5.3. Different ways *GPC* can vary with number of cycles in an ALD process. (a) Substrate-enhanced growth, (b) substrate-inhibited growth, and (c) substrate-inhibition with island growth. The dotted lines represents constant *GPC*. The figure is adapted from ref. [81].

GPC can be different in the beginning of the ALD process, where the first ALD cycle(s) are performed on the substrate surface, whereas later ALD cycles are performed on a surface that is covered with the ALD-grown material. Figure 5.3 displays different ways the *GPC* can vary with number of cycles during an ALD process: (a) substrate-enhanced growth, surface-inhibited (b) layer-by-layer or (c) island growth. How *GPC* varies in the beginning of the growth can potentially influence the film properties close to the substrate, which can be observed when growing ternary compound buffer layers on CIGS (see Section 7.3).

5.2 Low-temperature ALD of ternary compounds

5.2.1 Precursors

A way to enable ALD growth at low temperatures is to use metal-organic compounds as precursors, which leads to low activation energies due to weak bonds between the ligands and the cation (another way is by employing PE-ALD). The metal-organic precursors used in this thesis to grow ZnO, ZnS, SnO_2 and Ga_2O_3 films, and their ternary compounds, are DEZn, tetrakis(dimethylamido)tin(IV) [DMA_4Sn or $Sn(N(CH_3)_2)_4$] and tris(dimethylamido)gallium(III)–dimer [DMA_3Ga–dimer, $Ga_2(N(CH_3)_2)_6$], which are shown in Figure 5.4. Water and/or H_2S were used as co-reactants. These precursors allow for ALD growth at temperatures even below 100 °C, which is low enough for solar cell processing. However, a drawback with most metal-organic precursors is that they have a tendency to leave contaminants in the films due to incomplete reactions [82], or by thermal decomposition of the precursors [83].

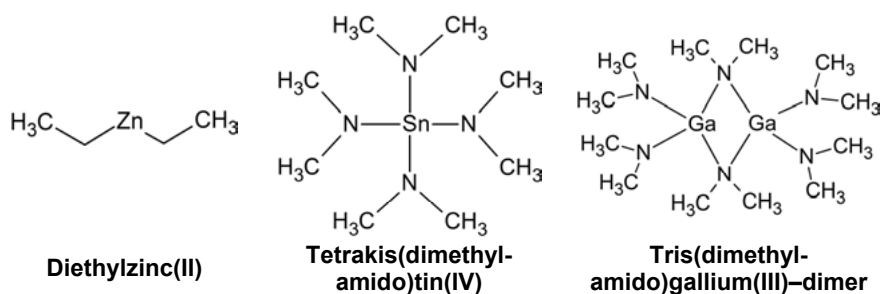**Diethylzinc(II)**   **Tetrakis(dimethyl-amido)tin(IV)**   **Tris(dimethyl-amido)gallium(III)–dimer**

Figure 5.4. Metal-organic compounds used as ALD precursors in this thesis to grow ZnO, ZnS, SnO_2, Ga_2O_3, and their ternary combinations.

5.2.2 Pulse scheme and composition control

Ternary compound buffer layers can be grown by ALD by employing a so-called super-cycle approach, where two binary ALD processes are combined and alternated throughout the process. An example pulse scheme for a $Zn_{1-x}Sn_xO_y$ process is:

$$(DEZn : N_2 : H_2O : N_2)_A : (DMA_4Sn : N_2 : H_2O : N_2)_B \qquad (5.4)$$

where $B/(A+B)$ or $A:B$ is the sub-cycle ratio. The film composition is controlled by the sub-cycle ratio, but the relationship is not necessarily linear. Figure 5.5 exemplifies how the composition and *GPC* varies with sub-cycle ratio in two ALD processes for $Zn_{1-x}Sn_xO_y$ and $ZnO_{1-x}S_x$ at substrate temperatures of 120 °C and 125 °C, respectively. The data are from refs. [84] and [85], where the same ALD reactors and similar process conditions were used as in this thesis.[†] In addition, the figure includes the expected composition and *GPC* as dashed lines based on a simple rule of mixtures (RoM) [86]. The rule of mixtures assumes that the material grown during each
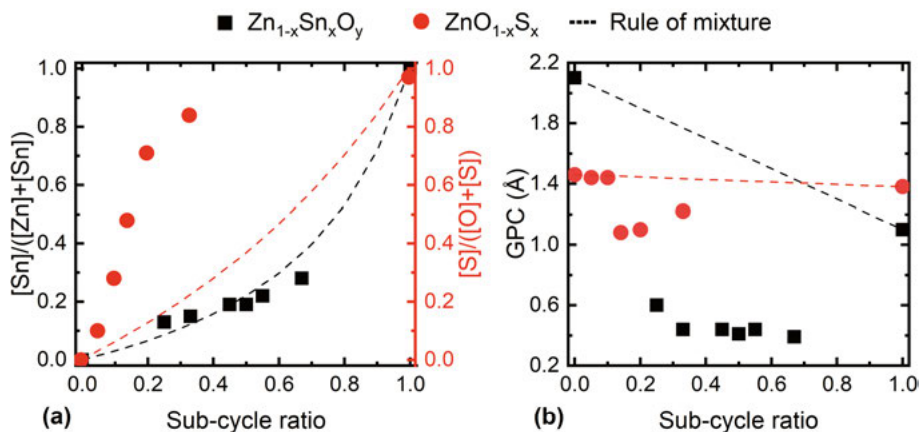
Figure 5.5. Example of (a) cation/anion ratio and (b) *GPC* as functions of sub-cycle ratio in ALD processes for $Zn_{1-x}Sn_xO_y$ and $ZnO_{1-x}S_x$. A sub-cycle ratio of $P = 0$ corresponds to ZnO. Values are from refs. [84] and [85].

[†]In this thesis, $Zn_{1-x}Sn_xO_y$ ALD was performed at 95–140 °C in an F-120 laminar-flow ALD reactor (ASM Microchemistry) with externally heated quartz substrate holders with room for two $5×5$ cm^2 sized substrates, where one can be replaced with a quartz crystal microbalance sensor head. The precursors DEZn and deionized H_2O were evaporated at room temperature, while TDM_4Sn was evaporated at 40 °C in a bubbler configuration using highly purified N_2 (99.9999%) as carrier gas. $ZnO_{1-x}S_x$ ALD was performed at 125 °C in a custom-built reactor that has room for one $12.5×12.5$ cm^2 sized substrate. No external heating of the precursors DEZn, H_2O and H_2S were applied. N_2 was used as inert transport and purge gas. The gas flows in both processes were regulated by needle valves in addition to a dual gas-regulator for H_2S.

sub-cycle is the same as if it was grown in a binary process, i.e. the ALD growth should not be affected by the mixing of sub-cycles. Under this assumption, GPC can be expressed as

$$GPC_{RoM} = P \cdot GPC_B + (1 - P) \cdot GPC_A \qquad (5.5)$$

where P is the sub-cycle ratio. Similarly, the expected cation ratio in $Zn_{1-x}Sn_xO_y$ and anion ratio in $ZnO_{1-x}S_x$ are expressed by

$$x_{RoM,ZTO} = \frac{[Sn]}{[Zn] + [Sn]} = \ldots$$
$$= \frac{1}{1 + \left(\dfrac{1-P}{P}\right)\left(\dfrac{M_{SnO_2}}{M_{ZnO}}\right)\left(\dfrac{\rho_{ZnO} \times GPC_{ZnO}}{\rho_{SnO_2} \times GPC_{SnO_2}}\right)} \qquad (5.6)$$

and

$$x_{RoM,Zn(O,S)} = \frac{[S]}{[O] + [S]} = \ldots$$
$$= \frac{1}{1 + \left(\dfrac{1-P}{P}\right)\left(\dfrac{M_{ZnS}}{M_{ZnO}}\right)\left(\dfrac{\rho_{ZnO} \times GPC_{ZnO}}{\rho_{ZnS} \times GPC_{ZnS}}\right)} \qquad (5.7)$$

where M is the molar mass and ρ is the film density for the respective binary compound. A derivation of the rule of mixtures for the cation ratio in ternary oxides is provided in Appendix B.

5.2.3 Non-ideal effects in ALD of $Zn_{1-x}Sn_xO_y$ and $ZnO_{1-x}S_x$

In Figure 5.5a, it can be observed that the cation ratio in $Zn_{1-x}Sn_xO_y$ roughly follows the rule of mixtures, in contrast to the anion ratio in $ZnO_{1-x}S_x$, where the sulfur concentration is much higher than expected from the rule of mixtures. The higher sulfur content is caused by exchange reactions between H_2S and the $ZnO_{1-x}S_x$ surface [85], similar to the bulk reaction between ZnO and H_2S:

$$ZnO(s) + H_2S(g) \longrightarrow ZnS(s) + H_2O(g) \qquad (5.8)$$
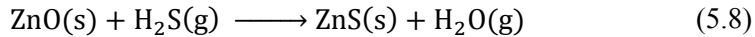
The reverse reaction also occurs. However, the reaction rate constant has been determined to be around 10^2 times higher for the exchange reaction with H_2S compared to with H_2O [87]. The presence of exchange reactions makes the film composition (and deviation from the rule of mixtures) sensitive to the substrate temperature and precursor exposure. This can be especially

problematic for large substrates (e.g. full-size solar cell modules) in which case the reactor should be carefully designed to ensure a uniform temperature and precursor partial pressure across the entire substrate area.

ALD of $Zn_{1-x}Sn_xO_y$ is not free from non-ideal effects either. The growth is inhibited when Sn–O sub-cycles are added to a ZnO process. This seems to be due to an inefficient ligand elimination during the H_2O pulse in the Zn–O sub-cycle performed after a Sn–O sub-cycle [82,88]. This is consistent with unpublished results showing that the *GPC* and degree of crystallinity of $Zn_{1-x}Sn_xO_y$ can be influenced by the water dose used.

5.3 In-situ monitoring of ALD growth using quartz crystal microbalance

ALD can be monitored by in-situ quartz crystal microbalance (QCM) to obtain information about the growth process. A monitor crystal (typically AT-cut quartz crystals with gold electrodes) is deposited during the ALD process, during which the crystal's resonance frequency (*f*) is monitored. The deposited film increases the effective mass of the crystal, which shifts the resonance frequency. For deposition of uniform rigid thin films measured in vacuum, the relationship between the frequency shift (Δf) and deposited mass (Δm) is well described by Sauerbrey's equation [89]:

$$\Delta f = -\frac{2f_0^2}{A\sqrt{\rho_q \mu_q}}\Delta m \tag{5.9}$$

where f_0 is the unloaded crystal's resonance frequency, A is the nominal area defined by the overlap between the front and back electrodes, ρ_q is the quartz density and μ_q is the shear modulus for AT-cut quartz crystals. The as-calculated mass is referred to as Sauerbrey's mass. This calculated value can in turn be calibrated with external measurements to allow for a more accurate determination of Δm. Constant temperature and pressure is assumed in Eq. 5.9. The frequency can be sensitive to temperature variations, which can result in measurement artifacts caused by a cooling/heating of the substrate during the ALD process. In the experimental set-up used in this work, the gas flow is pre-heated to match the substrate temperature.

A QCM recording of a SnO_2 ALD process is displayed in Figure 5.6 as an example. The filled background areas show the time intervals of the various precursor pulses, which were all 1 s in this process. The ligand-exchange mechanism in Eq. 5.1 can be used to explain the growth curve. The deposited mass distinctly increases during the metal precursor pulse, when heavy $Sn(DMA)_x$ species adsorb on the surface and lighter DMAH release until the
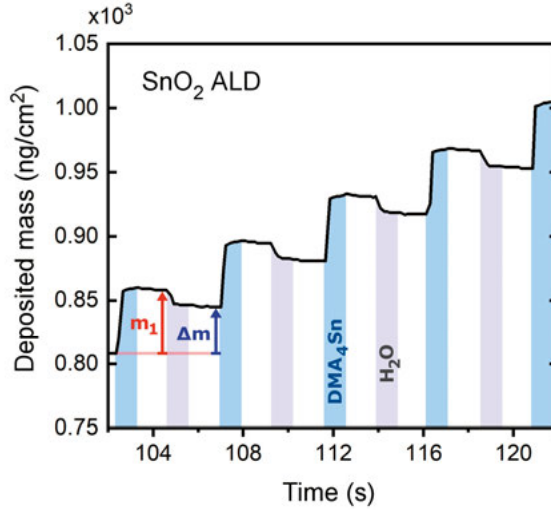
Figure 5.6. QCM recording of SnO$_2$ ALD at 175 °C. The precursors were DMA$_4$Sn and H$_2$O. The deposited mass after the first ALD half-reaction and after a complete ALD cycle is indicated by m_1 and Δm, respectively.

surface is saturated. In the second precursor pulse, the DMA ligands are replaced by lighter OH groups, which results in a net mass decrease.

The ratio between the mass increase after the first half-reaction (m_1) and the total mass increase after one ALD cycle (Δm) can reveal information about the chemisorption process if the ALD half-reactions are known. For example, if ALD of SnO$_2$ can be described by a ligand-exchange mechanism analogous to the half-reactions shown in Eq. 5.2 and 5.3 for ZnO, then it follows from the first half-reaction that

$$m_1 \propto M(\text{DMA}_4\text{Sn}) - x \cdot M(\text{DMAH}) \qquad (5.10)$$

and from the second half-reaction

$$\Delta m - m_1 \propto (4 - x) \cdot [M(\text{H}_2\text{O}) - M(\text{DMAH})] \qquad (5.11)$$

The average number of exchanged ligands, i.e. the average number of chemical bonds formed during chemisorption per metal precursor, can therefore be calculated from the ratio between m_1 and Δm. Note that even if the exact growth mechanism is not known with certainty, a shift in the mass ratio can indicate a shift in growth mechanism. For example, during an ALD process or when altering the sub-cycle ratio in a ternary ALD process.

6 Design of window layer structures

This section covers some of the most important aspects to consider when designing window layer structures for chalcopyrite solar cells. The primary aim is to minimize optical losses from parasitic absorption in the window layer structure and simultaneously minimize electrical losses from (near-)interface recombination and sub-optimal charge transport properties. This can be complicated by strong influences from the various interfaces and by interaction effects between the individual layers and/or process steps.

6.1 Reduction of the parasitic absorption

The parasitic absorption in the window layer structure occurs by either interband absorption or free-carrier absorption in the TCO.

Interband absorption primarily occurs by exciting an electron in the valence band across the bandgap to an unoccupied state in the conduction band. Note that absorption in the window layer structure does not significantly contribute to the photocurrent. Interband absorption can be minimized by using window layer materials with wide bandgaps ($E_g > 3$ eV) or otherwise weakly absorbing materials (e.g. with in-direct bandgaps). As mentioned, CdS has a bandgap energy of around 2.4 eV, which leads to absorption of light for wavelengths below 520 nm. This can be seen in Figure 6.1, which shows the EQE for three examples of window layer structures: (i) CBD CdS + sputtered (sp.) i-ZnO/ZnO:Al, (ii) ALD $ZnO_{1-x}S_x$ + sp. i-ZnO/ZnO:Al, and (iii) ALD $ZnO_{1-x}S_x$ + CVD ZnO:B. The wavelengths that correspond to the bandgap energies for ZnO ($E_g = 3.3$–3.4 eV) and CdS are indicated in the figure. When CdS is replaced with $ZnO_{1-x}S_x$, the interband absorption is reduced and EQE is increased for wavelengths up to about 520 nm. If the sputtered i-ZnO/ZnO:Al bi-layer is exchanged for CVD ZnO:B, the EQE can be improved further. However, this is partly due to an anti-reflective effect from the ZnO:B topography, rather than a reduction of the parasitic absorption.
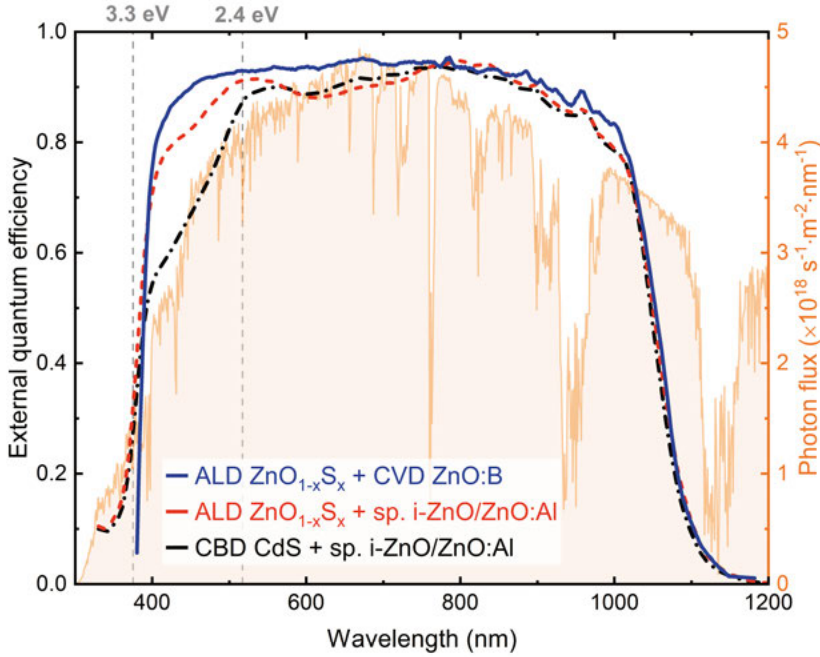
Figure 6.1. Examples of EQE for three different window-layer structures (on similar absorbers) with different optical properties. The photon flux for the AM1.5G standard spectrum [16] is included to indicate the potential gain from improving EQE at different wavelengths.

Free-carrier absorption occurs for long wavelengths in semiconductors with a high charge carrier concentration, i.e. in the TCO. Unlike interband absorption, the light is in this case absorbed by electrons in the conduction band that are able to move relatively freely within the band. A simple model to explain this is the classical Drude model [90]. In this model, the absorption coefficient increases with charge carrier concentration and is strongest around the so-called plasma frequency (ω_p). Furthermore, ω_p is also shifted to higher frequencies for higher charge carrier concentrations. Consequently, there is a compromise between transparency and lateral conductivity. However, by using TCOs with high electron mobility, it is possible to reduce free-carrier absorption without affecting the lateral conductivity.

6.2 Controlling the conduction band offset

One of the most influential window layer parameters to control is the conduction band offset (CBO) between the absorber and buffer layer. Theoretical analyses suggest that the optimal offset is in the range 0–0.4 eV [91,92], i.e. equal or slightly higher E_{CBM} in the buffer layer compared to the absorber at the interface. A positive and negative CBO is called a spike-like

51

and cliff-like offset, respectively. A spike in the conduction band will form a barrier that obstructs charge carrier transport across the junction. For small spikes, the photocurrent can be transported over the barrier by thermionic emission (or by tunneling for strong fields). However, if the CBO is too large, the photocurrent will be blocked (partially or fully). This is illustrated in Figures 6.2a and 6.2c, which show the energy band diagram of the front contact and corresponding influence on the J–V characteristics, respectively, when E_{CBM} in the buffer layer is increased. In this example, an S-shaped J–V curve will typically appear for too large CBO values, due to partially blocking of both the photocurrent and the forward current. On the other hand, the interface recombination rate typically increases if a cliff-like junction is formed, which significantly decreases V_{oc}. This is illustrated in Figures 6.2b and 6.2d. This is explained by recombination between holes in the absorber and electrons in the buffer layer, which can be neglected for spike-like junctions [91].

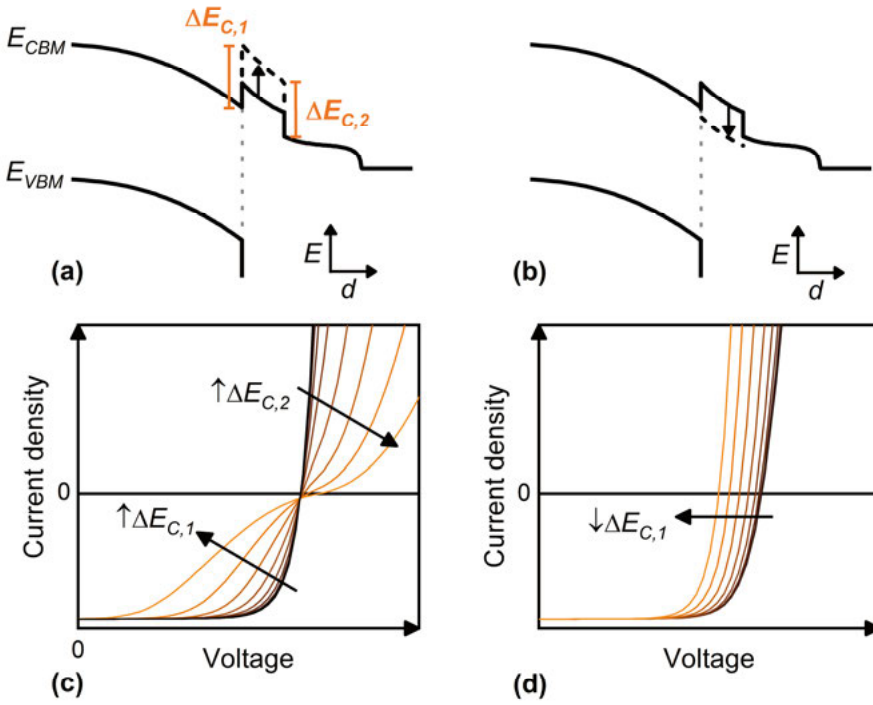**Figure 6.2**. Schematic energy band diagrams at the front contact for (a) increased and (b) decreased E_{CBM} in the buffer layer. The gray dotted line represents the absorber/buffer interface. The corresponding influence on the J–V characteristics is shown in (c) and (d). The notations $\Delta E_{C,1}$ and $\Delta E_{C,2}$ correspond to the CBO at the back and front interface of the buffer layer, respectively.

6.2.1 What determines the conduction band alignment?

In the simplest scenario, the conduction band alignment between two semiconductors is determined by their electron affinities. This is described by Anderson's model (also called the electron affinity rule) [93]:

$$\Delta E_C = \chi_A - \chi_B \tag{6.1}$$

where A and B are different semiconductors. However, Anderson's model only provides a rough estimation of the CBO. For most semiconductors, charge transfer across the interface must also be considered. Anderson's model can be modified to account for this [94]:

$$\Delta E_C = \left(\chi_A - \Phi_{CNL,A}\right) - \left(\chi_B - \Phi_{CNL,B}\right) + S(\Phi_{CNL,A} + \Phi_{CNL,B}) \tag{6.2}$$

where Φ_{CNL} is the so-called charge neutrality level for respective semiconductor [95], and S is a screening factor that is calculated for the semiconductor with widest bandgap. Generally, $S \approx 1$ if the density of interface states in the bandgap is low, which reduces Eq. 6.2 into Anderson's model, and $S \approx 0$ if the density of interface states is high, which results in the conduction band alignment being completely determined by the charge neutrality levels [96]. This is sometimes referred to as Fermi level pinning. Calculated values for S are around 0.3–0.6 for many oxides and sulfides (e.g. for ZnO, SnO_2, In_2O_3, Ga_2O_3, ZnS and CdS) [94], which means that the conduction band alignment to CIGS for these compounds is not solely determined by the electron affinities, even for ideal interfaces free from crystallographic defects. In general, the CBO can also be influenced by several other factors, such as interface polarity, crystallographic lattice matching and various chemical interactions that cause interface dipoles. However, this has not shown to dominate the band alignment for CIGS absorbers, and experimentally determined band alignments between CIGS and some of the most common buffer layer materials have been found to be in well agreement with theoretical predictions [97].

In a practical perspective, when working with materials with tunable electron affinities, a noteworthy implication of the band alignment theory is that the CBO can be manipulated by controlling the electron affinity as long as $S \neq 0$.

6.2.2 Improving the band alignment in wide-bandgap CIGS solar cells

The quality of CIGS solar cells with CdS buffer layers has shown to decrease when the gallium content near the front surface increases. The main issue is that V_{oc} does not scale with the absorber bandgap as expected, but instead saturates for absorber bandgaps above roughly 1.3 eV [64,98]. This is explained by the cliff-like CIGS/CdS junction that forms when the electron affinity of CIGS decreases [98]. By applying ALD $Zn_{1-x}Sn_xO_y$ buffer layers, the electron affinity and thus absorber/buffer CBO can be controlled by both the composition and deposition temperatures [84,99,100], and a suitable CBO can be achieved for the entire *GGI* range. This was shown in Paper II by depositing $Zn_{1-x}Sn_xO_y$ buffer layers at different deposition temperatures on non-graded CIGS absorbers with varying *GGI* between 0.3 and 1. At low deposition temperatures, where the lowest electron affinity is expected, the V_{oc} deficit was considerably reduced for high gallium contents compared to the CdS references, as shown in Figure 6.3. Unlike for the CdS reference solar cells, V_{oc} did not seem to saturate when $Zn_{1-x}Sn_xO_y$ was used, which indicates a significant reduction in interface recombination due to an improved CBO and/or a decreased interface defect density. Even so, the V_{oc} deficit increased when increasing the *GGI* regardless of buffer layer.

The potential of improving the CBO at the absorber/buffer interface was further investigated in Paper II for improved $CuGaSe_2$ absorbers that were co-evaporated in a high-temperature three-stage type process ($T_{substrate} \approx 650$ °C).
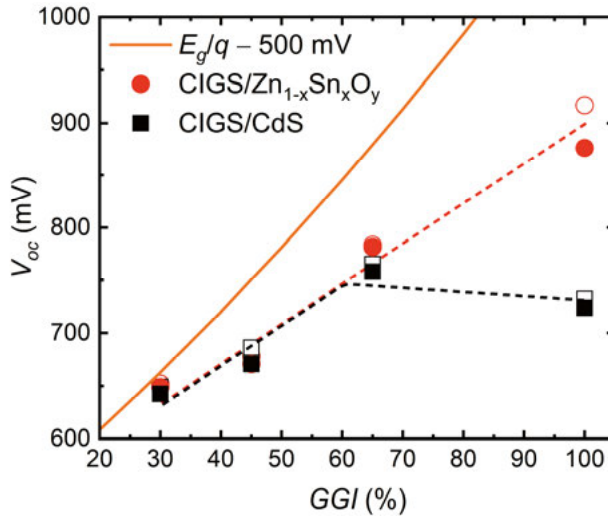

Figure 6.3. Median (filled symbols) and best (open symbols) V_{oc} values attained for CIGS absorbers with varying gallium content for two different buffer layers, CBD CdS and ALD $Zn_{1-x}Sn_xO_y$ ($x = 0.17 \pm 0.03$, $T_{ALD} = 95$ °C). The solid line indicates $E_g/q - 500$ mV and the dashed lines are guides for the eye. Data from Paper II.

Table 6.1. J–V parameters for the best solar cells achieved when using three-stage type co-evaporated CuGaSe$_2$ absorbers in Paper II for different buffer layers. Absorber bandgaps extracted from IQE measurements are also included. From Paper II.

Sample	$E_{g,QE}$ (eV)	V_{oc} (mV)	FF (%)	J_{sc} (mA/cm^2)	η (%)
CuGaSe$_2$/ZTO (T_{ALD} = 95 °C)	1.60	1007	56.4	16.0	9.10
CuGaSe$_2$/ZTO (T_{ALD} = 120 °C)	1.62	1003	67.1	15.8	10.7
with ARC:		1017	67.0	17.5	11.9
CuGaSe$_2$/CdS	1.62	768	58.6	15.2	6.82

First, solar cells were fabricated with Zn$_{1-x}$Sn$_x$O$_y$ buffer layers deposited at 95 °C with a cation ratio of $x = 0.24 \pm 0.03$. These solar cells exhibited a blocking J–V behavior that resulted in poor FF values. The best cell had a FF of 56.4%, as listed in Table 6.1 where the measured J–V parameters are reported for the best CuGaSe$_2$ solar cells achieved with different buffer layers. However, the V_{oc} of this device (1007 mV) was significantly higher than for the best CdS reference (786 mV).

The activation energy of the dominating recombination path in these solar cells was extracted from illuminated and dark J–V(T) measurements, as shown in Figure 6.4. For the solar cell with a Zn$_{1-x}$Sn$_x$O$_y$ buffer layer, activation energy values of 1.64 eV and 1.62 eV were extracted from the illuminated and dark J–V(T) measurements, respectively, which roughly corresponds to the expected fundamental bandgap of CuGaSe$_2$. The common interpretation is that this indicates a reduced interface recombination rate. However, this does not entirely exclude the possibility of a dominating recombination at the interface. In contrast, the activation energy values for the CdS reference sample were about 0.7–1.0 eV, which is consistent with recombination at the interface.

It was assumed that the blocking J–V behavior was caused by a too large CBO. Therefore, additional solar cells were fabricated where the temperature during ALD of Zn$_{1-x}$Sn$_x$O$_y$ was increased to 120 °C, while maintaining a cation ratio of $x = 0.24 \pm 0.03$. This resulted in a champion cell with an efficiency of 11.9% and V_{oc} of 1017 mV, after applying an anti-reflective coating. At the time Paper II was published, this was the highest reported efficiency for a CuGaSe$_2$ solar cell and the highest V_{oc} achieved for any chalcopyrite solar cell. The measured J–V and IQE curves for the champion cell and the best CdS reference are displayed in Figure 6.5. It can be observed that no blocking behavior can be discerned from the J–V characteristics. However, the FF seems to be limited by a voltage-dependent current collection. In addition, IQE is lower than 0.9 over the entire spectrum, which is presumably caused by collection losses in the absorber. Substantial improvements in device efficiency are therefore expected by improving the CuGaSe$_2$ bulk quality.
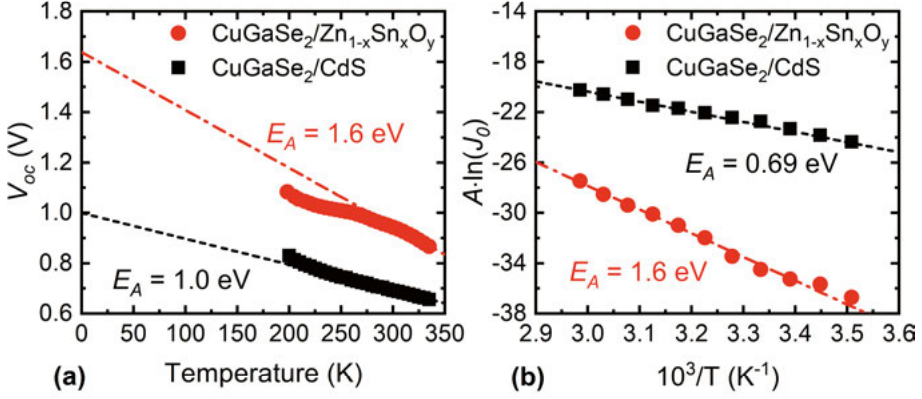
Figure 6.4. (a) $V_{oc}(T)$ from illuminated J–V(T) measurements for CuGaSe$_2$ devices with CdS and Zn$_{1-x}$Sn$_x$O$_y$ buffer layers ($x = 0.24 \pm 0.03$, $T_{ALD} = 95$ °C). (b) Recombination activation energies extracted from dark J–V(T) measurements. Reworked from Paper II.

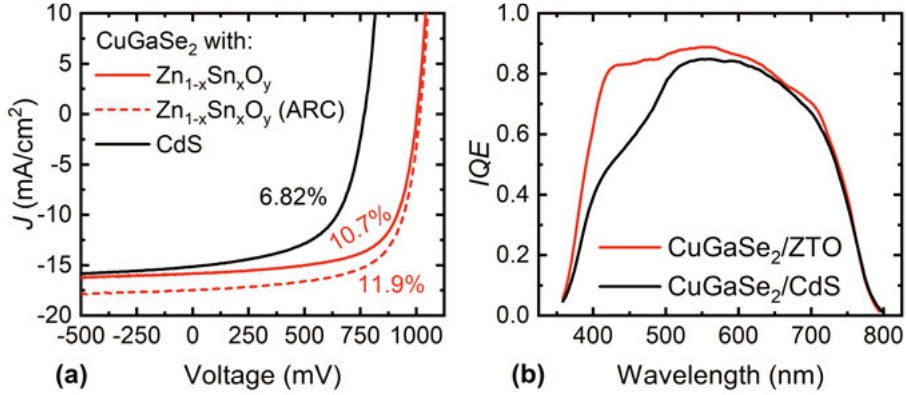**Figure 6.5**. (a) J–V characteristics for the best CuGaSe$_2$ device with Zn$_{1-x}$Sn$_x$O$_y$ buffer layer ($x = 0.24 \pm 0.03$, $T_{ALD} = 120$ °C) and the best CdS device from the same study. The characteristic after anti-reflection coating is shown for Zn$_{1-x}$Sn$_x$O$_y$. (b) IQE of the devices without anti-reflective coatings. Reworked from Paper II.

56

Another potential issue with the CuGaSe$_2$ solar cells that were fabricated in this study is that they all showed various metastable behavior regardless of buffer layer, e.g. it could take a few days or even weeks for the J–V parameters to stabilize (mainly due to variations in *FF*). However, the short-term and long-term stability was not systematically studied.

6.3 Doping profile in the window layers

The doping profile in the absorber and window layer structure (charge carrier concentration and layer thickness) is one of the main factors that determine the potential distribution in the solar cell, i.e. the built-in potential and band bending. An asymmetric doping is typically employed, where the n-side of the device is higher doped than the p-side, so the majority of the band bending takes place in the absorber layer, leading to a wide depletion region. In addition, this also results in a so-called type inversion of the absorber surface region, for a suitable absorber/buffer CBO. The type inversion can be observed in calculated energy band diagrams from the region where the Fermi level in the absorber is closer to the conduction band than the valence band. This is beneficial since the Fermi level is shifted away from the mid-gap energy at the CIGS/buffer interface, where the highest defect concentration is expected, which reduces the interface recombination rate. An alternative, but equivalent explanation, is that the p–n junction shifts into the CIGS bulk and thus results in a buried homo-junction. An example is provided in Figure 6.6, where energy band diagrams calculated in Paper I for a CIGS/CdS/i-ZnO/TCO structure with different i-ZnO thicknesses (20 nm and 160 nm) and i-ZnO doping concentrations (10^{17} cm^{-3} and 10^{14} cm^{-3}) are displayed. This demonstrates a weaker type inversion of the CIGS surface when the depletion width is extended further into the window layers. Note that the CdS layer is in this case assumed to be completely depleted, which occurs for low-doped buffer layers. Interestingly, the reduced type inversion for lower doped i-ZnO layers implies that too resistive intrinsic layers can be detrimental for solar cell performance, even though it is beneficial for shunt prevention. A more detailed discussion of the competing roles of i-ZnO can be found in ref. [101].
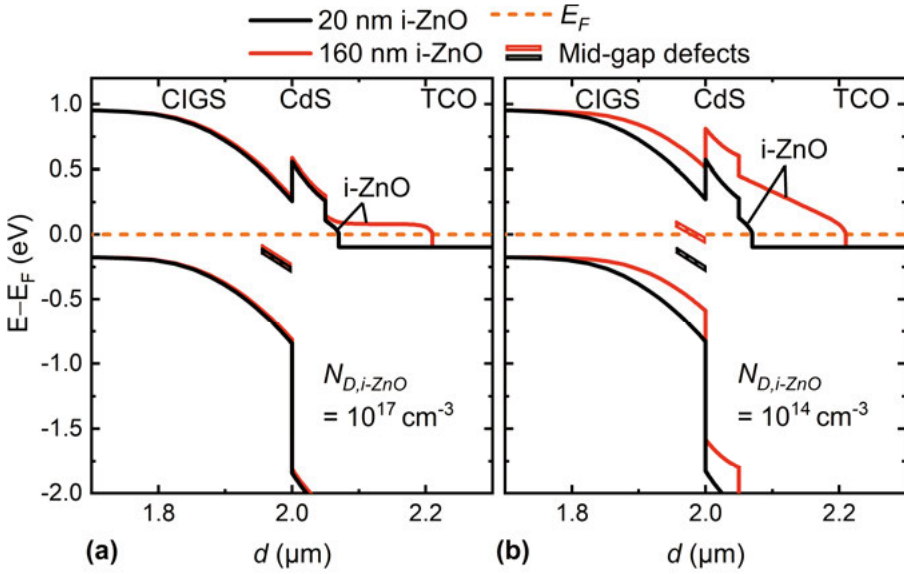
Figure 6.6. Calculated energy band diagrams for a CIGS/CdS/i-ZnO/TCO structure for a thin (20 nm) and thick (160 nm) i-ZnO layer with a charge carrier concentration (a) $N_D = 10^{17}$ cm^{-3} and (b) $N_D = 10^{14}$ cm^{-3}. CdS is here fully depleted ($d = 50$ nm, $N_D = 4.5 \cdot 10^{16}$ cm^{-3}). Reworked from Paper I.

6.4 Absorber surface passivation

Defect states at the absorber/buffer interface can have different origins, including a crystallographic lattice mismatch that results in so-called dangling bonds, chemical bonding/interactions, impurities, and structural damage from buffer layer processing. Regardless of the origin, it is important to minimize the defect density at the absorber/buffer interface in order to reduce the recombination rate. Other than finding a suitable buffer layer process, it is possible to reduce the defect density by various absorber surface treatments (e.g. PDT with alkali-metal fluorides) or by adding a passivating layer between the absorber and buffer layer. While rear contact passivation has been more extensively studied for application in solar cells with very thin absorber layers [102], three-dimensional numerical simulations of the effect from insulating passivating layers (with point contact openings) suggest that front contact passivation layers can substantially reduce the recombination rate [103]. The potential passivation effect is partly due to a reduction of the defect density (i.e. chemical passivation), but also due to positive fixed oxide charges that can enhance the absorber surface type inversion and repel holes from the interface at sufficiently high fixed positive charge densities (i.e. field effect passivation). Experimentally, several oxides have been found able to reduce

the CIGS interface defect density, e.g. Al_2O_3, Ga_2O_3, HfO_2 and SiO_2 [104–107]. The success in improving the solar cell efficiency with such passivation layers has been limited this far, but will potentially be a valuable part of future window layer structures.

6.5 Impact of alkali-metal fluoride PDT on ALD processing

Modification of CIGS surfaces by alkali-metal fluoride PDT typically results in residuals salts on the surface, as summarized in Section 3.5. This can directly influence the processing of ALD buffer layers and be detrimental to the solar cell performance. The possibility to combine ALD $ZnO_{1-x}S_x$ buffer layers with KF-PDT was investigated in Paper III. Blocking J–V characteristics were observed when $ZnO_{1-x}S_x$ buffer layers were applied to as-deposited CIGS-KF absorbers, which resulted in low *FF* values. The blocking behavior for the as-deposited CIGS-KF absorber likely originates from the residual salts at the CIGS/$ZnO_{1-x}S_x$ interface. A possible explanation is that the salts on the surface either form a fully or partially blocking layer, or that the KF-modified surface has a detrimental effect on the initial ALD growth of $ZnO_{1-x}S_x$. Either way, this could only be avoided by performing an additional wet-chemical treatment. This is shown in Figure 6.7 where typical J–V characteristics are shown for as-deposited, water rinsed and HCl etched CIGS-KF. In addition, schematic pictures are included that show the surface phases that were present on the surface in each case, according to XPS characterization in Paper III. A water rinse was sufficient to dissolve the salts from the surface and led to formation of a surface that was qualitatively similar to the one formed during a conventional CdS CBD process, i.e. copper- and gallium-depleted, with a $KInSe_2$ phase at the surface. The modified surface layer could be etched away by diluted hydrochloric acid.

Solar cells fabricated with water-rinsed absorbers and ALD $ZnO_{1-x}S_x$ buffer layers did not exhibit the blocking behavior observed for as-deposited absorbers. However, the efficiencies were still lower than for the CdS references, primarily due to lower *FF* values.
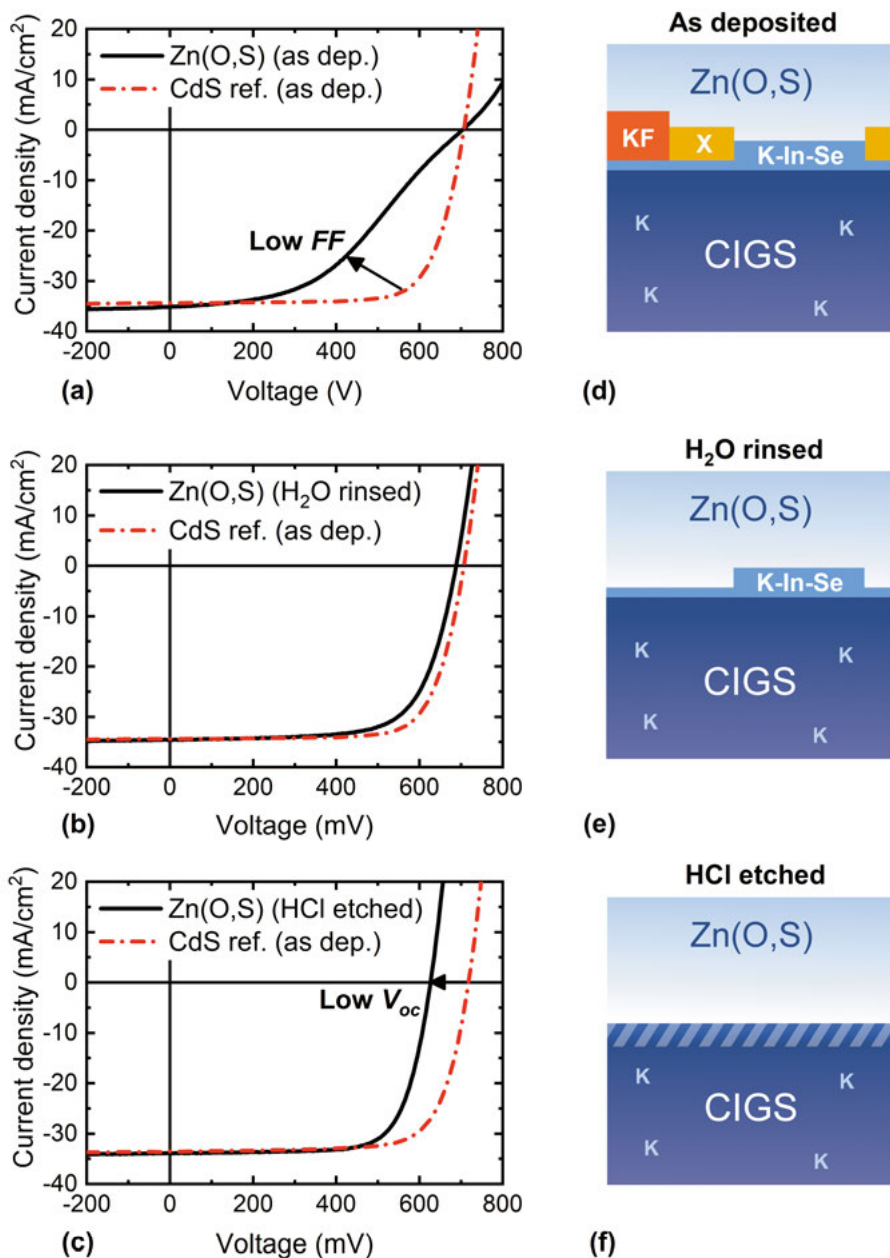
Figure 6.7. Typical J–V characteristics for solar cells with ALD $ZnO_{1-x}S_x$ buffer layers and (a) as-deposited, (b) water rinsed, and (c) HCl etched (2 M) CIGS-KF absorbers. CdS references are included that were fabricated with as-deposited absorbers. The schematic pictures in (d)–(f) show the expected surface phases for each treatment, according to XPS analysis. The phase denoted "X" represents a water-soluble gallium- and fluorine-containing compound. The dashed area in (f) indicates a CIGS surface that is possibly modified by the HCl etching. Reworked from Paper III.

The difference in average *FF* between $ZnO_{1-x}S_x$ devices and CdS references seemed to increase for an increased KF flux during the PDT process. This can be seen in Figure 6.8 where J–V parameters are plotted as a function of incoming KF flux during PDT. The solar cells where in this case fabricated with absorbers cut from a module-sized (60×120 cm^2) substrate, processed with a lateral gradient in KF flux during PDT. The lowest flux corresponded to no or little KF, while the highest flux provided more KF than optimal with regard to solar cell efficiency. For solar cells where no or little KF was applied, the average *FF* was around 69% for both buffer layers. When the KF flux increased, the average *FF* increased to a maximum of 72% for solar cells with CdS buffer layers while *FF* was rather constant for solar cells with $ZnO_{1-x}S_x$, despite a substantial improvement in V_{oc} (which would typically also result in improved *FF*). A possible explanation to the lower *FF* values for the $ZnO_{1-x}S_x$ devices can be that the PDT-modified surface affected the initial ALD growth, e.g. by modifying the nucleation in a way that resulted in a more sulfur-rich interface. Although this could not be confirmed in Paper III, a deviation from bulk composition during the initial ALD growth of ternary compounds can occur in general, which is demonstrated and discussed in Section 7.3.
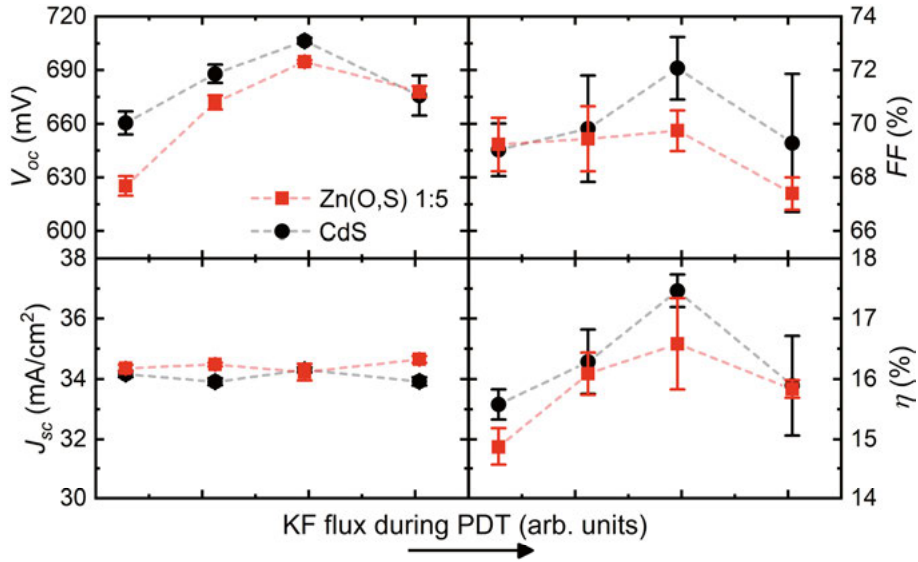
Figure 6.8. Average V_{oc}, *FF*, J_{sc}, and η for solar cells fabricated with ALD $ZnO_{1-x}S_x$ and CBD CdS buffer layers and absorbers cut from a module-sized substrate processed with a lateral gradient in KF flux during PDT. The lowest flux corresponds to no or little KF, while the highest flux results in more KF than optimal. The absorbers were water rinsed prior to $ZnO_{1-x}S_x$ deposition. Error bars show the within-sample standard deviation. Reworked from Paper III.

In either way, the *FF* could be partly improved by tuning the $H_2S:H_2O$ pulse ratio during the initial buffer layer growth. A series of solar cells was fabricated where the $H_2S:H_2O$ pulse ratio was varied between 1:4 and 1:8 during the first 25 ALD sub-cycles, followed by 150 sub-cycles with a 1:5 pulse ratio. The resulting J–V parameters are displayed in Figure 6.9. When the pulse ratio changed from 1:5 to 1:7, the average *FF* value increased from 65% to 69%. The difference was merely one H_2S pulse less during the first 3–5 nm of growth. This very high sensitivity to H_2S is possibly related to the exchange reactions discussed previously in Section 5.2.3.

Some additional interesting observations from the V_{oc} and efficiency trends in Figure 6.8 are that the optimal KF amount during PDT was found to be the same for both buffer layer processes, and that the V_{oc} improvement by KF-PDT was of comparable magnitudes. This indicates that the main effect from KF-PDT is independent of the buffer layer process.

In Paper III, the best efficiency achieved for solar cells fabricated with water rinsed CIGS-KF absorbers and ALD $ZnO_{1-x}S_x$ buffer layers was 16.8% (V_{oc} = 690 mV, *FF* = 69.5%, J_{sc} = 35.1 mA/cm^2), which can be compared to 17.7% for the CdS reference (V_{oc} = 711 mV, *FF* = 72.3%, J_{sc} = 34.5 mA/cm^2). However, by etching the absorbers in diluted hydrochloric acid prior to ALD growth, the apparent incompatibility of the KF-modified surface and the ALD process could be avoided. The *FF* values for solar cells with etched absorbers

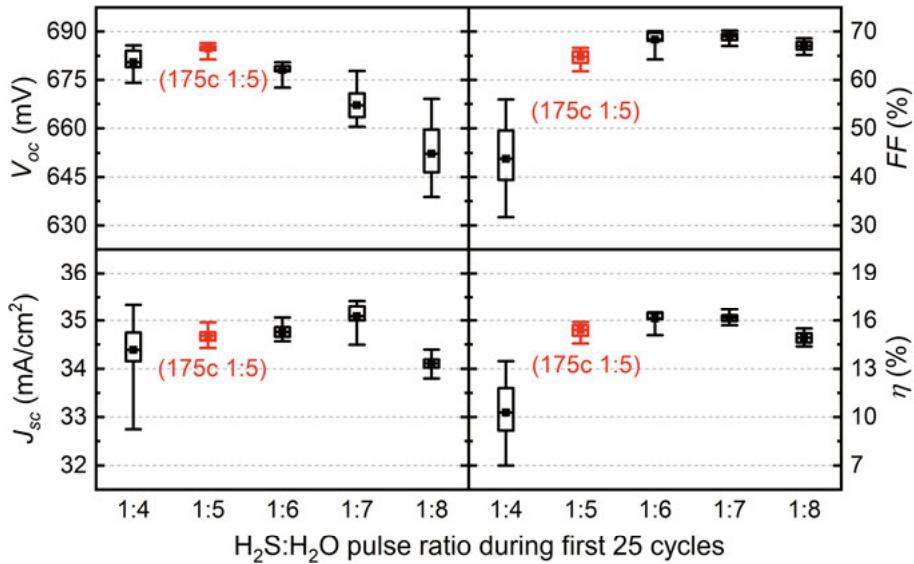**Figure 6.9**. Average V_{oc}, *FF*, J_{sc}, and η for solar cells with water-rinsed CIGS-KF absorbers and $ZnO_{1-x}S_x$ buffer layers grown in an ALD process where the $H_2S:H_2O$ pulse ratio was varied during the first 25 ALD sub-cycles, followed by 150 sub-cycles with a 1:5 pulse ratio. The red data corresponds to a single-step 1:5 process. Reworked from Paper III.

and $ZnO_{1-x}S_x$ buffer layers were almost as good as for the CdS reference. See Table 6.2 for measured J–V parameters. However, the etching step initially resulted in significantly reduced V_{oc} values and thus low efficiency values. Interestingly, the V_{oc} could be restored by heat treating the finalized devices at 165–180 °C for 30–60 min in 2 Torr N_2. The best CIGS-KF/$ZnO_{1-x}S_x$ device that was fabricated with this "etch-and-anneal" approach initially showed an efficiency of 15.5%, which was improved to 18.0% after a 30 min heat treatment at 165 °C (also in 2 Torr N_2). This efficiency was comparable to the efficiencies of the CdS references listed in Table 6.2.

The results from Paper III demonstrated that an efficiency gain by KF-PDT is possible when employing ALD buffer layers. However, the addition of wet-chemical process steps is less attractive for production. Other vacuum-based buffer layer processes might not require the etching step, while the residual salts must likely be either limited or removed entirely from the surface prior to buffer layer deposition.

Moreover, an interesting alternative to alkali-metal fluoride PDT is to employ a fluorine-free alkali-metal PDT, or even add the alkali metals directly during absorber layer deposition. A preliminary study has shown similar effects from pure K- and Rb-PDT compared to the fluoride equivalents [69]. The fluorine-free PDT processes might show to be more compatible with vacuum-based processing.

Table 6.2. Average (and best) J–V parameters for solar cells fabricated with CIGS-KF absorbers etched in 2 M HCl, before and after a post-fabrication heat treatment performed in 2 Torr N_2. CdS reference devices with as-deposited absorbers are included for a detailed comparison. From Paper III.

Buffer layer	Heat treatment	Pre-ALD treatment	η (%)	V_{oc} (mV)	FF (%)	J_{sc} (mA/cm^2)
$ZnO_{1-x}S_x$	None	HCl	15.1 (15.5)	619 (626)	72.5 (73.2)	33.7 (34.3)
$ZnO_{1-x}S_x$	165 °C 30 min	HCl	17.7 (18.0)	692 (696)	73.8 (74.1)	34.6 (34.9)
$ZnO_{1-x}S_x$	180 °C 60 min	HCl	17.5 (17.9)	689 (692)	74.1 (74.5)	34.3 (34.9)
CdS	None	HCl	16.6 (16.8)	692 (695)	73.0 (73.6)	32.9 (33.3)
CdS	180 °C 60 min	HCl	17.3 (17.6)	696 (699)	74.5 (74.9)	33.4 (33.7)
CdS	None	None	17.3 (17.8)	715 (718)	73.3 (74.1)	33.1 (33.6)
CdS	180 °C 60 min	None	17.8 (18.3)	707 (713)	74.3 (75.5)	33.9 (34.3)

6.6 Note on combining different window layer processes

A challenge when developing improved window layer structures is the intricate relationship between the different layers and corresponding deposition processes. When a window layer process is exchanged or modified, it can also affect the functionality of other layers. Some effects can be predicted from the layer's bulk properties, e.g. expected change in the energy band structure of the device. Examples of other effects that can be more challenging to predict (and quantify) are the electronic properties of the different interfaces and effects from subsequent processing steps on the properties of previously deposited layers, e.g. due to sputter-induced damage or thermal stress [108,109].

An example of this was early experienced in this thesis work when modifying the i-ZnO and TCO processes simultaneously in CIGS solar cells with conventional CdS buffer layers. In Paper I, the baseline sputtered i-ZnO layer (ρ = 0.6 $\Omega\cdot$cm) was replaced with CVD-grown i-ZnO that was considerably more resistive (ρ > 500 $\Omega\cdot$cm, T_{CVD} = 95 °C) and had previously shown to exhibit a slightly wider optical bandgap [110]. Meanwhile, the baseline sputtered ZnO:Al TCO was replaced with ALD-grown In_2O_3:H (IOH, T_{ALD} = 145 °C), which in general exhibits a higher electron mobility and thus allows for reduced free-carrier absorption [111]. It was found that the i-ZnO thickness can have a strong effect on V_{oc}, depending on the combination of processes. This can be seen in Figure 6.10, which shows that the best obtained V_{oc} values significantly decreased with increased CVD i-ZnO thickness when ALD In_2O_3:H was used as TCO, while the decrease was not as pronounced for sputtered ZnO:Al TCOs. Similar reductions in V_{oc} could not be reproduced for sputtered i-ZnO layers (more data are available in Paper I). A possible explanation for the observed V_{oc} variations is that the depletion layer width extends further into the front contact as the thickness of the intrinsic layer is increased, in case of a low-doped i-ZnO layer (i.e. CVD i-ZnO). This reduces the type inversion of the CIGS surface, resulting in an increased (near-)interface recombination rate as the Fermi level shifts closer to the mid-gap energy (see Section 6.3). In case of the sputtered i-ZnO layer, the higher charge carrier concentration (estimated to be in the order of 10^{18} cm^{-3}) likely limits how far the depletion region can extend into the intrinsic layer and thus determines the band bending rather than the layer thickness. If this mechanism explains all observed V_{oc} variation, then it would seem like the carrier concentration in the i-ZnO layer is increased after ZnO:Al sputtering, which has been previously proposed [112]. However, it is not possible to exclude an effect from interfaces or different TCO electron affinities.
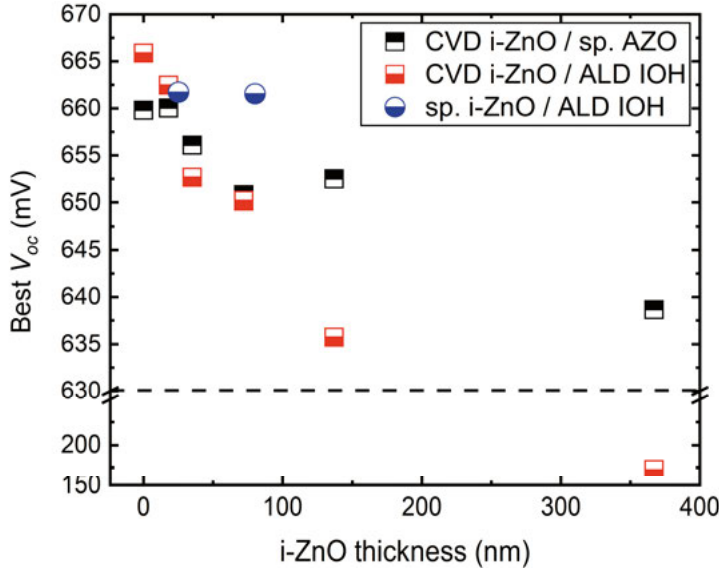
Figure 6.10. Best obtained V_{oc} values for different i-ZnO thicknesses in solar cells fabricated with different combinations of i-ZnO and TCO processes. Reworked from Paper I.

Furthermore, the window layer structure can also influence light-induced metastability effects that are commonly observed in CIGS solar cells [21,84,113,114]. One important contribution to the metastability is photoconductivity in the buffer layer, which can influence the effective barrier height for the photocurrent [115,116]. However, it should be noted that this also depends on the other layers in the window layer structure, as demonstrated by $ZnO_{1-x}S_x$ buffer layers, which show different metastable effects depending on the intrinsic layer material and deposition conditions [114].

In addition, chemical reactions at interfaces and interdiffusion between layers in the solar cell are known to contribute to the deterioration of the long-term stability of a solar cell, and they strongly depend on the combination of material layers [117]. In conclusion, it is not possible to optimize each layer of the solar cell individually (including the solar cell absorber).

7 Development of amorphous tin gallium oxide as a new buffer layer

Ternary compound buffer layers have shown to be very promising for wide-bandgap absorbers, not only for $CuGaSe_2$ (Section 6.2.2) but also for non-chalcopyrite structured absorbers such as Cu_2ZnSnS_4 (CZTS) [118–120]. However, all established ternary buffer layers are modifications of ZnO, which can form a rather poor-quality interface to CIGS when deposited by low-temperature ALD [121]. Moreover, ALD grown $ZnO_{1-x}S_x$ and $Zn_{1-x}Mg_xO_y$ have shown to suffer from phase separation for high values of x [85,122], limiting their use for wide-bandgap absorbers. This motivated the search for a new buffer layer candidate that should (i) exhibit a highly variable electron affinity that can be suitable for wide-bandgap absorbers, (ii) form similar or better interface quality than obtained with CdS, and (iii) consist of a single phase over the entire composition range, while allowing for an industrially feasible and non-hazardous production.

An interesting class of materials for this purpose is the transparent semiconducting amorphous oxides [123]. These are oxides formed from post-transition metal cations that possess a $(n-1)d^{10}ns^0$ electron configuration, where n is the principal quantum number, see Figure 7.1 [124]. The bottom

Figure 7.1. Reduced view of the periodic table with highlighted elements that can form cations with $(n-1)d^{10}ns^0$ electron configurations. Adapted from ref. [124]. Green triangles indicate elements that might be interesting for ternary oxide buffer layers.

part of the CBM in these oxides mainly consists of the cations' ns orbitals. The spherical symmetry and spatial size of these orbitals allow for the fabrication of disordered materials with moderately high electron mobility values of above 10 $cm^2/(V·s)$. Furthermore, by forming multicomponent oxides with these cations, it is possible to tailor the electron affinity by controlling the ratio of the binary oxide components [125]. The range of expected band alignments is thus, in theory, defined by the binary oxides. See Figure 7.2 for band alignments between $CuInSe_2$ (and $CuGaSe_2$) and various binary semiconducting oxides, calculated according to Eq. 6.2. CdS is included for comparison. These calculated values for ideal interfaces should only be regarded as a rough estimation of the band alignments that can be expected. All the same, they indicate that suitable band alignments can likely be obtained by combining e.g. ZnO, In_2O_3 or SnO_2 (which show small or negative CBO values with $CuInSe_2$) with Ga_2O_3 or GeO_2 (which show large CBO values). Out of these combinations, sputtered $a\text{-}In_{1-x}Ga_xO_y$ has previously been evaluated as a buffer layer in CIGS solar cells [126].

$Sn_{1-x}Ga_xO_y$ grown by ALD was chosen to be evaluated as a new buffer layer material. In addition to a wide predicted range of possible CBO values, a good interface to CIGS with a low defect density is expected. Ga_2O_3 has been suggested to form a beneficial interface to CIGS with a low defect density [104], and it has been indicated that SnO_2 forms interfaces to CIGS of better quality than ZnO [121]. Furthermore, the amorphous structure of $Sn_{1-x}Ga_xO_y$
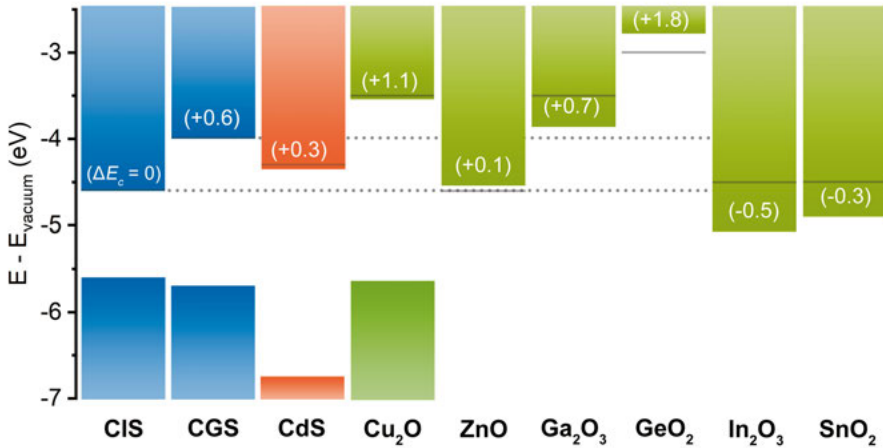

Figure 7.2. Intrinsic band alignments according to Eq. 6.2 with data (χ, E_g, Φ_{CNL}, S) from refs. [94] and [127]. The solid gray lines correspond to the electron affinity values. Note that the valence band edges for ZnO, Ga_2O_3, GeO_2 In_2O_3 and SnO_2 are out of scale.

reduces the risk of secondary phase formation and possibly eliminates any concerns about lattice matching with the crystallographic surface planes of CIGS.

7.1 ALD of a-$Sn_{1-x}Ga_xO_y$

A ternary ALD process to deposit a-$Sn_{1-x}Ga_xO_y$ was developed in Paper IV by combining existing low-temperature processes for a-SnO_2 and a-Ga_2O_3, respectively [128,129]. The films were grown in an F-120 laminar flow reactor (ASM Microchemistry) equipped with a QCM sensor head, at substrate temperatures between 105 and 195 °C. The metal precursors were DMA_4Sn and DMA_3Ga (dimer). Deionized water was used as co-reactant. Highly purified N_2 was used as transport and purge gas. The film composition was controlled by the sub-cycle ratio in a super-cycle approach, with the pulse scheme $(DMA_4Sn:N_2:H_2O:N_2)_A$:$(DMA_3Ga:N_2:H_2O:N_2)_B$, where $B/(A+B)$ or $A:B$ is the sub-cycle ratio. A pulse time of 1 s was used for all pulses. See Paper IV for more details.

7.1.1 ALD growth characteristics

Figure 7.3 shows QCM recordings of typical film-on-film growth of SnO_2, Ga_2O_3 and a $Sn_{1-x}Ga_xO_y$ process with a 1:1 sub-cycle ratio, when employing the ALD process described above at 175 °C. The ALD growth during each sub-cycle in the mixed process is similar to the growth in the corresponding binary processes. See Table 7.1 for extracted values for mass gain per sub-cycle (Δm) and the ratio between the mass after the first half-reaction (m_1) and Δm. This indicates that the ALD growth of each sub-cycle is not significantly influenced by the mixing of sub-cycles, for depositions at 175 °C.

Table 7.1. Extracted growth parameters from QCM measurements. From Paper IV.

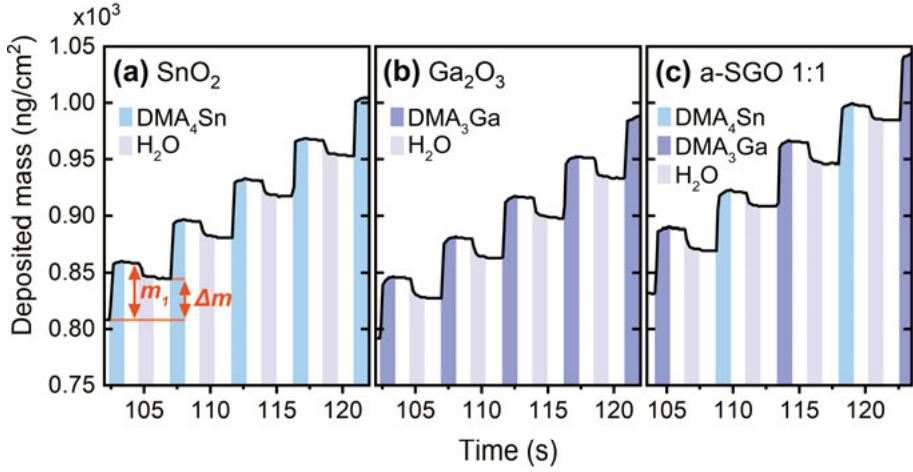| Process	Δm (ng/cm^2)	$m_1/\Delta m$
T_{ALD} = 175 °C		
SnO_2	36	1.4
Ga_2O_3	36	1.5
1:1 Sn-O sub-cycle	39	1.3
1:1 Ga-O sub-cycle	38	1.5
T_{ALD} = 105 °C		
SnO_2	55	1.2
Ga_2O_3	37	1.4
1:1 Sn-O sub-cycle	45	1.2
1:1 Ga-O sub-cycle	43	1.4

Figure 7.3. Deposited mass over time during ALD of (a) SnO_2, Ga_2O_3, and $Sn_{1-x}Ga_xO_y$ with a 1:1 sub-cycle ratio, measured by QCM at a deposition temperature of 175 °C. Reworked from Paper IV.

The *GPC* and average mass gain per super-cycle ($<\Delta m>$) for different sub-cycle ratios are shown in Figure 7.4a for depositions at 175 °C. It can be observed that the average mass gain is rather constant around 34–37 ng/cm^2 at this temperature, with only a slightly increased value for intermediate sub-cycle ratios. This results in an approximately linear *GPC* trend (due to differences in density) between 0.6 Å for pure SnO_2 and 0.8 Å for pure Ga_2O_3. Furthermore, $<\Delta m>$ for SnO_2, Ga_2O_3 and a mixed process with a 1:1 sub-cycle ratio is shown Figure 7.4b for varying deposition temperatures in the range 105–195 °C. The mass gain per cycle for Ga_2O_3 is relatively unaffected by the deposition temperature, whereas it decreases from around 55 ng/cm^2 at 105 °C to 31 g/cm^2 at 195 °C for SnO_2. The substantial variation in *GPC* for the SnO_2 process in this temperature range has been previously reported and discussed in the literature [130,131]. Furthermore, the average mass gain per super-cycle for the 1:1 process is in-between the corresponding values for the binary processes, except a slight deviation for T_{ALD} = 175 °C. However, the mass gain for the individual sub-cycles in the mixed process differs from the binary processes at other deposition temperatures than 175 °C, e.g. see values for T_{ALD} = 105 °C in Table 7.1. A proposed explanation to this observation is given in Paper IV, based on variations in number of reactive surface sites.
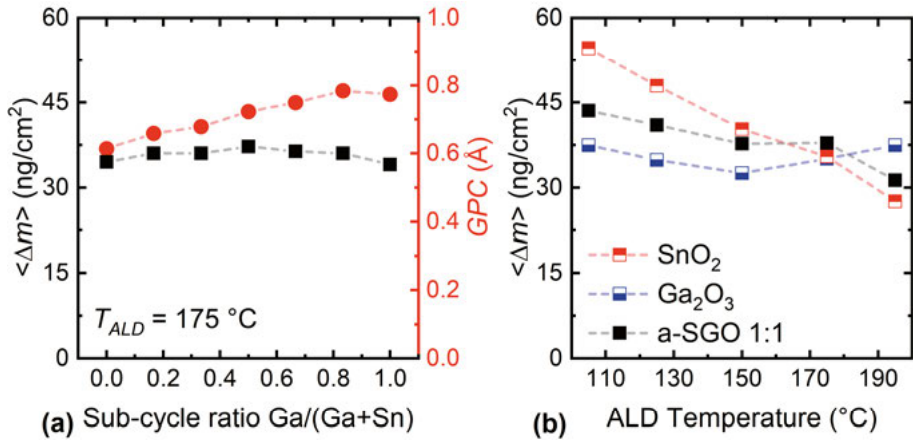
Figure 7.4. (a) Average mass gain per super-cycle (squares) and *GPC* (circles) versus sub-cycle ratio measured by QCM for ALD $Sn_{1-x}Ga_xO_y$ deposited at 175 °C. (b) Average mass gain per super-cycle versus deposition temperature for ALD of SnO_2, Ga_2O_3 and $Sn_{1-x}Ga_xO_y$ with a 1:1 sub-cycle ratio. Reworked from Paper IV.

7.1.2 Cation composition control

The independency of $<\Delta m>$ in respect of sub-cycle ratio for depositions performed at 175 °C makes it straightforward to predict and control the cation composition in the films. This is shown in Figure 7.5a, where the measured cation ratio is plotted versus sub-cycle ratio. The figure includes both data obtained with RBS-calibrated XRF measurements for 62–79 nm thick films grown on fused quartz substrates using 1000 ALD sub-cycles, as well as composition values calculated from QCM measurements. By extracting the mass gain per individual sub-cycle, it is possible to estimate the cation ratio according to Eq. 7.1:

$$x_{QCM} = \frac{n_{Ga}}{n_{Ga} + n_{Sn}} = \frac{1}{1 + 0.5\left(\frac{A}{B}\right)\left(\frac{M_{Ga_2O_3}}{M_{SnO_2}}\right)\left(\frac{\Delta m_{Sn-O}}{\Delta m_{Ga-O}}\right)} \qquad (7.1)$$

Furthermore, the expected cation composition based on a simple rule-of-mixtures (see Section 5.2.2) is also included in Figure 7.5a. It is shown that the experimental composition values accurately follow the rule-of-mixtures for depositions performed at 175 °C. This is a strong indication that the growth at this temperature is mainly free from non-ideal effects.

For other deposition temperatures, this may not hold true. In either way, it was found that the cation composition was constant for a 1:1 process in the investigated temperature range, as shown in Figure 7.5b. This is explained by the similar Δm values for each sub-cycle regardless of deposition temperature.
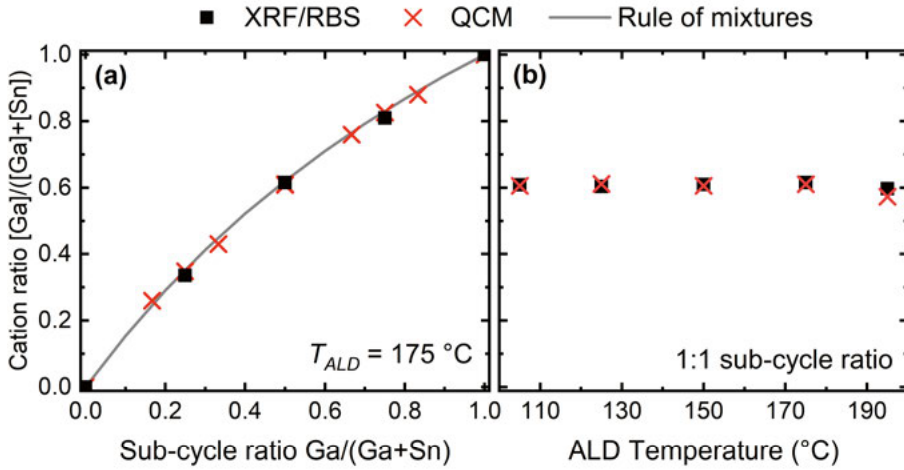
Figure 7.5. Cation composition in $Sn_{1-x}Ga_xO_y$ films (a) versus sub-cycle ratio for films grown at 175 °C, and (b) versus deposition temperature for films deposited with a 1:1 sub-cycle ratio. Reworked from Paper IV.

Furthermore, this shows that the ALD process is very robust in terms of controlling the cation composition in the films.

7.1.3 Optical properties

By controlling the cation ratio in the $Sn_{1-x}Ga_xO_y$ films, the optical bandgap can be varied in a wide range, as predicted. This is shown in Figures 7.6a and 7.6c, where optical bandgap values are plotted as a function of cation ratio and deposition temperature. The optical bandgap values were extracted from R–T measurements and corresponding Tauc plots for amorphous films (see Appendix A.2). Tauc plots for films deposited at 175 °C with varying composition are shown in Figure 7.6b, and Tauc plots for films with cation ratio $x = 0.6$ for varying deposition temperatures are shown in Figure 7.6d. The optical bandgap varies from around 2.7 eV for pure SnO_2 to above 4.2 eV for pure Ga_2O_3 for films deposited at 175 °C. A part of the bandgap variation is presumably due to the expected shift in electron affinity for a varied cation ratio (in contrast to a lowered valence band). Furthermore, quite strong absorption tails can be observed. It is possible that the tails originate from localized oxygen p-states above the valence band, which has been reported for other amorphous semiconducting oxides [132–134]. However, sub-gap states below the conduction band edge cannot be excluded.

It was also found that the deposition temperature has a significant influence on the optical bandgap. For instance, the optical bandgap varies from 4.1 eV when deposited at 105 °C to 3.2 eV when deposited at 195 °C for $Sn_{1-x}Ga_xO_y$ films with $x = 0.6$, deposited by a 1:1 process. It is not possible to pinpoint the exact mechanism behind this effect from the available data. Any influence

71
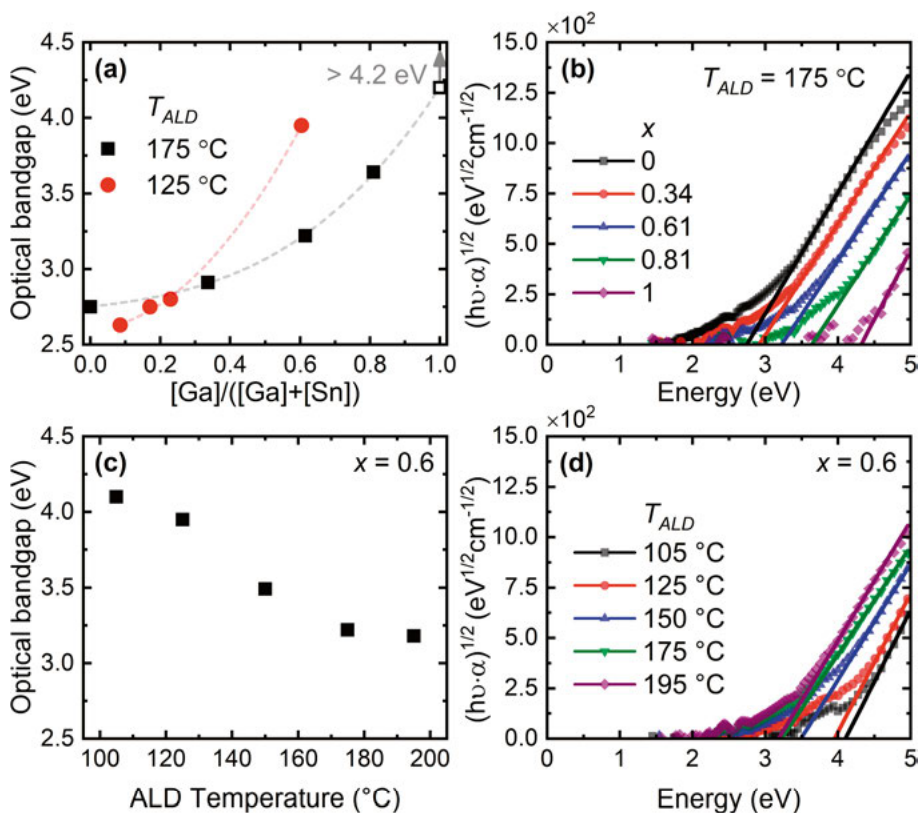
Figure 7.6. Optical band gaps of $Sn_{1-x}Ga_xO_y$ films versus (a) cation composition for films deposited at 125 °C and 175 °C, and (c) deposition temperature for films with a cation ratio of $x = 0.6$. The corresponding Tauc plots are shown in (b) and (d), respectively, with exception of films deposited at 125 °C with varying composition. Reworked with data from Papers IV and V.

from quantum confinement by grain size is unlikely, since the as-deposited films were confirmed to be fully amorphous by electron diffraction. However, the observed deposition-temperature-induced bandgap shift was accompanied by variations in two material properties, namely the film density and impurity content. See Paper IV for more details.

7.1.4 Note on electrical properties

All deposited $Sn_{1-x}Ga_xO_y$ films were highly resistive, with resistivity values higher than 10^4 Ω·cm, as determined by the van der Pauw method [135]. It was unfortunately not practically possible to determine the carrier mobility due to the high resistivity. However, it can be noted that a bulk resistivity of above 10^4 Ω·cm corresponds to a charge carrier concentration lower than 10^{13}–10^{15} cm^{-3}, according to Eq 2.1 and assuming an electron mobility in the range 1–100 cm^2/(V·s).

7.2 Solar cells with $Sn_{1-x}Ga_xO_y$ buffer layers

The potential use of $Sn_{1-x}Ga_xO_y$ as a buffer layer was evaluated in Paper V with RbF post-deposition treated ACIGS absorbers, provided by Solibro Research AB. All absorbers used within each experimental series originated from the same co-evaporation batch and they were capped with CdS directly after deposition in order to reduce surface deterioration during storage. The capping layer was etched off in diluted hydrochloric acid prior to ALD of $Sn_{1-x}Ga_xO_y$. Note that this absorber preparation method results in excellent experimental repeatability by eliminating experimental variation caused by varying absorber properties, which is in general very valuable from an experimental design perspective. On the other hand, this can also potentially modify the ACIGS surface and thus the junction properties. However, any such effects would be similar for all samples.

The $Sn_{1-x}Ga_xO_y$ films grew in a highly conformal manner on the ACIGS absorbers, as shown in the high-angle annular dark field (HAADF) STEM image in Figure 7.7a. Furthermore, an elemental analysis with EDS did not show any signs of any significant compositional gradients or large inhomogeneities in the films, although slight variations near the interface to ACIGS cannot be excluded. See compositional maps in Figure 7.7b. Note that the main contrast within the $Sn_{1-x}Ga_xO_y$ layer is from measurement noise, which could not be improved without risking beam-induced damages.

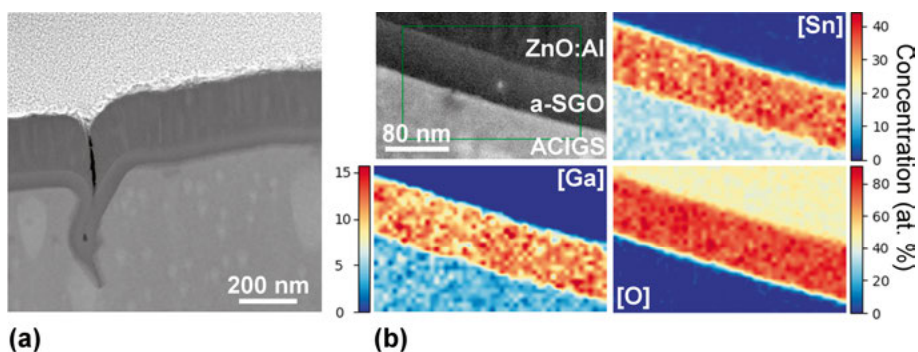**Figure 7.7**. (a) HAADF STEM cross-sectional image of a ACIGS/$Sn_{1-x}Ga_xO_y$/ /ZnO:Al solar cell stack, and (b) EDS composition maps of Sn, Ga and O. The $Sn_{1-x}Ga_xO_y$ film had a cation ratio of $x = 0.18$ and was deposited at 125 °C with a 7:1 sub-cycle ratio (Sn:Ga). Note that the Sn signal in ACIGS layer is due to an overlapping signal from In. Reworked from Paper V.

7.2.1 Controlling the CBO at the absorber/buffer interface

To investigate the possibility to control the absorber/buffer CBO when applying $Sn_{1-x}Ga_xO_y$ as a buffer layer, a series of solar cells with $Sn_{1-x}Ga_xO_y$ buffer layers was fabricated where the cation composition was varied at 125 °C and 175 °C. The resulting J–V curves (after light soaking) are shown in Figure 7.8 and the extracted values for V_{oc}, FF, J_{sc} and η are shown in Figure 7.9. For devices with buffer layers deposited at 125 °C, the average V_{oc} increased from 572 mV to 659 mV when x increased from 0 to 0.17, whereas the average FF value barely changed. A further increase in x to 0.34 had a negligible effect on V_{oc}, while the average FF decreased from around 60% to 48%. These opposing trends are typically observed when the absorber/buffer CBO is varied from a cliff-like to a strong spike-like offset (see Section 6.2). In support of this, the ACIGS/$Sn_{1-x}Ga_xO_y$ CBO was estimated to be around +0.8 eV for a $Sn_{1-x}Ga_xO_y$ buffer layer deposited at 125 °C with $x = 0.33$ (see Paper V for details), which indicates that a spike-like offset is obtained for high gallium concentrations.

A similar trend can be seen in the data for the solar cells fabricated with $T_{ALD} = 175$ °C. The main differences are that (i) the solar cells with pure SnO_2 buffer layers showed considerably lower V_{oc} values in average than observed for $T_{ALD} = 125$ °C (446 mV compared to 572 mV). (ii) In addition, these samples also exhibited a rollover (of unknown origin) in the first quadrant of the J–V curve, which indicates a transport barrier for the forward current. (iii) The J–V data indicates that the optimal $Sn_{1-x}Ga_xO_y$ composition for these absorbers is found at $x \approx 0.2$ for $T_{ALD} = 125$ °C and around $x \approx 0.4$ for $T_{ALD} = 175$ °C.

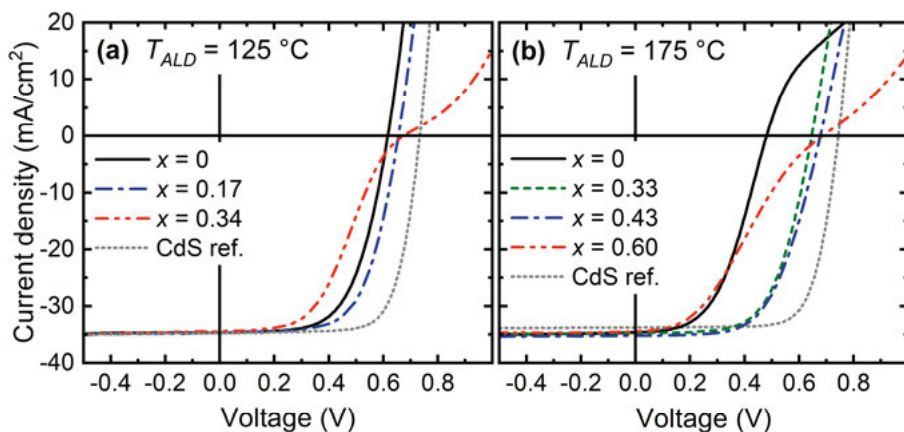**Figure 7.8**. Best cell J–V characteristics of ACIGS solar cells with 25–30 nm $Sn_{1-x}Ga_xO_y$ buffer layers where the cation ratio was varied between (a) 0 and 0.34 for $T_{ALD} = 125$ °C, and (b) between 0 and 0.60 for $T_{ALD} = 175$ °C. The corresponding ACIGS/CdS devices are included as reference. Reworked from Paper V.
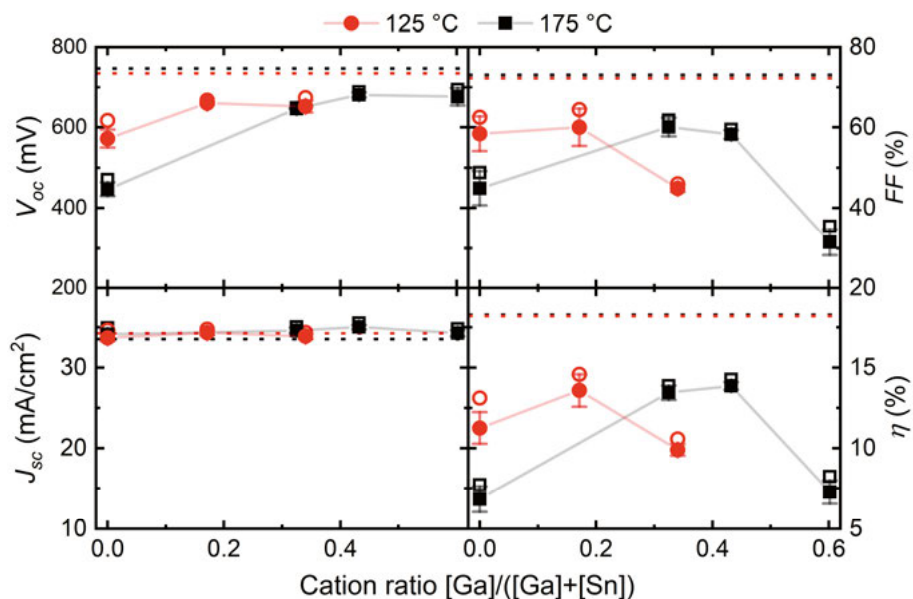
Figure 7.9. Average (filled symbols) and best (open symbols) V_{oc}, FF, J_{sc}, and η for ACIGS solar cells with 25–30 nm $Sn_{1-x}Ga_xO_y$ buffer layers with varying cation ratio for $T_{ALD} = 125\ °C$ (red circles) and $T_{ALD} = 175\ °C$ (black squares). Error bars show the within-sample standard deviation and dashed lines show the average parameters for each corresponding CdS reference. Reworked from Paper V.

The difference in optimal composition is likely explained by a shift in electron affinity when varying the deposition temperature, which is plausible considering that the bandgap varies with deposition temperature, as previously shown. It is also noted that the optimal composition at each deposition temperature yields roughly the same optical bandgap ($E_g = 2.8 \pm 0.1$ eV). While it is not known to which extent the observed bandgap variations are explained by variations in the E_{CBM} opposed to variations in E_{VBM}, the J–V data supports the prediction that a large part of the bandgap variation in $Sn_{1-x}Ga_xO_y$ is due to an altered electron affinity. It is therefore expected that a beneficial CBO can be obtained even for wide-bandgap absorbers, such as $CuGaSe_2$ or $Cu(Ga,In)S_2$, by tuning the buffer layer properties.

7.2.2 Effect of $Sn_{1-x}Ga_xO_y$ buffer layer thickness on metastability

When screening the effects of $Sn_{1-x}Ga_xO_y$ layer thickness on the solar cell performance, it was found that the solar cell's response to light soaking[†] varied for different thicknesses. It was observed that thin buffer layers suffered from light-induced degradation of V_{oc} and FF, whereas light soaking improved V_{oc}

[†]Light soaking was performed under illumination from an Osram Powerstar HQI-T 250W metal-halide lamp during which the samples were unintentionally heated to around 60 °C.

Table 7.2. Average (and best) J–V parameters for ACIGS/$Sn_{1-x}Ga_xO_y$ devices with different buffer layer thicknesses. The $Sn_{1-x}Ga_xO_y$ layers were deposited at 125 °C.

Buffer layer	LS[†]	V_{oc} (mV)	FF (%)	J_{sc} (mA/cm^2)	η (%)
8 nm a-SGO	None	644 (673)	65.5 (67.4)	34.5 (35.1)	14.6 (15.1)
(x = 0.19)	1 hour	667 (689)	65.1 (67.6)	34.6 (35.2)	15.0 (15.5)
	3 days	626 (659)	56.0 (64.7)	34.4 (35.7)	12.2 (15.0)
26 nm a-SGO	None	606 (623)	59.2 (63.7)	34.5 (35.1)	12.4 (13.7)
(x = 0.17)	4 days	660 (667)	60.0 (64.4)	34.4 (34.8)	13.6 (14.6)
51 nm a-SGO	None	600 (610)	59.7 (61.3)	34.0 (34.4)	12.2 (12.4)
(x = 0.18)	4 days	640 (647)	63.7 (64.7)	35.0 (35.4)	14.3 (14.6)
CdS reference	None	737 (741)	72.1 (73.3)	34.2 (34.5)	18.2 (18.6)
	3 days	734 (736)	72.2 (73.2)	34.3 (34.7)	18.2 (18.6)

[†]LS: Light soaking

and *FF* for thicker buffers. This is shown in Table 7.2 which lists the average (and best) values for V_{oc}, *FF*, J_{sc} and η for a series of ACIGS/$Sn_{1-x}Ga_xO_y$ solar cells where the thickness was varied (d = 8/26/51 nm) while keeping the cation ratio constant (x = 0.18 ± 0.01). As pointed out in Section 6.6, many factors can influence the light-induced metastability of CIGS solar cells. This includes the effect of light soaking on bulk properties of ACIGS [136]. Another contributing factor might be light-induced changes to the electrical properties of $Sn_{1-x}Ga_xO_y$. This was investigated in Paper V by analyzing Al/$Sn_{1-x}Ga_xO_y$/n-Si metal–oxide–semiconductor capacitors (MOSCAPs) that were fabricated and characterized by dark J–V and C–V. Both an increased charge-transport barrier (suppressed forward and reverse current) and a shift in fixed-oxide charges to less negative values were observed for thin oxide layers (d = 13 and 26 nm).

The light soaking effects make it more difficult to compare the performance of different $Sn_{1-x}Ga_xO_y$ thicknesses. Nonetheless, when comparing the J–V parameters for each sample's best light soaking condition, it can be observed that the average *FF* for solar cells with 51 nm $Sn_{1-x}Ga_xO_y$ was similar to the average *FF* obtained with 8 nm $Sn_{1-x}Ga_xO_y$ (63.7% compared to 65.5%). This suggests that series resistance associated with charge transport within the bulk of the a-SGO layer was not the factor that limited *FF* in the solar cells in this series.

7.2.3 Evaluation of the best ACIGS/$Sn_{1-x}Ga_xO_y$ solar cell

After further variations of the buffer layer thickness and composition, the best ACIGS/$Sn_{1-x}Ga_xO_y$ solar cell was fabricated with a 14 nm thick buffer layer with cation ratio x = 0.25 that was deposited at 125 °C. The J–V characteristics of this cell is compared to the best CdS reference in Figure 7.10a. An

efficiency of 17.0% was obtained after 4 hours of light soaking (V_{oc} = 705 mV, FF = 69.8%, J_{sc} = 34.5 mA/cm^2), which can be compared to 18.6% for the best CdS reference (V_{oc} = 734 mV, FF = 73.0%, J_{sc} = 34.7 mA/cm^2). However, the $Sn_{1-x}Ga_xO_y$ sample showed a slight degradation in FF during prolonged light soaking, leading to a stabilized efficiency of 16.5%. Even before degradation, the difference in FF accounted for around half of the efficiency difference between the $Sn_{1-x}Ga_xO_y$ solar cell and the CdS reference. Fitting of one-diode models to the experimental data suggested that the FF difference was mainly due to a difference in series resistance, possibly due to an impeded charge transport across the $ACIGS/Sn_{1-x}Ga_xO_y$ or $Sn_{1-x}Ga_xO_y/ZnO:Al$ interface (no intrinsic layer was used).

An important property of $Sn_{1-x}Ga_xO_y$ buffer layers is the reduced parasitic absorption due to a wider bandgap compared to CdS. This is seen in Figure 7.10b, where IQE and EQE are shown for the best solar cells with $Sn_{1-x}Ga_xO_y$ and CdS buffer layers. This gain in J_{sc} is not apparent in the J–V measurements, due to an unfavorable position of reflection fringes relative to the AM1.5G spectrum. Note that this leads to a biased efficiency comparison between the different solar cells in favor of the CdS references (although it might also be possible to use thinner CdS layers).
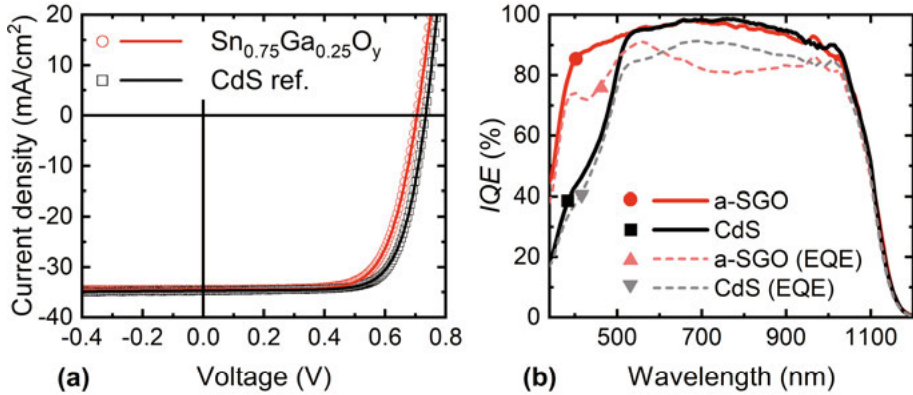
Figure 7.10. (a) Measured J–V characteristics (solid lines) and fitted one-diode models (open symbols) for the best fabricated ACIGS solar cell with a $Sn_{1-x}Ga_xO_y$ buffer layer (d = 14 nm, x = 0.25) and the best corresponding CdS reference cell. The fitted one-diode parameters are A = 2.09, J_0 = 68.5 nA/cm^2, R_s = 1.05 $\Omega \cdot$cm^2, and R_{sh} = 9.42 k$\Omega \cdot$cm^2 for the solar cell with $Sn_{1-x}Ga_xO_y$ and A = 2.03, J_0 = 27.0 nA/cm^2, R_s = 0.65 $\Omega \cdot$cm^2, and R_{sh} = 2.24 k$\Omega \cdot$cm^2 for the CdS reference. (b) IQE of the best cells as estimated by reflection-corrected EQE (solid lines). EQE is included for comparison (dashed lines).

7.2.4 Effect of a Ga_2O_3 interlayer in $ACIGS/Sn_{1-x}Ga_xO_y$ solar cells

The possibility to chemically passivate the $ACIGS/Sn_{1-x}Ga_xO_y$ interface was explored by initiating the buffer layer ALD process with 10 cycles of pure Ga_2O_3, resulting in an interlayer with a maximum thickness of about 1 nm. This reduced the V_{oc} difference to 16–20 mV compared to the best CdS reference cell, and a best cell efficiency of 17.0% was attained before light soaking (V_{oc} = 721 mV, FF = 68.1%, J_{sc} = 34.7 mA/cm^2). However, all fabricated solar cells with this layer structure showed a severe degradation in FF after light soaking. Nevertheless, the similar V_{oc} values as for the CdS references indicate that structures with $Sn_{1-x}Ga_xO_y$ buffer layers can achieve relatively low (near-)interface recombination rates. Moreover, the results also suggest that the properties of the $ACIGS/Sn_{1-x}Ga_xO_y$ interface can be improved.

7.3 ALD of ternary compounds on CIGS

Variations in composition can occur during the first nanometer(s) of growth when ternary compounds are deposited on CIGS with ALD by a super-cycle approach, if the growth is not limited by steric hindrance and the two binary processes experience different degrees of substrate-enhanced or substrate-inhibited growth (see Section 5.1.3). Other non-ideal effects can also contribute.

The initial growth of $Sn_{1-x}Ga_xO_y$ and $Zn_{1-x}Sn_xO_y$ on CIGS surfaces was studied in-situ in Paper VI by employing a QCM-based methodology. Polished and unpolished commercial Cr/Au-coated quartz monitor crystals were pre-coated with a Mo/(NaF)/CIGS thin-film stack before being mounted in the ALD reactor, after which the deposited mass during the initial growth was recorded with a QCM monitor. In addition, the effect of RbF-PDT on the ALD growth was also studied. Figure 7.11 shows the increase in Sauerbrey's mass per individual sub-cycle for each super cycle, as extracted from QCM measurements, when $Sn_{1-x}Ga_xO_y$ and $Zn_{1-x}Sn_xO_y$ were deposited at 125 °C, using a 1:1 sub-cycle ratio and 1 s pulse times for both processes. Note that the measured deposited mass values depend on the total surface area, which seemed to vary during the initial growth. The total surface area is essentially determined by the surface roughness and possible pores and cracks in the CIGS layer. Island growth during nucleation can also contribute (see Section 5.1.3). The apparent mass gain per cycle is therefore not necessarily linearly related to GPC throughout the entire process. In either way, a delay in nucleation was observed for both processes on as-deposited CIGS, while being more pronounced for $Zn_{1-x}Sn_xO_y$ for which it required 40 super-cycles (i.e. 80 sub-cycles) before any significant film growth occurred.
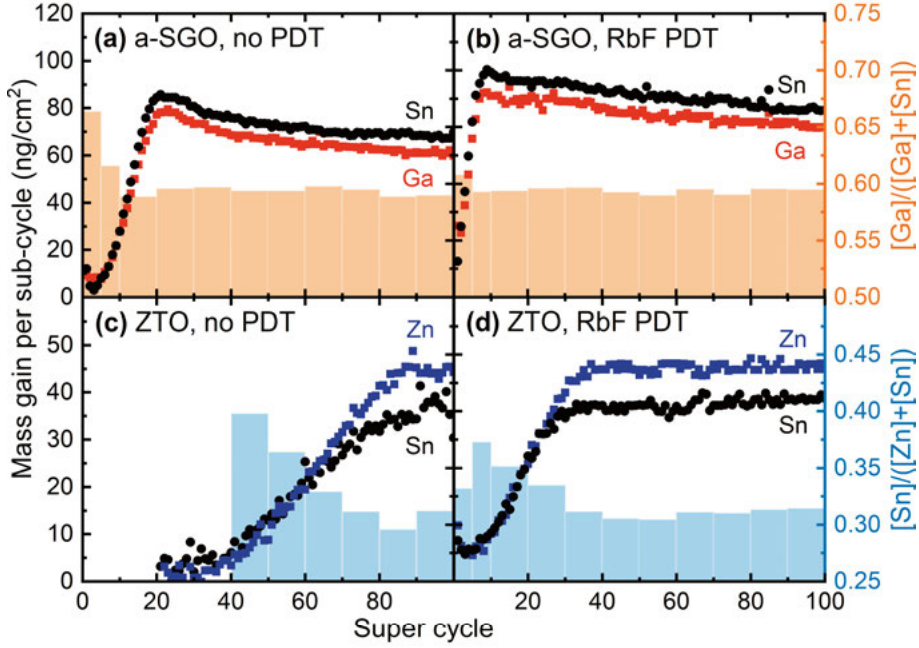
Figure 7.11. Mass gain per super-cycle for each sub-cycle type (symbols) as extracted from QCM recordings of the initial ALD growth of $Sn_{1-x}Ga_xO_y$ and $Zn_{1-x}Sn_xO_y$ on as-deposited and RbF-treated CIGS. The bar plots show estimated depth profiles of the cation ratio in respective process. Adapted from Paper VI.

The nucleation delay was considerably reduced in both processes for growth on RbF-treated CIGS surfaces, indicating an increased number of reactive surface sites for both processes.

A difference in mass gain during the initial cycles of each ALD process results in a composition gradient in the films. The bar plots in Figure 7.11 provide estimated cation compositions in different segments of the films, where each segment corresponds to 5 or 10 super cycles. The cation ratio in $Sn_{1-x}Ga_xO_y$ was calculated with Eq. 7.1 and a similar expression was constructed for a $Zn_{1-x}Sn_xO_y$ process with a 1:1 sub-cycle ratio:

$$x_{Zn_{1-x}Sn_xO_y} = \frac{n_{Sn}}{n_{Sn} + n_{Zn}} = \frac{1}{1 + \left(\frac{M_{SnO_2}}{M_{ZnO}}\right)\left(\frac{\Delta m_{Zn-O}}{\Delta m_{Sn-O}}\right)} \qquad (7.2)$$

Both Eq. 7.1 and Eq. 7.2 assume a simple ligand-exchange chemisorption as growth mechanism and the ALD processes must thus be free from non-ideal effects such as non-terminating reactions and exchange reactions between the precursors and the growing film. It is also assumed that no significant diffusion occurs during the process at the low deposition temperature of 125 °C.

The estimated composition in the film segment deposited during the first five super cycles of $Sn_{1-x}Ga_xO_y$ on as-deposited CIGS was $x = 0.66$, whereas the calculated bulk composition was around $x = 0.59$, i.e. the film was enriched in gallium at the interface to CIGS. Similarly for $Zn_{1-x}Sn_xO_y$, the estimated composition corresponding to the first ten super cycles with significant growth after the nucleation delay was $x = 0.40$, compared to an average bulk composition of $x = 0.31$. This corresponds to a relative increase of 29% in tin concentration. Interestingly, the composition gradient was reduced for both processes when the CIGS surface was modified by RbF-PDT. This is possibly related to the observed reduction of nucleation delay. Even so, the deviating composition near the interface to CIGS can potentially have a significant effect on the solar cell performance when employing $Sn_{1-x}Ga_xO_y$ and $Zn_{1-x}Sn_xO_y$ buffer layers, e.g. by influencing the charge-transport properties and recombination rate near the interface. This may also have a negative impact on the experimental reproducibility, considering that different interface compositions were obtained for different CIGS surfaces (with or without PDT). Furthermore, the varying composition is expected to occur within the first 2–3 nm (as estimated in Paper VI) which can be difficult to quantify with conventional ex-situ characterizations techniques. The QCM-based methodology employed in Paper VI was therefore shown to be a very valuable tool for increasing the understanding of the absorber/buffer interface formation in solar cells with ALD-grown buffer layers and enhance the control over ternary ALD processes in general.

Summary of conclusions and outlook

The overall aim of this thesis was to contribute to the general development of window layer structures for chalcopyrite solar cells. This was accomplished in different ways, partly by exploring the potential of existing materials and processes, but also by developing new buffer layer processes and improving the general understanding of ALD processing of ternary buffer layers. This has so far been discussed in a broader context, whereas the main conclusions drawn from the research findings in Papers I–VI are summarized below:

- The i-ZnO thickness can significantly influence the V_{oc} depending on the combination of layers in the window structure, presumably by influencing the type inversion of the CIGS surface.

- The (near-)interface recombination in wide-bandgap CIGS or CuGaSe$_2$ can be considerably reduced by improving the CBO at the absorber/buffer interface. By employing ALD Zn$_{1-x}$Sn$_x$O$_y$ buffer layers in CuGaSe$_2$ solar cells, record high V_{oc} values above 1.0 V can be achieved and the efficiency limitation appears to shift from the absorber/buffer interface to the bulk properties of CuGaSe$_2$.

- Similar beneficial effects from KF-PDT on V_{oc} can be gained with ALD ZnO$_{1-x}$S$_x$ buffer layers as for CBD CdS buffer layers, indicating that the main effect from KF-PDT is not associated with the CBD process.

- A wet-chemical treatment of CIGS after KF-PDT is required prior to ALD growth of ZnO$_{1-x}$S$_x$ buffer layers to avoid a severely inhibited charge transport across the junction (low FF), which is possibly related to residuals salts from the PDT process. Water rinsing of CIGS-KF absorbers results in a surface similar to the one formed during CdS CBD, i.e. a copper- and gallium-depleted surface, presumably including a KInSe$_2$ phase. This modified surface results in slightly lower FF values for solar cells with ALD ZnO$_{1-x}$S$_x$ buffer layers compared to CBD CdS references. However, the FF deficit can be partly mitigated by tuning the H$_2$S:H$_2$O pulse ratio during ALD growth initiation, indicating that the FF limitation is associated with the initial ALD growth on the modified CIGS surface. Similar efficiencies for the solar cells with ZnO$_{1-x}$S$_x$ compared to the CdS

references can be achieved by etching away the KInSe$_2$ layer prior to ALD growth and heat treating the complete devices. This might suggest that the role of the KInSe$_2$ layer in itself is limited, concerning the beneficial effects from KF-PDT.

- Fully amorphous Sn$_{1-x}$Ga$_x$O$_y$ thin films can be grown by low-temperature ALD ($T < 200$ °C) from DMA$_4$Sn, DMA$_3$Ga(-dimer), and water. The optical bandgap in these films can be varied in a wide range by controlling the cation ratio and deposition temperature (from 2.7 eV to above 4.2 eV for $T_{ALD} = 175$ °C).

- A significant part of the bandgap widening in Sn$_{1-x}$Ga$_x$O$_y$ is due to an increased conduction band energy level (as opposed to a decreased valence band energy). It is thus possible to control the absorber/buffer CBO when applying Sn$_{1-x}$Ga$_x$O$_y$ buffer layers. In addition, optical bandgap data suggest that an appropriate CBO may be achievable even for wide-bandgap absorbers, such as CuGaSe$_2$ or Cu(In,Ga)S$_2$.

- The best fabricated ACIGS solar cell with a Sn$_{1-x}$Ga$_x$O$_y$ buffer layer had a lower efficiency compared to the corresponding CdS reference cell (17.0% compared to 18.6%) due to larger recombination losses and higher series resistance, which result in lower V_{oc} and FF values. The increased series resistance seems to be related to interface properties, rather than associated with charge transport within the bulk of Sn$_{1-x}$Ga$_x$O$_y$.

- The V_{oc} difference between the best Sn$_{1-x}$Ga$_x$O$_y$ device and the CdS reference can be reduced to 16–20 mV by adding a thin Ga$_2$O$_3$ interlayer (d ≤ 1 nm) between ACIGS and Sn$_{1-x}$Ga$_x$O$_y$, which indicates that solar cells with Sn$_{1-x}$Ga$_x$O$_y$ buffer layers can achieve relatively low (near-)interface recombination rates and also that the interface properties can likely be improved further.

- ACIGS solar cells with thin Sn$_{1-x}$Ga$_x$O$_y$ buffer layers or Ga$_2$O$_3$ interlayers can suffer from light-induced degradation. This is possibly related to a change in the electrical bulk properties of Sn$_{1-x}$Ga$_x$O$_y$.

- Deposition of ternary compounds on CIGS by ALD can result in significant compositional variations in the first nanometers of growth. This can be studied in-detail by employing a methodology based on QCM with monitor-crystals pre-coated with CIGS. The degree of variation can differ for different CIGS surfaces (e.g. with or without PDT) and is possibly explained by differences in substrate-induced growth inhibition.

An emphasis was placed on ALD processing of buffer layers in this thesis work. However, the addition of alkali-metal fluoride PDT in the solar cell fabrication process complicates the application of ALD buffer layers. An interesting alternative would be to use an elemental alkali metal PDT process, which is yet to be evaluated for ALD buffer layers, if it is not possible to obtain the same effect by adding heavy alkali metals directly during the absorber layer deposition. If the problem with residual salts on the CIGS surface is not solved, a wet-chemical treatment is likely required prior to ALD growth. This would cancel out the main benefits of using a vacuum-based buffer layer deposition process.

In either way, ternary compound buffer layers grown by ALD remain interesting due to the demand for buffer layers with suitable conduction band alignments to wide-bandgap absorbers (e.g. in multi-junction solar cell structures). The application of $Zn_{1-x}Sn_xO_y$ buffer layers showed promising results in $CuGaSe_2$ solar cells, where the (near-)interface recombination could be significantly reduced, as mentioned, resulting in a record cell efficiency of 11.9%. However, despite a seemingly high V_{oc} value of 1017 mV, the device still exhibited a V_{oc} deficit of around 660 mV (i.e. significant recombination losses). The performance was mainly limited by a poor absorber bulk quality, which gives room for further improvements by optimizing the $CuGaSe_2$ bulk properties.

It would also be interesting to evaluate $Sn_{1-x}Ga_xO_y$ as a new buffer layer for wide-bandgap absorbers. In this thesis work, only a first glimpse of the potential of $Sn_{1-x}Ga_xO_y$ was obtained. To further evaluate its potential as a competitive buffer layer, the interface properties and light-soaking behavior should be studied in more detail on a relevant solar cell absorber surface and for different window layer structures.

Finally, it is more complicated to control the properties of ternary compound buffer layers, compared to binary compounds, since the composition (and thus electrical properties) can be different at the absorber interface as compared to the bulk. On the other hand, the QCM-based methodology that was demonstrated in this thesis can potentially enhance the control over the buffer layer composition at the interface, in addition to improve the understanding of the absorber/buffer interface formation in chalcopyrite solar cells with ALD grown buffer layers. This method is believed to be especially valuable when evaluating different absorber materials, surface modifications, or new buffer layer processes.

Sammanfattning på svenska

Tillgång till elektricitet är en nyckelfaktor som bidragit till att den globala livsstandarden aldrig tidigare varit så hög som den är nu. Samtidigt ökar den globala energikonsumtionen, vilket är problematiskt eftersom majoriteten av de energislag som utnyttjas leder till utsläpp av växthusgaser som bidrar till den globala uppvärmningen. För en hållbar utveckling är det nödvändigt att utöka andelen energiproduktion från förnybara energikällor.

Solcellsteknik gör det möjligt att omvandla den energi som finns lagrad i solljus direkt till användbar elektricitet. Den första praktiskt användbara solcellen utvecklades på 1950-talet och var tillverkad med kiselbaserad halvledarteknik. Då låg verkningsgraden på 6%. Idag dominerar fortfarande denna solcellstyp marknaden och det finns kommersiella solcellspaneler med över 20% verkningsgrad. Utvecklingen har gått så långt att solceller kan konkurrera med icke-förnybara energikällor, med avseende på kostnadseffektivitet. Kisel har dock en låg ljusabsorberande förmåga vilket gör att ett relativt tjockt materiallager behövs för att absorbera solljuset till fullo. Dessutom är produktion av kisel en energikrävande process.

Tunnfilmssolceller kan potentiellt reducera både material- och produktionskostnader, jämfört med traditionella kiselsolceller. En av dagens kommersiella tunnfilmssolcellstekniker är baserad på halvledarmaterialet $Cu(In,Ga)Se_2$ (CIGS). Det absorberande lagret i dessa solceller är endast 1–2 µm tjockt, vilket är cirka 50–100 gånger tunnare än ett hårstrå. Med tunnfilmssolceller är det också möjligt att använda lätta och flexibla substrat. Detta kan dels sänka produktions- och installationsrelaterade kostnader ytterligare, men kan även öppna upp för nya möjligheter att integrera solceller i byggnadsarkitektur och ny teknologi.

Denna avhandling syftade att bidra till utvecklingen av tunnfilmssolceller baserade på CIGS eller liknande ljusabsorberande lager av kalkogena halvledare med en kristallografisk kalkopyritstruktur (exempelvis $CuGaSe_2$ och $(Ag,Cu)(In,Ga)Se_2$). Mer specifikt studerades den så kallade fönsterlagerstrukturen i dessa solceller, för att öka förståelsen om hur fönsterlagrens egenskaper och tillverkningsprocesser kan påverka solcellens egenskaper. Därtill utvecklades nya fönsterlagerstrukturer anpassade för solceller med stora bandgap, vilka är intressanta för specialtillämpningar såsom semi-transparenta solceller och så kallade tandemsolceller. Fönsterlagerstrukturen består av flera olika tunnfilmer med individuella

elektriska funktioner, men i enklaste mening utgör fönsterlagerstrukturen den transparenta elektriska kontakten på framsidan (ovansidan) av solcellen.

En mer teknisk beskrivning av fönsterlagerstrukturen är att den typiskt sett består av tre n-dopade transparenta halvledare: ett buffertlager, ett högresistivt lager och en transparent ledande oxid. Tillsammans med det p-dopade absorberande lagret skapas en pn-övergång (en diod) som utgör grunden för hur en solcell fungerar. En solcell absorberar ljus i en process där en elektron i det absorberande lagrets valensband exciteras till ett högre energitillstånd i ledningsbandet, vilket genererar ett elektron-hål-par. Detta par av laddningsbärare måste separeras för att de inte ska rekombinera, vilket skulle innebära att den absorberade energin från solljuset går förlorad. Separationen av laddningsbärare uppnås med hjälp av pn–övergången, vilken ger upphov till ett inbyggt elektriskt fält i solcellen. I detta fält sveps de exciterade elektronerna över gränsskiktet mellan det absorberande lagret och fönsterlagerstrukturenen, vidare ut till den externa kretsen. Dessvärre finns det typiskt sett en hög koncentration av defekter i gränsskiktet mot fönsterlagerstrukturen och via dessa tenderar de exciterade elektronerna att rekombinera. Detta leder till en försämrad verkningsgrad hos solcellerna.

Även om samtliga lager samverkar med varandra, är det främst buffertlagret som ansvarar för att säkerställa att de exciterade elektronerna kan korsa gränsskiktet till fönsterlagerstrukturen så effektivt som möjligt, med minimala rekombinationsförluster. I kommersiella CIGS-solceller beläggs buffertlagret med en våtkemisk deponeringsmetod (eng.: chemical bath deposition). Denna typ av beläggningsprocess är inte optimal, dels eftersom den medför stora volymer av kemiskt avfall som måste hanteras, men också på grund av att den inte är vakuumbaserad till skillnad från de andra beläggningsprocesser som används i produktionskedjan. Detta leder till oönskade avbrott i produktionen som skulle kunna undvikas om samtliga beläggningar utförs i vakuum. Dessutom är det vanligt att använda CdS som buffertlagermaterial. Detta är dels problematiskt på grund av att användandet av kadmium i produkter är kraftigt reglerat av lagstiftning i många länder (exempelvis under REACH inom EU). Men även på grund av att CdS har ett för lågt bandgap (2.4 eV) som leder till en oönskad absorption av ljus innan ljuset når det absorberande lagret och därmed försämrar solcellens verkningsgrad.

Av dessa anledningar avgränsades denna avhandling till att enbart beakta fönsterlagerstrukturer av miljö- och hälsomässigt skonsamma(re) processer, som baseras på vakuumbaserade beläggningsmetoder. En stor vikt i denna avhandling lades på buffertlager belagda med atomlagerdeponering (eng.: atomic layer deposition, ALD). Med denna vakuumbaserade metod är det möjligt att belägga uniforma tunnfilmer över stora substrat, genom sekventiella självterminerande reaktioner mellan en gas (prekursor) och ytan. Endast en andel av ett kristallografiskt atomlager deponeras per tillväxtsekvens (per ALD-cykel) vilket resulterar i en hög precision i

filmtjocklek. Dessutom är det möjligt att deponera ternära förereningar, genom att variera de material som beläggs under de olika ALD-cyklerna.

En lockande egenskap hos många ternära föreningar är möjligheten att variera energinivån av buffertlagrets ledningsbandskant för att skapa en fördelaktig anpassning till det absorberande lagrets ledningsbandskant. I dagsläget är de flesta alternativa buffertlager just ternära föreningar, där $Zn_{1-x}Sn_xO_y$. $Zn_{1-x}Mg_xO$ och $ZnO_{1-x}S_x$ är nämnvärda exempel som tidigare visat lovande resultat i CIGS-solceller.

De senaste åren har det blivit vanligt att efterbehandla CIGS-ytan med fluorider av alkalimetaller (KF, RbF och CsF). Under denna process bildas det salter på ytan som löses upp i en våtkemisk buffertlagerprocess, men inte i en ALD-process. Dessa salter resulterade i en kraftigt försvårad transport av laddningsbärare över gränsskiktet mellan det absorberande lagret och buffertlagret, när ALD $ZnO_{1-x}S_x$ användes i solceller med KF-behandlad CIGS. Om problemet med dessa salter inte går att undvika måste troligtvis en våtkemisk behandling tillämpas före ALD-processen. Detta skulle eliminera de huvudsakliga fördelarna med en vakuumbaserad buffertlagerprocess.

Trots detta är det fortsatt intressant med ternära buffertlager belagda med ALD, speciellt med tanke på en ökande efterfrågan av bra buffertlager till absorberande lager med stort bandgap. I denna avhandling visades det vara möjligt att utnyttja den varierbara ledningsbandskanten hos ALD-belagd $Zn_{1-x}Sn_xO_y$ för att erhålla en god ledningsbandsanpassning till $CuGaSe_2$–ett absorberande lager med ett stort bandgap. Detta resulterade i en signifikant minskning av rekombinationsförluster i solcellen, vilket i sin tur ledde till den bästa rapporterade verkningsgraden för $CuGaSe_2$-solceller (11.9%) samt den högsta rapporterade öppenkretsspänningen ($V_{oc} > 1.0$ V) för alla solceller med CIGS-liknande absorberande lager. I det typiska fallet är verkningsgraden i dessa $CuGaSe_2$-solceller begränsade av den dåliga anpassningen till buffertlagret, men med en förbättrad fönsterlagerstruktur var solcellen istället begränsad av kvalitén på det absorberande lagret. Detta öppnar upp för framtida förbättringar av verkningsgraden för absorberande lager med stora bandgap, efter optimeringar av bulkegenskaperna av $CuGaSe_2$.

I denna avhandling utvecklades även en ny ALD-process för beläggning av amorfa filmer av $Sn_{1-x}Ga_xO_y$ som buffertlager. Förhoppningen var att detta material skulle bilda ett mer defektfritt gränsskikt mot det absorberande lagret, samt uppvisa en ledningsbandskant som är varierbar i ett brett intervall beroende på filmens sammansättning av katjoner. Det sistnämnda visade sig vara fallet, men ledningsbandskanten visade sig också bero på beläggningstemperaturen i ALD-processen. Detta demonstrerades med solceller baserade på $(Ag,Cu)(In,Ga)Se_2$ som absorberande lager och $Sn_{1-x}Ga_xO_y$ som buffertlager. För dessa solceller uppnåddes en högsta verkningsgrad på 17.0% i denna studie. Även om verkningsgraden var lägre än den som erhölls för referenssolceller med konventionella CdS buffertlager (18.6%), var det möjligt att erhålla snarlika rekombinationsförluster samt öka

den optiska transmittansen, jämfört med referenserna. Däremot var transporten av laddningsbärare sämre i solcellerna med $Sn_{1-x}Ga_xO_y$-buffertlager, vilket begränsade verkningsgraden. Dessutom degraderade vissa solceller under belysning, vilket kan vara relaterat till ljuskänsliga elektriska egenskaper hos $Sn_{1-x}Ga_xO_y$. Trots detta bedöms $Sn_{1-x}Ga_xO_y$ vara ett lovande buffertlagermaterial som skulle kunna vara intressant att kombinera med absorberande lager med högt bandgap, men att de olika gränsskikten måste studeras i mer detalj (och optimeras) för att ta reda på den verkliga potentialen av detta material i CIGS-solceller.

Slutligen, det är mer komplicerat att kontrollera egenskaperna av ALD-belagda ternära buffertlagermaterial jämfört med binära föreningar, eftersom sammansättningen nära gränsskiktet mot det absorberande lagret kan skilja sig från bulksammansättningen. Detta kan påverka de lokala elektriska egenskaperna och i sin tur solcellernas verkningsgrad, genom att påverka rekombinationsegenskaper samt transporten av laddningsbärare över gränsskiktet. Dessvärre kan dessa sammansättningsvariationer vara svåra att kvantifiera med konventionella materialanalystekniker. Av denna anledning utvecklades en metod baserad på en kvartskristalloscillator (eng.: quartz crystal microbalance, QCM), där sensorkristallen först belades med CIGS. Genom att sedan i realtid mäta massökningen under ALD-tillväxten av de ternära oxiderna $Zn_{1-x}Sn_xO_y$ och $Sn_{1-x}Ga_xO_y$ på CIGS-ytan kunde en djupprofil över katjonsammansättningen uppskattas. $Zn_{1-x}Sn_xO_y$-lagret blev kraftigt berikat på tenn nära gränsskiktet mot CIGS, medan $Sn_{1-x}Ga_xO_y$-lagret blev berikat på gallium. Hur stora variationerna blev berodde på CIGS-ytans tillstånd, där sammansättningsvariationerna var kraftigt reducerade för RbF-behandlad CIGS-ytor. Ur ett mer generellt perspektiv bedöms denna QCM-baserade metodologi ha stor potential att öka förståelsen för bildandet av gränsskiktet mellan det absorberande lagret och buffertlagret i solceller med ternära buffertlager belagda med ALD. Denna metod kan även vara särskilt åtråvärd vid utvärderingar av olika absorberande lager, ytbehandlingar eller nya buffertlagerprocesser.

Acknowledgements

Pursuing a PhD degree has been an incredible experience for me, during which I have had the pleasure to meet and become acquainted with numerous people to whom I would like to express my warmest gratitude. It would not have been as enjoyable or rewarding without them.

To begin with, I would like to thank **my supervisors** for putting their faith in me, by choosing me as their PhD student, and for their unwavering patience and guidance throughout the years. **Tobias**, I always felt very lucky to have you as my main supervisor. I think we made a great team and had a great deal of fun, both in the office and during travelling. I especially value your efforts to teach me to work independently as a researcher, and the freedom and responsibility you trusted me in the process. **Jan**, you taught me just about everything I know about solar cells (and then some), and I admire your knowledge and passion for solar cell research. Thank you for always showing interest in my latest results and for all discussions we had. **Marika**, thank you for all your support over the years and for being such an inspiring leader of the solar cell group that always manages to radiate joy and energy.

I thank my **co-authors**, which have made a significant scientific contribution to this thesis. I am glad to have had the chance to work with so many talented people!

I thank the current and past members of the **solar cell group** (now division!) for the scientific and non-scientific discussions, spontaneous hallway chats and enjoyable "Fika" moments. Special thanks to **Adam**, for all the fun moments and stories, as well as for always being willing to help in the cleanroom if some machine misbehaved. **Uwe Z.**, for all your help over the years, fun discussions, and answers to my stupid questions regarding electronics or stuff in general. **Jörgen**, for guiding me in the world of semiconductor physics and, together with **Lotten**, providing valuable input on this thesis. **Lars S.**, **Nina** and **Olof**, for all your help running the BAK and more. **Olivier**, for the laughs and projects together. **Tove** and **Jes**, for interesting side-projects, despite using non-chalcopyrite absorbers… **Johan**, for paving the way. **Christopher**, for interesting discussions and motivational muscle-up competitions. **Carl** and **Jonathan S.**, for many enjoyable lunchtime talks. **Natalia**, for good times at the beam line. **Sven** and **Katharina**, for nice talks, good advices and showing me how to defend via Zoom. **Faraz**, **Nishant** and **Corrado**, for our too short time as PhD students together. **Wei-Chao**, for interesting research ideas. **Kostya**, for having the

patience to be surrounded by a division of experimentalists. Other former members **Alexandra**, **Dorothea**, **Oleksandr**, **Piotr**, **Ray**, **Sethu**, **Shuyi**, **Viktor** and **Volodymyr**, for nice times and for having been valuable members of the group. My thanks also go to the visiting PhD students **Sigbjørn**, **Miguel**, **Andrii**, and particularly **Filippo** for the awesome times when you were here and when we met abroad. Your stay in Uppsala was way too short!

I also thank my other colleagues at the **old FTE division**, which have contributed with a wider perspective through the weakly seminars and pleasant company over the years. Thanks to **Tomas K.**, **Lars V.**, **Patrik**, **Malkolm**, **Asta**, **Long**, **Michelle**, **Apurba**, **Shuangshuang, Xingxing** and **Chenyu**. In addition to having been great colleagues, I thank **Lukas** for great brewing inspiration, **Lars R.** for dark hours in-front of the microscope, and **Ramy** for counting the coins and fun times.

I thank the entire **administration staff** for keeping the office running and the **MSL staff** for ensuring a good cleanroom environment, in particular **Amit**, **Björn**, **Farhad**, **Jan-Åke** and **Örjan**. I would also like to thank **Mikael** for maintaining the X-ray laboratory.

My thanks also go to the people who worked at **Solibro**. Thanks, **Olle**, **Francis**, **Jonathan J.** and **Edgar** for nice collaborations and for all superb absorber materials you provided me, which was invaluable for my work. Also thanks to **Daniel**, **Uwe S.**, and **Fredrik** for always being so helpful in the cleanroom in the beginning of my PhD studies.

I thank the **floorball-playing chemists** for welcoming me to many exhausting but fun Monday games.

The **Friday beer tradition** also deserves to be acknowledged! It is really something special, which I wish I could have attended more regularly. Thank you **Wolfgang** for all the stories.

I would also like to express my gratitude to **Torsten Thurén's foundation** for environmental friendly research, for granting me an additional opportunity to pursuit my own ideas.

Lastly, my warmest thanks goes to my **family** and **friends** for all their love and support. Thanks **Mom** and **Dad**, for everything you have done for me. Even though I try my best to avoid walking in your footsteps, I have not been so successful yet. Thanks **Magnus**, my older brother, for inspiring me to dream big. Thanks to **the Johnsson's**, for welcoming me into their family. **Elin**, my beloved wife and companion in life, how could I ever thank you enough? Your support and presence by my side during these years have been invaluable for me. Thank you for being you, and for being the best possible mother to my children that I can imagine. **Tilde** and **Vilgot**, my children, it is amazing how you two constantly manage to consume so much of my energy but, at the same time, providing me with so much more in return. You are my greatest source of joy in life! Moreover, I am also privileged to be surrounded by so many **close friends**, with whom I have enjoyed many nice dinners,

intense board-game nights, and a beer or two. Thank you for past and future adventures!

To those that I forgot to mention by name but deserve my thanks… Sorry!

Appendix A. Summary of material characterization techniques

A.1 Glow-discharge optical emission spectroscopy (GDOES)

GDOES allows for a quantitative depth-resolved measurement of the elemental composition in solid materials. This technique provides good accuracy, low detection limit (in the ppb–ppm range) and can in principle detect all elements. The sample is mounted as a cathode in a glow-discharge source. An applied voltage accelerates argon ions towards the sample surface, resulting in sample atoms being sputtered from the surface. An argon plasma, formed in the discharge process, excites the sample atoms to a higher energy state. During the subsequent de-excitation process, light with characteristic wavelengths are emitted, which can be detected and used to identify and quantify respective elements.

A.2 Reflectance and transmittance (R–T) spectroscopy

R–T spectroscopy is used to quantify the wavelength-dependent reflectance and transmittance of a sample and is measured using monochromatic light at normal incidence. An integrating sphere is used to capture the reflected intensity from both direct and diffuse scattering. Furthermore, the optical absorbance (A) in the material is measured indirectly, and is given by the expression $A = 1 - R - T$. This allows for an estimation of the absorption coefficient of a thin film with thickness d [137]:

$$\alpha = \frac{\ln\left(\frac{1-R}{T}\right)}{d} \qquad \text{(A.1)}$$

Note that multiple scattering within the film is neglected and the expression is thus only valid for high absorption coefficients (i.e. at the absorption edge).

The optical bandgap energies can in-turn be extracted from so-called Tauc plots based on the relationship

$$\alpha \propto \frac{\left(h\nu - E_g\right)^m}{h\nu} \tag{A.2}$$

where $m = \frac{1}{2}$ for direct bandgaps and $m = 2$ for in-direct bandgaps and for amorphous materials [90,138].

A.3 Four-terminal resistivity sensing

A four-terminal sensing setup allows for accurate resistance measurements by avoiding errors associated with contact resistance. This is achieved by using one pair of contacts to apply a current and another pair of contacts to measure the voltage drop induced by the current ($V = I \cdot R$). This principle can be used to measure the sheet resistance of thin films, e.g. by using a four-point probe where the terminals are placed on a line with a well-defined spacing [139], or by using a van der Pauw method where the terminals are placed on the perimeter of the sample [135].

A.4 Scanning electron microscopy (SEM)

SEM is a surface imaging technique that employs a focused electron beam as a probe to produce high-resolution micrographs of samples. The resolution limit is around 1 nm, depending on sample- and instrument-related factors. The incoming electrons, which are accelerated to an energy of 1–30 keV, interact with the atoms in the sample and produce various signals, mainly: (i) secondary electrons from inelastic scattering, (ii) backscattered electrons from elastic scattering, and (iii) emission of characteristic X-rays. These signals can be detected in different ways to obtain information about the surface topography, film morphology, crystallographic properties, and even elemental composition by analyzing the characteristic X-rays with a technique known as energy dispersive X-ray spectroscopy (EDS).

A.5 Transmission electron microscopy (TEM)

TEM is a technique that can be used for many purposes, including imaging with atomic resolution, crystallographic structure determination, and chemical analysis. In comparison to SEM, the electrons are accelerated to considerably higher kinetic energies (up to around 300 keV), where they are best described by wave functions instead of particles in accordance with the wave–particle

duality concept. The sample is prepared in such way that the propagating electron wave can be transmitted through the sample, e.g. by preparing a sample lamella with a thickness below 100 nm in a focused-ion beam system. The electron wave is interacting with the sample when it is propagating through the material, and is then projected on an imaging-device/detector. Depending on how the beam is manipulated by electromagnetic lenses before and after the sample, as well as what types of detectors are used, a wide range of various information can be obtained.

In addition, characteristic X-rays are emitted which can be used for EDS analysis, like in SEM. If the electron beam is focused in a point and used to scan the sample (this is referred to as STEM), compositional maps can be produced. A complementary method to obtain chemical information in STEM is electron energy loss spectroscopy (EELS). This method is more sensitive than EDS to detect atoms with low atomic number and can also be employed to obtain other chemical information, e.g. about chemical bonds.

Interference occurs when the wave propagates through a crystalline material (i.e. material with a periodic atomic structure), which generates so-called diffraction patterns. A diffraction pattern represents a slice of the reciprocal lattice, and thus contains information about the crystal structure(s) of a sample.

A.6 Rutherford backscattering spectrometry (RBS)

RBS is an ion-beam technique that allows for a quantitative analysis and depth profiling of the elemental composition in the near-surface region (< 2–20 µm) of solid materials. The sensitivity is at ppm-level for heavy elements, but worse for light elements. One of the major advantages of this technique is that it can accurately determine the composition of a material without reference samples. RBS is based on analyzing the energy of elastically backscattered ions (e.g. $^4He^+$) that has been accelerated to a kinetic energy of around 1–3 MeV and projected into the sample.

A.7 Time-of-flight elastic recoil detection analysis (ToF–ERDA)

ToF–ERDA is an ion-beam method that is complementary to RBS and can provide elemental composition data for light elements (including hydrogen) from a depth range of around 1 µm. However, the accuracy in composition determination is lower compared to RBS. In ToF–ERDA, 10–100 MeV ions, with higher atomic number than for the atoms to be detected, are projected onto the sample at a certain angle. Sample atoms are ejected from the sample

by collision with the high-energetic primary ions. An energy and time-of-flight detector is then used to identify the sample atoms as well as identify their depth-position in the sample.

A.8 X-ray diffraction (XRD)

XRD is a technique used for phase identification and for obtaining various other structural information from a sample, such as cell parameters, orientation of crystallites (i.e. texture), degree of crystallinity, phase composition, and grain size (in some cases). In this technique, monochromatic X-ray radiation is used to generate a diffraction pattern, which is the result of the interference that occurs when the X-rays are elastically scattered from the electrons in a periodic crystallographic structure (analogous to electron diffraction). Depending on the sample and instrument geometry, different directions in the reciprocal space can be probed. For example, in the commonly used θ–2θ scan, only reflections from crystallographic planes perpendicular to the surface normal are detected.

A.9 X-ray reflectivity (XRR)

XRR is technique that allows for density and highly accurate thickness determination of flat and homogeneous thin films (or multi-layer thin-film stacks). In XRR, an incoming beam of highly collimated monochromatic X-rays is scattered from the sample surface by specular (and diffuse) reflection. For incoming angles below a certain critical angle, total reflection occurs. From the intensity versus incidence angle relationship, the critical angle is determined and used to extract the sample density. Furthermore, when analyzing thin films, reflection fringes appear due to multiple scattering within the film(s), which contain information about the thin-film thickness(es).

A.10 X-ray fluorescence spectrometry (XRF)

XRF is primarily used for quantitative analysis of the elemental composition, for elements heavier than beryllium. The sensitivity is however low for light elements. In addition, it can simultaneously be used for determining the thickness of thin films. The sample is irradiated with X-rays, which are absorbed in the top 1–10 μm of the sample material in a photoionization process, in which an electron is removed from an inner shell orbital (emission of a photoelectron). The excited atom is then relaxed through one of two possible mechanisms: by emission of a characteristic X-ray (X-ray fluorescence) or by emission of an Auger electron. The former mechanism

dominates for heavy atoms and give rise to the detected XRF signal. Note that this technique is principally comparable with EDS in SEM.

A.11 X-ray photoelectron spectroscopy (XPS)

XPS is used to acquire quantitative and qualitative information about the elemental composition and chemical state of surfaces. X-rays are used as the probing beam, similar as in XRF, but it is here the emitted photoelectrons (and Auger electrons) that are detected. The kinetic energy of the photoelectrons is measured and translated into electron binding energies, which are unique to certain orbital levels and thereby used for element identification. Depending on the local chemical surrounding, the binding energies may be shifted. The information depth is determined by the inelastic mean free path (IMFP) of the photoelectrons, which is around 1–10 nm for Al Kα radiation ($E = 1.487$ keV). Note that IMFP depends on the binding energy, where a high binding energy results in a low kinetic energy for the photoelectron and thus a short IMFP. The IMFP can be increased by increasing the X-ray energy, e.g. by using a synchrotron-based X-ray source. The use of so-called hard X-rays ($E > 5$ keV) in XPS is referred to as Hard X-ray Photoemission spectroscopy (HAXPES).

A.12 Capacitance–voltage measurements on metal–oxide–semiconductor capacitors

The capacitance–voltage (C–V) characteristics of metal–oxide–semiconductor capacitors (MOSCAPs) can be analyzed to reveal details about certain electrical properties of the oxide, semiconductor, and the oxide/semiconductor interface. A MOSCAP is constructed from an n- or p-type semiconductor, with an insulating oxide film in-between the semiconductor and the metal contact (the gate). In Paper V, high-frequency (1 MHz) C–V measurements were performed on Al/$Sn_{1-x}Ga_xO_y$/n-Si MOSCAPs. The fabrication process is described in Paper V. By using n-Si with well-defined properties, the number of unknown parameters was minimized and the dielectric constant and (fixed) charges in the oxide layer could be evaluated.

It is beyond the scope of this section to provide an in-depth theory of the C–V characteristics of MOSCAPs. Such descriptions can be found in textbooks on semiconductor device physics, e.g. in ref. [12]. Nonetheless, a summary is given in the following paragraphs.
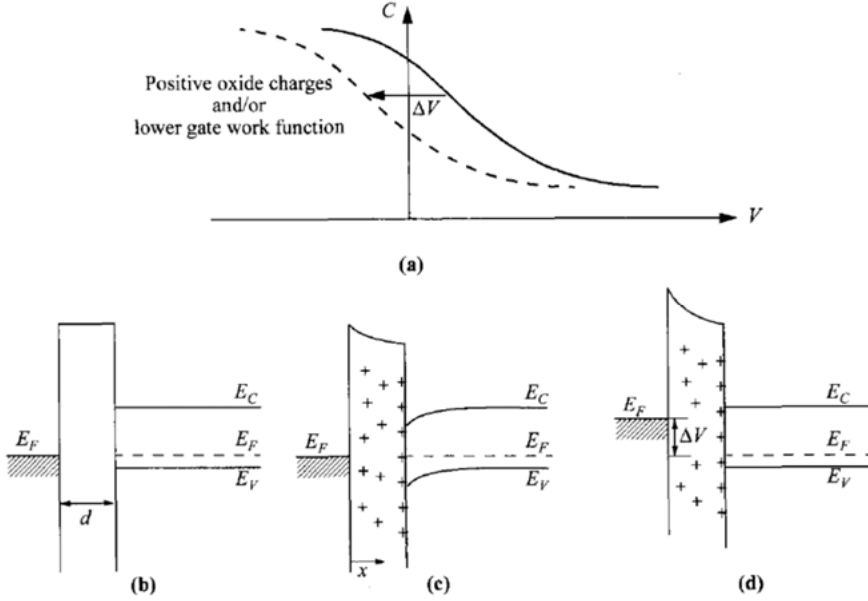
Figure A.1. (a) Voltage shift of a high-frequency C–V curve due to positive oxide charges, for a p-type semiconductor. Energy band diagrams at (b) flat-band condition without oxide charges, (c) with positive oxide charges, and (d) new flat band condition at a negative voltage bias, ΔV. Note that the polarities are reversed for an n-type semiconductor. The figure is reproduced from ref. [12] with permission from John Wiley and Sons.

A typical high-frequency C–V curve for a MOSCAP is shown in Figure A.1a (for a p-type semiconductor). The total capacitance is

$$C = \frac{C_{ox}C_D}{C_{ox} + C_D} \tag{A.3}$$

where C_{ox} is the oxide capacitance and C_D is the capacitance from the semiconductor depletion region. C_D varies with applied voltage, which changes the Fermi level position at the semiconductor surface, i.e. the concentration of electrons and holes (and the depletion width). The highest achievable capacitance in a high-frequency C–V measurement is when the semiconductor surface is accumulated (increased majority charge carrier concentration). In this case, C is dominated by C_{ox} according to Eq. A.3. By determining C_{max}, the oxide dielectric constant can be determined from the relationship

$$C_{max} = C_{ox} = \frac{\varepsilon_{ox}\varepsilon_0}{d} \cdot A \tag{A.4}$$

where ε_{ox} is the dielectric constant, ε_0 is the vacuum permittivity, d is the oxide thickness and A is the area of the MOSCAP.

The flat-band voltage is the voltage where there is no band bending in the semiconductor (see Figure A.1b). The flat-band voltage is equal to zero for an ideal MOSCAP (which neither has oxide charges nor a work-function difference between the metal and semiconductor). If (fixed) charges are present in the oxide, the flat-band voltage is shifted according to

$$\Delta V = -\frac{Q_f}{C_{ox}} \qquad\qquad (A.5)$$

where Q_f is the fixed oxide charge and is described as a two-dimensional sheet of charges. Note that this shifts the entire C–V curve along the voltage axis, as shown in Figure A.1a. A qualitative understanding of the flat-band shift can be gained by considering the effect from Q_f on the band bending. This is illustrated in Figure A.1 b–d for an otherwise ideal MOSCAP. An introduction of Q_f introduces a band bending in the semiconductor and ΔV is the gate voltage necessary to compensate for this effect.

Appendix B. Derivation of rule of mixtures for the cation ratio in ternary oxides grown by ALD

Assume an arbitrary ternary oxide of the type $A_{1-x}B_xO_y$, where A and B are two different cations, and the corresponding binary oxides are $A_\alpha O$ and $B_\beta O$. The cation ratio x is

$$x = \frac{n_B}{n_B + n_A} = \frac{1}{1 + \frac{n_A}{n_B}} \tag{B.1}$$

where n_A and n_B is the number of moles per surface area [mol/cm^2] of cation A and B, respectively. The moles of deposited cations per surface area can be calculated from the moles of deposited oxide formula units and number of cations per formula units:

$$n_A = \left(\frac{m_{A_\alpha O}}{M_{A_\alpha O}}\right) \cdot \alpha \tag{B.2}$$

$$n_B = \left(\frac{m_{B_\beta O}}{M_{B_\beta O}}\right) \cdot \beta \tag{B.3}$$

where m is deposited mass per surface area [g/cm^2] and M is molar mass [g/mol]. As stated in Section 5.2.2, the rule of mixture assumes that the material grown during each sub-cycle is equivalent to the growth in respective binary process. The moles of cations deposited per cycle can thus be expressed as

$$n_A \text{ per cycle} = \frac{GPC_{A_\alpha O} \cdot \rho_{A_\alpha O}}{M_{A_\alpha O}} \cdot \alpha \tag{B.4}$$

$$n_B \text{ per cycle} = \frac{GPC_{B_\beta O} \cdot \rho_{B_\beta O}}{M_{B_\beta O}} \cdot \beta \tag{B.5}$$

where GPC is growth per cycle in [cm] and ρ is film density in [g/cm^3].

The number of moles of cations deposited per surface area by one super-cycle with sub-cycle ratio P is then

$$n_A \text{ per super cycle} = N \cdot (1 - P) \cdot \frac{GPC_{A_\alpha O} \cdot \rho_{A_\alpha O}}{M_{A_\alpha O}} \cdot \alpha \qquad (B.6)$$

$$n_B \text{ per super cycle} = N \cdot P \cdot \frac{GPC_{B_\beta O} \cdot \rho_{B_\beta O}}{M_{B_\beta O}} \cdot \beta \qquad (B.7)$$

where N is the numbers of sub-cycles per super-cycle. An expression for the composition (per super cycle) can then be obtained by inserting Eq. B.6 and Eq. B.7 into Eq. B.1:

$$x = \frac{1}{1 + \left(\dfrac{1 - P}{P}\right)\left(\dfrac{M_{B_\beta O}}{M_{A_\alpha O}}\right)\left(\dfrac{GPC_{A_\alpha O} \cdot \rho_{A_\alpha O}}{GPC_{B_\beta O} \cdot \rho_{B_\beta O}}\right)\left(\dfrac{\alpha}{\beta}\right)} \qquad (B.8)$$

References

[1]   H. Ritchie, M. Roser, Access to Energy, Our World Data. (2020). https://our-worldindata.org/energy-access (accessed February 19, 2020).

[2]   BP Statistical Review 2019, BP Glob. (2019). http://www.bp.com/statisticalreview (accessed February 25, 2020).

[3]   Climate and Earth's Energy Budget, (2009). https://earthobservatory.nasa.gov/features/EnergyBalance/page4.php (accessed February 19, 2020).

[4]   C.E. Fritts, On a new form of selenium cell, and some electrical discoveries made by its use, Am. J. Sci. s3-26 (1883) 465–472. https://doi.org/10.2475/ajs.s3-26.156.465.

[5]   G. Meyers, Photovoltaic Dreaming 1875-1905: First Attempts At Commercializing PV, CleanTechnica. (2014). https://cleantechnica.com/2014/12/31/photovoltaic-dreaming-first-attempts-commercializing-pv/ (accessed February 19, 2020).

[6]   D.M. Chapin, C.S. Fuller, G.L. Pearson, A New Silicon p-n Junction Photocell for Converting Solar Radiation into Electrical Power, J. Appl. Phys. 25 (1954) 676–677. https://doi.org/10.1063/1.1721711.

[7]   Photovoltaics Report, Fraunhofer ISE. (2019). https://www.ise.fraunhofer.de/content/dam/ise/de/documents/publications/studies/Photovoltaics-Report.pdf (accessed February 22, 2020).

[8]   SunPower® X-Series X22-370 Residential DC Module Datasheet, SunPower. (2018). https://us.sunpower.com/solar-resources/sunpower%C2%AE-x-series-residential-dc-x22-370 (accessed February 19, 2020).

[9]   A. de La Tour, M. Glachant, Y. Ménière, Predicting the costs of photovoltaic solar modules in 2020 using experience curve models, Energy. 62 (2013) 341–348. https://doi.org/10.1016/j.energy.2013.09.037.

[10]   C. Kost, S. Shammugam, V. Jülch, H.-T. Nguyen, T. Schlegl, Levelized Cost of Electricity- Renewable Energy Technologies, Fraunhofer ISE. (2018). https://www.ise.fraunhofer.de/content/dam/ise/en/documents/publications/studies/EN2018_Fraunhofer-ISE_LCOE_Renewable_Energy_Technologies.pdf (accessed February 19, 2020).

[11]   M.A. Green, Solar cells: operating principles, technology and system applications, Repr. [der Ausg.] Englewood Cliffs, NJ 1982, Univ. of New South Wales, Kensington, NSW, 1998.

[12]   S.M. Sze, K.K. Ng, Physics of semiconductor devices, 3rd ed, Wiley Books, Hoboken, N.J, 2006.

[13]   J. Malmström, On generation and recombination in $Cu(In,Ga)Se_2$ thin-film solar cells, Doctoral thesis, Uppsala University, 2005. http://urn.kb.se/resolve?urn=urn%3Anbn%3Ase%3Auu%3Adiva-5721.

[14]   W. Shockley, The Theory of p-n Junctions in Semiconductors and p-n Junction Transistors, Bell Syst. Tech. J. 28 (1949) 435–489.

[15] W. Shockley, H.J. Queisser, Detailed Balance Limit of Efficiency of p-n Junction Solar Cells, J. Appl. Phys. 32 (1961) 510–519. https://doi.org/10.1063/1.1736034.

[16] ASTM G-173-03 Reference Air Mass 1.5 Spectra, NREL. https://www.nrel.gov/grid/solar-resource/spectra-am1.5.html (accessed February 28, 2020).

[17] S. Siebentritt, What limits the efficiency of chalcopyrite solar cells?, Sol. Energy Mater. Sol. Cells. 95 (2011) 1471–1476. https://doi.org/10.1016/j.solmat.2010.12.014.

[18] A.D. Vos, Detailed balance limit of the efficiency of tandem solar cells, J. Phys. Appl. Phys. 13 (1980) 839–846. https://doi.org/10.1088/0022-3727/13/5/018.

[19] B.R. Pamplin, T. Kiyosawa, K. Masumoto, Ternary chalcopyrite compounds, Prog. Cryst. Growth Charact. 1 (1979) 331–387. https://doi.org/10.1016/0146-3535(79)90002-9.

[20] S.B. Zhang, S.-H. Wei, A. Zunger, H. Katayama-Yoshida, Defect physics of the $CuInSe_2$ chalcopyrite semiconductor, Phys. Rev. B. 57 (1998) 9642–9656. https://doi.org/10.1103/PhysRevB.57.9642.

[21] S. Lany, A. Zunger, Light- and bias-induced metastabilities in $Cu(In,Ga)Se_2$ based solar cells caused by the $(V_{Se}-V_{Cu})$ vacancy complex, J. Appl. Phys. 100 (2006) 113725. https://doi.org/10.1063/1.2388256.

[22] P. Szaniawski, From Light to Dark: Electrical Phenomena in $Cu(In,Ga)Se_2$ Solar Cells., Doctoral thesis, Uppsala University, 2017. http://urn.kb.se/resolve?urn=urn%3Anbn%3Ase%3Auu%3Adiva-319454.

[23] M. Bodeg Ård, K. Granath, L. Stolt, Growth of $Cu(In,Ga)Se_2$ thin films by coevaporation using alkaline precursors, Thin Solid Films. 361–362 (2000) 9–16. https://doi.org/10.1016/S0040-6090(99)00828-7.

[24] Leeor. Kronik, D. Cahen, H.W. Schock, Effects of Sodium on Polycrystalline $Cu(In,Ga)Se_2$ and Its Solar Cell Performance, Adv. Mater. 10 (1998) 31–36. https://doi.org/10.1002/(SICI)1521-4095(199801)10:1<31::AID-ADMA31>3.0.CO;2-3.

[25] S.-H. Wei, S.B. Zhang, A. Zunger, Effects of Na on the electrical and structural properties of $CuInSe_2$, J. Appl. Phys. 85 (1999) 7214–7218. https://doi.org/10.1063/1.370534.

[26] Z.-K. Yuan, S. Chen, Y. Xie, J.-S. Park, H. Xiang, X.-G. Gong, S.-H. Wei, Na-Diffusion Enhanced p-type Conductivity in $Cu(In,Ga)Se_2$: A New Mechanism for Efficient Doping in Semiconductors, Adv. Energy Mater. 6 (2016) 1601191. https://doi.org/10.1002/aenm.201601191.

[27] R. Carron, E. Avancini, T. Feurer, B. Bissig, P.A. Losio, R. Figi, C. Schreiner, M. Bürki, E. Bourgeois, Z. Remes, M. Nesladek, S. Buecheler, A.N. Tiwari, Refractive indices of layers and optical simulations of $Cu(In,Ga)Se_2$ solar cells, Sci. Technol. Adv. Mater. 19 (2018) 396–410. https://doi.org/10.1080/14686996.2018.1458579.

[28] H. Neumann, Optical properties and electronic band structure of $CuInSe_2$, Sol. Cells. 16 (1986) 317–333. https://doi.org/10.1016/0379-6787(86)90092-X.

[29] J.L. Shay, B. Tell, H.M. Kasper, L.M. Schiavone, p−d Hybridization of the Valence Bands of I-III-VI$_2$ Compounds, Phys. Rev. B. 5 (1972) 5003–5005. https://doi.org/10.1103/PhysRevB.5.5003.

[30] A. Soni, V. Gupta, C.M. Arora, A. Dashora, B.L. Ahuja, Electronic structure and optical properties of $CuGaS_2$ and $CuInS_2$ solar cell materials, Sol. Energy. 84 (2010) 1481–1489. https://doi.org/10.1016/j.solener.2010.05.010.

[31] J.H. Boyle, B.E. McCandless, W.N. Shafarman, R.W. Birkmire, Structural and optical properties of (Ag,Cu)(In,Ga)Se$_2$ polycrystalline thin film alloys, J. Appl. Phys. 115 (2014) 223504. https://doi.org/10.1063/1.4880243.

[32] J. Keller, K.V. Sopiha, O. Stolt, L. Stolt, C. Persson, J.J.S. Scragg, T. Törndahl, M. Edoff, Wide-gap (Ag,Cu)(In,Ga)Se$_2$ solar cells with different buffer materials—A path to a better heterojunction, Prog. Photovolt. Res. Appl. 28 (2020) 237–250. https://doi.org/10.1002/pip.3232.

[33] S. Wei, A. Zunger, Band offsets and optical bowings of chalcopyrites and Zn-based II-VI alloys, J. Appl. Phys. 78 (1995) 3846–3856. https://doi.org/10.1063/1.359901.

[34] Y. Hinuma, F. Oba, Y. Kumagai, I. Tanaka, Band offsets of CuInSe$_2$/CdS and CuInSe$_2$/ZnS (110) interfaces: A hybrid density functional theory study, Phys. Rev. B. 88 (2013) 035305. https://doi.org/10.1103/PhysRevB.88.035305.

[35] A. Klein, T. Löher, C. Pettenkofer, W. Jaegermann, Chemical interaction of Na with cleaved (011) surfaces of CuInSe$_2$, J. Appl. Phys. 80 (1996) 5039–5043. https://doi.org/10.1063/1.363549.

[36] A.D. Katnani, G. Margaritondo, Empirical rule to predict heterojunction band discontinuities, J. Appl. Phys. 54 (1983) 2522–2525. https://doi.org/10.1063/1.332320.

[37] S. Niki, M. Contreras, I. Repins, M. Powalla, K. Kushiya, S. Ishizuka, K. Matsubara, CIGS absorbers and processes, Prog. Photovolt. Res. Appl. 18 (2010) 453–466. https://doi.org/10.1002/pip.969.

[38] A. Hultqvist, P.M.P. Salomé, V. Fjällström, M. Edoff, B. Aitken, K. Zhang, Y. Shi, K. Fuller, C.K. Williams, Performance of Cu(In,Ga)Se$_2$ solar cells using nominally alkali free glass substrates with varying coefficient of thermal expansion, J. Appl. Phys. 114 (2013) 094501. https://doi.org/10.1063/1.4819802.

[39] S. Binetti, P. Garattini, R. Mereu, A. Le Donne, S. Marchionna, A. Gasparotto, M. Meschia, I. Pinus, M. Acciarri, Fabricating Cu(In,Ga)Se$_2$ solar cells on flexible substrates by a new roll-to-roll deposition system suitable for industrial applications, Semicond. Sci. Technol. 30 (2015) 105006. https://doi.org/10.1088/0268-1242/30/10/105006.

[40] K.H. Ong, R. Agileswari, B. Maniscalco, P. Arnou, C.C. Kumar, J.W. Bowers, M.B. Marsadek, Review on Substrate and Molybdenum Back Contact in CIGS Thin Film Solar Cell, Int. J. Photoenergy. 2018 (2018) 1–14. https://doi.org/10.1155/2018/9106269.

[41] J.H. Scofield, A. Duda, D. Albin, B.L. Ballard, P.K. Predecki, Sputtered molybdenum bilayer back contact for copper indium diselenide-based polycrystalline thin-film solar cells, Thin Solid Films. 260 (1995) 26–31. https://doi.org/10.1016/0040-6090(94)06462-8.

[42] T. Wada, N. Kohara, S. Nishiwaki, T. Negami, Characterization of the Cu(In,Ga)Se$_2$/Mo interface in CIGS solar cells, Thin Solid Films. 387 (2001) 118–122. https://doi.org/10.1016/S0040-6090(00)01846-0.

[43] M. Mazzer, S. Rampino, G. Spaggiari, F. Annoni, D. Bersani, F. Bissoli, M. Bronzoni, M. Calicchio, E. Gombia, A. Kingma, F. Pattini, E. Gilioli, Bifacial CIGS solar cells grown by Low Temperature Pulsed Electron Deposition, Sol. Energy Mater. Sol. Cells. 166 (2017) 247–253. https://doi.org/10.1016/j.solmat.2016.10.048.

[44] J. Keller, N. Shariati Nilsson, A. Aijaz, L. Riekehr, T. Kubart, M. Edoff, T. Törndahl, Using hydrogen-doped In_2O_3 films as a transparent back contact in (Ag,Cu)(In,Ga)Se_2 solar cells, Prog. Photovolt. Res. Appl. 26 (2018) 159–170. https://doi.org/10.1002/pip.2977.

[45] J.K. Larsen, H. Simchi, P. Xin, K. Kim, W.N. Shafarman, Backwall super-strate configuration for ultrathin Cu(In,Ga)Se_2 solar cells, Appl. Phys. Lett. 104 (2014) 033901. https://doi.org/10.1063/1.4862651.

[46] J. Keller, W.-C. Chen, L. Riekehr, T. Kubart, T. Törndahl, M. Edoff, Bifacial Cu(In,Ga)Se_2 solar cells using hydrogen-doped In_2O_3 films as a transparent back contact, Prog. Photovolt. Res. Appl. 26 (2018) 846–858. https://doi.org/10.1002/pip.3025.

[47] P. Reinhard, S. Buecheler, A.N. Tiwari, Technological status of Cu(In,Ga)(Se,S)$_2$-based photovoltaics, Sol. Energy Mater. Sol. Cells. 119 (2013) 287–290. https://doi.org/10.1016/j.solmat.2013.08.030.

[48] O. Lundberg, M. Edoff, L. Stolt, The effect of Ga-grading in CIGS thin film solar cells, Thin Solid Films. 480–481 (2005) 520–525. https://doi.org/10.1016/j.tsf.2004.11.080.

[49] D. Hariskos, S. Spiering, M. Powalla, Buffer layers in Cu(In,Ga)Se_2 solar cells and modules, Thin Solid Films. 480–481 (2005) 99–109. https://doi.org/10.1016/j.tsf.2004.11.118.

[50] W. Witte, S. Spiering, D. Hariskos, Substitution of the CdS buffer layer in CIGS thin-film solar cells: Status of current research and record cell efficiencies, Vak. Forsch. Prax. 26 (2014) 23–27. https://doi.org/10.1002/vipr.201400546.

[51] Cadmium Substance Information, ECHA. https://echa.europa.eu/substance-information/-/substanceinfo/100.028.320 (accessed April 15, 2020).

[52] M. Nakamura, K. Yamaguchi, Y. Kimoto, Y. Yasaki, T. Kato, H. Sugimoto, Cd-Free Cu(In,Ga)(Se,S)$_2$ Thin-Film Solar Cell With Record Efficiency of 23.35%, IEEE J. Photovolt. 9 (2019) 1863–1867. https://doi.org/10.1109/JPHOTOV.2019.2937218.

[53] J. Lindahl, U. Zimmermann, P. Szaniawski, T. Torndahl, A. Hultqvist, P. Salome, C. Platzer-Bjorkman, M. Edoff, Inline Cu(In,Ga)Se_2 Co-evaporation for High-Efficiency Solar Cells and Modules, IEEE J. Photovolt. 3 (2013) 1100–1105. https://doi.org/10.1109/JPHOTOV.2013.2256232.

[54] R. Scheer, L. Messmann-Vera, R. Klenk, H.-W. Schock, On the role of non-doped ZnO in CIGSe solar cells, Prog. Photovolt. Res. Appl. 20 (2012) 619–624. https://doi.org/10.1002/pip.1185.

[55] T. Minemoto, T. Negami, S. Nishiwaki, H. Takakura, Y. Hamakawa, Preparation of $Zn_{1-x}Mg_xO$ films by radio frequency magnetron sputtering, Thin Solid Films. 372 (2000) 173–176. https://doi.org/10.1016/S0040-6090(00)01009-9.

[56] S. Calnan, A.N. Tiwari, High mobility transparent conducting oxides for thin film solar cells, Thin Solid Films. 518 (2010) 1839–1849. https://doi.org/10.1016/j.tsf.2009.09.044.

[57] T. Koida, Y. Ueno, H. Shibata, In_2O_3-Based Transparent Conducting Oxide Films with High Electron Mobility Fabricated at Low Process Temperatures, Phys. Status Solidi A. 215 (2018) 1700506. https://doi.org/10.1002/pssa.201700506.

[58] I. Repins, M.A. Contreras, B. Egaas, C. DeHart, J. Scharf, C.L. Perkins, B. To, R. Noufi, 19.9%-efficient ZnO/CdS/CuInGaSe$_2$ solar cell with 81.2% fill factor, Prog. Photovolt. Res. Appl. 16 (2008) 235–239. https://doi.org/10.1002/pip.822.

[59] P. Jackson, D. Hariskos, E. Lotter, S. Paetel, R. Wuerz, R. Menner, W. Wischmann, M. Powalla, New world record efficiency for Cu(In,Ga)Se$_2$ thin-film solar cells beyond 20%, Prog. Photovolt. Res. Appl. 19 (2011) 894–897. https://doi.org/10.1002/pip.1078.

[60] T. Kato, J.-L. Wu, Y. Hirai, H. Sugimoto, V. Bermudez, Record Efficiency for Thin-Film Polycrystalline Solar Cells Up to 22.9% Achieved by Cs-Treated Cu(In,Ga)(Se,S)$_2$, IEEE J. Photovolt. 9 (2019) 325–330. https://doi.org/10.1109/JPHOTOV.2018.2882206.

[61] B. Huang, S. Chen, H.-X. Deng, L.-W. Wang, M.A. Contreras, R. Noufi, S.-H. Wei, Origin of Reduced Efficiency in Cu(In,Ga)Se$_2$ Solar Cells With High Ga Concentration: Alloy Solubility Versus Intrinsic Defects, IEEE J. Photovolt. 4 (2014) 477–482. https://doi.org/10.1109/JPHOTOV.2013.2285617.

[62] J.P. Teixeira, P.M.P. Salomé, B. Alves, M. Edoff, J.P. Leitão, Evidence of Limiting Effects of Fluctuating Potentials on V$_{OC}$ of Cu(In,Ga)Se$_2$ Thin-Film Solar Cells, Phys. Rev. Appl. 11 (2019) 054013. https://doi.org/10.1103/PhysRevApplied.11.054013.

[63] S. Siebentritt, E. Avancini, M. Bär, J. Bombsch, E. Bourgeois, S. Buecheler, R. Carron, C. Castro, S. Duguay, R. Félix, E. Handick, D. Hariskos, V. Havu, P. Jackson, H. Komsa, T. Kunze, M. Malitckaya, R. Menozzi, M. Nesladek, N. Nicoara, M. Puska, M. Raghuwanshi, P. Pareige, S. Sadewasser, G. Sozzi, A.N. Tiwari, S. Ueda, A. Vilalta-Clemente, T.P. Weiss, F. Werner, R.G. Wilks, W. Witte, M.H. Wolter, Heavy Alkali Treatment of Cu(In,Ga)Se$_2$ Solar Cells: Surface versus Bulk Effects, Adv. Energy Mater. 10 (2020) 1903752. https://doi.org/10.1002/aenm.201903752.

[64] M.A. Contreras, L.M. Mansfield, B. Egaas, J. Li, M. Romero, R. Noufi, E. Rudiger-Voigt, W. Mannstadt, Wide bandgap Cu(In,Ga)Se$_2$ solar cells with improved energy conversion efficiency, Prog. Photovolt. Res. Appl. 20 (2012) 843–850. https://doi.org/10.1002/pip.2244.

[65] S. Ishizuka, CuGaSe$_2$ Thin Film Solar Cells: Challenges for Developing Highly Efficient Wide-Gap Chalcopyrite Photovoltaics, Phys. Status Solidi A. 216 (2019) 1800873. https://doi.org/10.1002/pssa.201800873.

[66] A. Chirilă, P. Reinhard, F. Pianezzi, P. Bloesch, A.R. Uhl, C. Fella, L. Kranz, D. Keller, C. Gretener, H. Hagendorfer, D. Jaeger, R. Erni, S. Nishiwaki, S. Buecheler, A.N. Tiwari, Potassium-induced surface modification of Cu(In,Ga)Se$_2$ thin films for high-efficiency solar cells, Nat. Mater. 12 (2013) 1107–1111. https://doi.org/10.1038/nmat3789.

[67] P. Jackson, R. Wuerz, D. Hariskos, E. Lotter, W. Witte, M. Powalla, Effects of heavy alkali elements in Cu(In,Ga)Se$_2$ solar cells with efficiencies up to 22.6%, Phys. Status Solidi RRL - Rapid Res. Lett. 10 (2016) 583–586. https://doi.org/10.1002/pssr.201600199.

[68] O. Donzel-Gargand, F. Larsson, T. Törndahl, L. Stolt, M. Edoff, Secondary phase formation and surface modification from a high dose KF-post deposition treatment of (Ag,Cu)(In,Ga)Se$_2$ solar cell absorbers, Prog. Photovolt. Res. Appl. 27 (2019) 220–228. https://doi.org/10.1002/pip.3080.

[69] M. Edoff, T. Torndahl, F. Larsson, O. Stolt, N. Shariati-Nilsson, L. Stolt, Post Deposition Treatments of (Ag,Cu)(In,Ga)Se$_2$ Thin Films for Solar Cells, in: 2019 IEEE 46th Photovolt. Spec. Conf. PVSC, IEEE, Chicago, IL, USA, 2019: pp. 0618–0621. https://doi.org/10.1109/PVSC40753.2019.8981287.

[70] Record Cell Chart Explanatory Notes, Natl. Renew. Energy Lab. (2020). https://www.nrel.gov/pv/cell-efficiency.html (accessed April 16, 2020).

[71] U. Rau, H.W. Schock, Electronic properties of Cu(In,Ga)Se$_2$ heterojunction solar cells-recent achievements, current understanding, and future challenges, Appl. Phys. Mater. Sci. Process. 69 (1999) 131–147. https://doi.org/10.1007/s003390050984.

[72] V. Nadenau, U. Rau, A. Jasenek, H.W. Schock, Electronic properties of Cu-GaSe$_2$-based heterojunction solar cells. Part I. Transport analysis, J. Appl. Phys. 87 (2000) 584. https://doi.org/10.1063/1.371903.

[73] M. Burgelman, P. Nollet, S. Degrave, Modelling polycrystalline semiconductor solar cells, Thin Solid Films. 361–362 (2000) 527–532. https://doi.org/10.1016/S0040-6090(99)00825-1.

[74] P.O. Oviroh, R. Akbarzadeh, D. Pan, R.A.M. Coetzee, T.-C. Jen, New development of atomic layer deposition: processes, methods and applications, Sci. Technol. Adv. Mater. 20 (2019) 465–496. https://doi.org/10.1080/14686996.2019.1599694.

[75] D. Hariskos, M. Powalla, N. Chevaldonnet, D. Lincot, A. Schindler, B. Dimmler, Chemical bath deposition of CdS buffer layer: prospects of increasing materials yield and reducing waste, Thin Solid Films. 387 (2001) 179–181. https://doi.org/10.1016/S0040-6090(00)01705-3.

[76] N. Naghavi, S. Spiering, M. Powalla, B. Cavana, D. Lincot, High-efficiency copper indium gallium diselenide (CIGS) solar cells with indium sulfide buffer layers deposited by atomic layer chemical vapor deposition (ALCVD), Prog. Photovolt. Res. Appl. 11 (2003) 437–443. https://doi.org/10.1002/pip.508.

[77] A. Hultqvist, C. Platzer-Björkman, T. Törndahl, M. Ruth, M. Edoff, Proceedings of the 22nd European Photovoltaic Solar Energy Conference, Milan, Italy, 2007.

[78] T. Kobayashi, Z. Jehl Li Kao, T. Kato, H. Sugimoto, T. Nakada, A comparative study of Cd- and Zn-compound buffer layers on Cu(In$_{1-x}$,Ga$_x$)(S$_y$,Se$_{1-y}$)$_2$ thin film solar cells, Prog. Photovolt. Res. Appl. 24 (2016) 389–396. https://doi.org/10.1002/pip.2695.

[79] H. Hiroi, Y. Iwata, S. Adachi, H. Sugimoto, A. Yamada, New World-Record Efficiency for Pure-Sulfide Cu(In,Ga)S$_2$ Thin-Film Solar Cell With Cd-Free Buffer Layer via KCN-Free Process, IEEE J. Photovolt. 6 (2016) 760–763. https://doi.org/10.1109/JPHOTOV.2016.2537540.

[80] S.M. George, Atomic Layer Deposition: An Overview, Chem. Rev. 110 (2010) 111–131. https://doi.org/10.1021/cr900056b.

[81] R.L. Puurunen, Surface chemistry of atomic layer deposition: A case study for the trimethylaluminum/water process, J. Appl. Phys. 97 (2005) 121301. https://doi.org/10.1063/1.1940727.

[82] A.J.M. Mackus, C. MacIsaac, W.-H. Kim, S.F. Bent, Incomplete elimination of precursor ligands during atomic layer deposition of zinc-oxide, tin-oxide, and zinc-tin-oxide, J. Chem. Phys. 146 (2017) 052802. https://doi.org/10.1063/1.4961459.

[83] R.W. Johnson, A. Hultqvist, S.F. Bent, A brief review of atomic layer deposition: from fundamentals to applications, Mater. Today. 17 (2014) 236–246. https://doi.org/10.1016/j.mattod.2014.04.026.

[84] A. Hultqvist, C. Platzer-Björkman, U. Zimmermann, M. Edoff, T. Törndahl, Growth kinetics, properties, performance, and stability of atomic layer deposition Zn-Sn-O buffer layers for Cu(In,Ga)Se$_2$ solar cells, Prog. Photovolt. Res. Appl. 20 (2012) 883–891. https://doi.org/10.1002/pip.1153.

[85] C. Platzer-Björkman, T. Törndahl, D. Abou-Ras, J. Malmström, J. Kessler, L. Stolt, Zn(O,S) buffer layers by atomic layer deposition in Cu(In,Ga)Se$_2$ based thin film solar cells: Band alignment and sulfur gradient, J. Appl. Phys. 100 (2006) 044506. https://doi.org/10.1063/1.2222067.

[86] A.J.M. Mackus, J.R. Schneider, C. MacIsaac, J.G. Baker, S.F. Bent, Synthesis of Doped, Ternary, and Quaternary Materials by Atomic Layer Deposition: A Review, Chem. Mater. 31 (2019) 1142–1183. https://doi.org/10.1021/acs.chemmater.8b02878.

[87] D.K. Lancaster, H. Sun, S.M. George, Atomic Layer Deposition of Zn(O,S) Alloys Using Diethylzinc with H$_2$O and H$_2$S: Effect of Exchange Reactions, J. Phys. Chem. C. 121 (2017) 18643–18652. https://doi.org/10.1021/acs.jpcc.7b05361.

[88] M.N. Mullings, C. Hägglund, J.T. Tanskanen, Y. Yee, S. Geyer, S.F. Bent, Thin film characterization of zinc tin oxide deposited by thermal atomic layer deposition, Thin Solid Films. 556 (2014) 186–194. https://doi.org/10.1016/j.tsf.2014.01.068.

[89] G. Sauerbrey, Verwendung von Schwingquarzen zur Wägung dünner Schichten und zur Mikrowägung, Z. Für Phys. 155 (1959) 206–222. https://doi.org/10.1007/BF01337937.

[90] M. Fox, Optical properties of solids, 2nd ed, Oxford University Press, Oxford ; New York, 2010.

[91] A. Niemegeers, M. Burgelman, A. De Vos, On the CdS/CuInSe$_2$ conduction band discontinuity, Appl. Phys. Lett. 67 (1995) 843. https://doi.org/10.1063/1.115523.

[92] T. Minemoto, T. Matsui, H. Takakura, Y. Hamakawa, T. Negami, Y. Hashimoto, T. Uenoyama, M. Kitagawa, Theoretical analysis of the effect of conduction band offset of window/CIS layers on performance of CIS solar cells using device simulation, Sol. Energy Mater. Sol. Cells. 67 (2001) 83–88. https://doi.org/10.1016/S0927-0248(00)00266-X.

[93] R.L. Anderson, Experiments on Ge-GaAs heterojunctions, Solid-State Electron. 5 (1962) 341–351. https://doi.org/10.1016/0038-1101(62)90115-6.

[94] J. Robertson, Band offsets, Schottky barrier heights, and their effects on electronic devices, J. Vac. Sci. Technol. Vac. Surf. Films. 31 (2013) 050821. https://doi.org/10.1116/1.4818426.

[95] V. Heine, Theory of Surface States, Phys. Rev. 138 (1965) A1689–A1696. https://doi.org/10.1103/PhysRev.138.A1689.

[96] A. Klein, Energy band alignment at interfaces of semiconducting oxides, Thin Solid Films. 520 (2012) 3721–3728. https://doi.org/10.1016/j.tsf.2011.10.055.

[97] A. Klein, Energy band alignment in chalcogenide thin film solar cells from photoelectron spectroscopy, J. Phys. Condens. Matter. 27 (2015) 134201. https://doi.org/10.1088/0953-8984/27/13/134201.

[98] M. Gloeckler, J.R. Sites, Efficiency limitations for wide-band-gap chalcopyrite solar cells, Thin Solid Films. 480–481 (2005) 241–245. https://doi.org/10.1016/j.tsf.2004.11.018.

[99] M. Kapilashrami, C.X. Kronawitter, T. Törndahl, J. Lindahl, A. Hultqvist, W.-C. Wang, C.-L. Chang, S.S. Mao, J. Guo, Soft X-ray characterization of Zn$_{1-x}$Sn$_x$O$_y$ electronic structure for thin film photovoltaics, Phys. Chem. Chem. Phys. 14 (2012) 10154. https://doi.org/10.1039/c2cp41394a.

[100] J. Lindahl, J. Keller, O. Donzel-Gargand, P. Szaniawski, M. Edoff, T. Törndahl, Deposition temperature induced conduction band changes in zinc tin oxide buffer layers for Cu(In,Ga)Se$_2$ solar cells, Sol. Energy Mater. Sol. Cells. 144 (2016) 684–690. https://doi.org/10.1016/j.solmat.2015.09.048.

[101] B.L. Williams, V. Zardetto, B. Kniknie, M.A. Verheijen, W.M.M. Kessels, M. Creatore, The competing roles of i-ZnO in Cu(In,Ga)Se$_2$ solar cells, Sol. Energy Mater. Sol. Cells. 157 (2016) 798–807. https://doi.org/10.1016/j.solmat.2016.07.049.

[102] G. Birant, J. de Wild, M. Meuris, J. Poortmans, B. Vermang, Dielectric-Based Rear Surface Passivation Approaches for Cu(In,Ga)Se$_2$ Solar Cells—A Review, Appl. Sci. 9 (2019) 677. https://doi.org/10.3390/app9040677.

[103] G. Sozzi, S. Di Napoli, R. Menozzi, B. Bissig, S. Buecheler, A.N. Tiwari, Impact of front-side point contact/passivation geometry on thin-film solar cell performance, Sol. Energy Mater. Sol. Cells. 165 (2017) 94–102. https://doi.org/10.1016/j.solmat.2017.02.031.

[104] S. Garud, N. Gampa, T.G. Allen, R. Kotipalli, D. Flandre, M. Batuk, J. Hadermann, M. Meuris, J. Poortmans, A. Smets, B. Vermang, Surface Passivation of CIGS Solar Cells Using Gallium Oxide, Phys. Status Solidi A. 215 (2018) 1700826. https://doi.org/10.1002/pssa.201700826.

[105] J.M.V. Cunha, P.A. Fernandes, A. Hultqvist, J.P. Teixeira, S. Bose, B. Vermang, S. Garud, D. Buldu, J. Gaspar, M. Edoff, J.P. Leitao, P.M.P. Salome, Insulator Materials for Interface Passivation of Cu(In,Ga)Se$_2$ Thin Films, IEEE J. Photovolt. 8 (2018) 1313–1319. https://doi.org/10.1109/JPHOTOV.2018.2846674.

[106] J. Löckinger, S. Nishiwaki, B. Bissig, G. Degutis, Y.E. Romanyuk, S. Buecheler, A.N. Tiwari, The use of HfO$_2$ in a point contact concept for front interface passivation of Cu(In,Ga)Se$_2$ solar cells, Sol. Energy Mater. Sol. Cells. 195 (2019) 213–219. https://doi.org/10.1016/j.solmat.2019.03.009.

[107] J. Keller, F. Gustavsson, L. Stolt, M. Edoff, T. Törndahl, On the beneficial effect of Al$_2$O$_3$ front contact passivation in Cu(In,Ga)Se$_2$ solar cells, Sol. Energy Mater. Sol. Cells. 159 (2017) 189–196. https://doi.org/10.1016/j.solmat.2016.09.019.

[108] M. Sugiyama, H. Sakakura, S.-W. Chang, M. Itagaki, Investigation of Sputtering Damage around pn Interfaces of Cu(In,Ga)Se$_2$ Solar Cells by Impedance Spectroscopy, Electrochimica Acta. 131 (2014) 236–239. https://doi.org/10.1016/j.electacta.2014.04.058.

[109] J. Keller, F. Chalvet, J. Joel, A. Aijaz, T. Kubart, L. Riekehr, M. Edoff, L. Stolt, T. Törndahl, Effect of KF absorber treatment on the functionality of different transparent conductive oxide layers in CIGSe solar cells, Prog. Photovolt. Res. Appl. (2017). https://doi.org/10.1002/pip.2925.

[110] F. Larsson, Study of CVD deposited i-ZnO layers in CIGS thin film solar cells, Master thesis, Uppsala University, 2015. http://urn.kb.se/resolve?urn=urn:nbn:se:uu:diva-253685.

[111] J. Keller, J. Lindahl, M. Edoff, L. Stolt, T. Törndahl, Potential gain in photocurrent generation for Cu(In,Ga)Se$_2$ solar cells by using In$_2$O$_3$ as a transparent conductive oxide layer, Prog. Photovolt. Res. Appl. 24 (2016) 102–107. https://doi.org/10.1002/pip.2655.

[112] S. Ishizuka, K. Sakurai, A. Yamada, K. Matsubara, P. Fons, K. Iwata, S. Nakamura, Y. Kimura, T. Baba, H. Nakanishi, T. Kojima, S. Niki, Fabrication of wide-gap $Cu(In_{1-x}Ga_x)Se_2$ thin film solar cells: a study on the correlation of cell performance with highly resistive i-ZnO layer thickness, Sol. Energy Mater. Sol. Cells. 87 (2005) 541–548. https://doi.org/10.1016/j.solmat.2004.08.017.

[113] J. Pettersson, C. Platzer-Björkman, M. Edoff, Temperature-dependent current-voltage and lightsoaking measurements on $Cu(In,Ga)Se_2$ solar cells with ALD-$Zn_{1-x}Mg_xO$ buffer layers, Prog. Photovolt. Res. Appl. 17 (2009) 460–469. https://doi.org/10.1002/pip.912.

[114] N. Naghavi, T. Hildebrandt, M. Bouttemy, A. Etcheberry, D. Lincot, Impact of the deposition conditions of buffer and windows layers on lowering the metastability effects in $Cu(In,Ga)Se_2/Zn(S,O)$-based solar cell, in: F.H. Teherani, D.C. Look, D.J. Rogers (Eds.), San Francisco, California, United States, 2016: p. 97491I. https://doi.org/10.1117/12.2223151.

[115] H. Hori, K. Tanaka, Y. Oda, T. Minemoto, H. Takakura, Metastability of $Zn_{1-x}Mg_xO/Cu(In,Ga)Se_2$ solar cells with different conduction band offset values, J. Cryst. Growth. 311 (2009) 727–730. https://doi.org/10.1016/j.jcrysgro.2008.09.082.

[116] I.L. Eisgruber, J.E. Granata, J.R. Sites, J. Hou, J. Kessler, Blue-photon modification of nonstandard diode barrier in $CuInSe_2$ solar cells, Sol. Energy Mater. Sol. Cells. 53 (1998) 367–377. https://doi.org/10.1016/S0927-0248(98)00035-X.

[117] M. Theelen, F. Daume, Stability of $Cu(In,Ga)Se_2$ solar cells: A literature review, Sol. Energy. 133 (2016) 586–627. https://doi.org/10.1016/j.solener.2016.04.010.

[118] C. Platzer-Björkman, C. Frisk, J.K. Larsen, T. Ericson, S.-Y. Li, J.J.S. Scragg, J. Keller, F. Larsson, T. Törndahl, Reduced interface recombination in Cu_2ZnSnS_4 solar cells with atomic layer deposition $Zn_{1-x}Sn_xO_y$ buffer layers, Appl. Phys. Lett. 107 (2015) 243904. https://doi.org/10.1063/1.4937998.

[119] T. Ericson, F. Larsson, T. Törndahl, C. Frisk, J. Larsen, V. Kosyak, C. Hägglund, S. Li, C. Platzer-Björkman, Zinc-Tin-Oxide Buffer Layer and Low Temperature Post Annealing Resulting in a 9.0% Efficient Cd-Free Cu_2ZnSnS_4 Solar Cell, Sol. RRL. 1 (2017) 1700001. https://doi.org/10.1002/solr.201700001.

[120] J.K. Larsen, F. Larsson, T. Törndahl, N. Saini, L. Riekehr, Y. Ren, A. Biswal, D. Hauschild, L. Weinhardt, C. Heske, C. Platzer-Björkman, Cadmium Free Cu_2ZnSnS_4 Solar Cells with 9.7% Efficiency, Adv. Energy Mater. 9 (2019) 1900439. https://doi.org/10.1002/aenm.201900439.

[121] A. Hultqvist, J.V. Li, D. Kuciauskas, P. Dippo, M.A. Contreras, D.H. Levi, S.F. Bent, Reducing interface recombination for $Cu(In,Ga)Se_2$ by atomic layer deposited buffer layers, Appl. Phys. Lett. 107 (2015) 033906. https://doi.org/10.1063/1.4927096.

[122] T. Törndahl, C. Platzer-Björkman, J. Kessler, M. Edoff, Atomic layer deposition of $Zn_{1-x}Mg_xO$ buffer layers for $Cu(In,Ga)Se_2$ solar cells, Prog. Photovolt. Res. Appl. 15 (2007) 225–235. https://doi.org/10.1002/pip.733.

[123] T. Kamiya, H. Hosono, Material characteristics and applications of transparent amorphous oxide semiconductors, NPG Asia Mater. 2 (2010) 15–22. https://doi.org/10.1038/asiamat.2010.5.

[124] H. Hosono, M. Yasukawa, H. Kawazoe, Novel oxide amorphous semiconductors: transparent conducting amorphous oxides, J. Non-Cryst. Solids. 203 (1996) 334–344. https://doi.org/10.1016/0022-3093(96)00367-5.

108

[125] T.C. Yeh, Q. Zhu, D.B. Buchholz, A.B. Martinson, R.P.H. Chang, T.O. Mason, Amorphous transparent conducting oxides in context: Work function survey, trends, and facile modification, Appl. Surf. Sci. 330 (2015) 405–410. https://doi.org/10.1016/j.apsusc.2015.01.026.

[126] T. Koida, Y. Kamikawa-Shimizu, A. Yamada, H. Shibata, S. Niki, Cu(In,Ga)Se$_2$ Solar Cells With Amorphous Oxide Semiconducting Buffer Layers, IEEE J. Photovolt. 5 (2015) 956–961. https://doi.org/10.1109/JPHO-TOV.2015.2396356.

[127] W. Mönch, Electronic Properties of Semiconductor Interfaces, in: S. Kasap, P. Capper (Eds.), Springer Handb. Electron. Photonic Mater., Springer International Publishing, Cham, 2017: pp. 1–1. https://doi.org/10.1007/978-3-319-48933-9_8.

[128] J.W. Elam, D.A. Baker, A.J. Hryn, A.B.F. Martinson, M.J. Pellin, J.T. Hupp, Atomic layer deposition of tin oxide films using tetrakis(dimethylamino) tin, J. Vac. Sci. Technol. Vac. Surf. Films. 26 (2008) 244. https://doi.org/10.1116/1.2835087.

[129] Dezelah, J. Niinistö, K. Arstila, L. Niinistö, C.H. Winter, Atomic Layer Deposition of Ga$_2$O$_3$ Films from a Dialkylamido-Based Precursor, Chem. Mater. 18 (2006) 471–475. https://doi.org/10.1021/cm0521424.

[130] M.N. Mullings, C. Hägglund, S.F. Bent, Tin oxide atomic layer deposition from tetrakis(dimethylamino)tin and water, J. Vac. Sci. Technol. Vac. Surf. Films. 31 (2013) 061503. https://doi.org/10.1116/1.4812717.

[131] J.T. Tanskanen, S.F. Bent, Insights into the Surface Chemistry of Tin Oxide Atomic Layer Deposition from Quantum Chemical Calculations, J. Phys. Chem. C. 117 (2013) 19056–19062. https://doi.org/10.1021/jp4063324.

[132] Y. Kang, H. Song, H.-H. Nahm, S.H. Jeon, Y. Cho, S. Han, Intrinsic nature of visible-light absorption in amorphous semiconducting oxides, APL Mater. 2 (2014) 032108. https://doi.org/10.1063/1.4868175.

[133] W. Körner, D.F. Urban, C. Elsässer, Generic origin of subgap states in transparent amorphous semiconductor oxides illustrated for the cases of In-Zn-O and In-Sn-O: Subgap states in transparent amorphous semiconductor oxides, Phys. Status Solidi A. 212 (2015) 1476–1481. https://doi.org/10.1002/pssa.201431871.

[134] W. Körner, C. Elsässer, Density-functional theory study of stability and subgap states of crystalline and amorphous Zn–Sn–O, Thin Solid Films. 555 (2014) 81–86. https://doi.org/10.1016/j.tsf.2013.05.146.

[135] L.J. van der Pauw, A method of measuring specific resistivity and Hall effect of discs of arbitrary shape, Philips Res. Rep. 13 (1958) 1–9.

[136] A. Ferguson, P. Dippo, D. Kuciauskas, R. Farshchi, J. Bailey, G. Zapalac, D. Poplavskyy, Optical Spectroscopic Probes of Degradation and Metastability in Polycrystalline (Ag,Cu)(In,Ga)Se$_2$ Absorbers, in: 2018 IEEE 7th World Conf. Photovolt. Energy Convers. WCPEC Jt. Conf. 45th IEEE PVSC 28th PVSEC 34th EU PVSEC, IEEE, Waikoloa Village, HI, 2018: pp. 3918–3922. https://doi.org/10.1109/PVSC.2018.8548226.

[137] W.Q. Hong, Extraction of extinction coefficient of weak absorbing thin films from special absorption, J. Phys. Appl. Phys. 22 (1989) 1384–1385. https://doi.org/10.1088/0022-3727/22/9/024.

[138] J. Tauc, Optical properties and electronic structure of amorphous Ge and Si, Mater. Res. Bull. 3 (1968) 37–46. https://doi.org/10.1016/0025-5408(68)90023-8.

[139] F.M. Smits, Measurement of Sheet Resistivities with the Four-Point Probe, Bell Syst. Tech. J. 37 (1958) 711–718. https://doi.org/10.1002/j.1538-7305.1958.tb03883.x.

Acta Universitatis Upsaliensis

Digital Comprehensive Summaries of Uppsala Dissertations from the Faculty of Science and Technology 1951

Editor: The Dean of the Faculty of Science and Technology